The Saffman-Taylor Instability using Complex Fluids in Tapered Hele-Shaw Cells

by

Alban Pouplard

A thesis submitted in partial fulfillment of the requirements for the degree of

Master of Science

Department of Mechanical Engineering

University of Alberta

Abstract

This thesis research concerns controlling viscous fingering instability when a less-viscous fluid pushes another more-viscous one in a porous medium. This instability is called the Saffman-Taylor instability and has been extensively studied, primarily for simple Newtonian fluids. The resultant of such growing and wavy interfacial perturbation is the deterioration of the efficiency of industrial processes (e.g., Enhanced Oil Recovery). For Newtonian fluids, it has already been proved that adding a gap gradient to a Hele-Shaw cell is an efficient method to suppress this interfacial instability. In our work, we focus on achieving a total sweep displacement with complex (yield-stress) fluids. We demonstrate the viscous fingering instability suppression using converging cells, whereby we add a negative depth gradient by tapering the upper plate of both radial and rectangular Hele-Shaw cells.

Performing experiments in our homemade rectangularly tapered Hele-Shaw cell, we observe that a converging cell, implying a permeability gradient, can be used to inhibit the viscous fingering instability of complex yield-stress fluids. We investigate, in particular, the impact of the gap gradient (α) and the injection flow rate (Q) on the stabilization of the interface of three complex yield-stress viscous fluids. For a fixed cell gradient, our experimental results show that a full sweep is achieved at a low flow rate, whereas a partial displacement with fingering is obtained when the flow rate is over a critical value.

Furthermore, we develop a theoretical linear stability analysis generalized for common complex fluids possessing a power-law varying viscosity and yield stress. From this analysis, we establish a theoretical stability criterion that we tested which depends on the cell geometry (α, the gap gradient, and W, the cell's width), the interface's gap thickness, and

velocity (h_0 and U_0, respectively), the fluid's viscosity (μ), surface tension (γ) and contact angle (θ_c). Using the experimental values of h_0 and U_0 at the interface, we calculate the value of our theoretical criterion and obtain a good agreement to separate both stable and unstable experimental displacements.

We also carry out similar experimental and theoretical investigations using two complex yield-stress viscous fluids for radially tapered Hele-Shaw cells. We obtain a stability diagram for one of them depending on the gap gradient and the injection flow rate (α v.s Q). Theoretically, we derive a linear stability analysis starting from an effective Darcy's law and the continuity equation replacing the constant viscosity, μ, by an effective viscosity μ_{eff} respecting the Herschel-Bulkley law. From the two governing equations, we obtain a criterion depending on three important parameters. First, the fluid's rheology and characteristics μ_{eff} and the different constants, γ and θ_c. Then, the gap gradient (α) and lastly, the interface radial position, gap thickness, and velocity (r_0, h_0 and U_0, respectively). Once again, using the experimental values of radius of the interface, gap thickness at the interface, and velocity of the interface, we compare our theoretical stability criterion to the experiments. We found good agreement between the two, but we observed a slight discrepancy which is expected due to our assumptions.

As a consequence, we investigate the impact of one major assumption we made in our first linear stability analysis in the radial geometry concerning the Bingham number (ratio of the yield stress to the viscous stress). To do so, we develop a second more complex linear analysis in a radially tapered Hele-Shaw cell. In this new derivation, we obtain another stability criterion by avoiding to neglect the Bingham number. As in our first theoretical derivation, the stability is dependent on the gap gradient (α), the interface position, gap thickness and velocity (r_0, h_0 and U_0), as well as the fluids' viscosity, surface tension and contact angle. We immediately compare this second criterion to our experimental results. We are able to improve the agreement between them for low values of gap gradient. However, for higher values of α, it seems that neglecting or not the Bingham number does not affect the overall agreement between theoretical and experimental results, meaning other assumptions made during our stability analyses still undermine our work.

Preface

This thesis is an original work by Alban Pouplard under the guidance and supervision of Dr. Peichun Amy Tsai. No part of this thesis has been previously published but is in preparation for several journal publications.

Chapter 2 is based on a manuscript in preparation by Alban Pouplard and Peichun Amy Tsai, "Control of Viscous Fingering Instability of Complex Yield-Stress Fluids using a Rectangular Tapered Cell Geometry," in preparation, 2021.

Chapter 3 is based on a manuscript in preparation by Alban Pouplard and Peichun Amy Tsai, "Controlling Viscous Fingering of Complex Fluids," in preparation, 2021.

Chapter 4 is based on a manuscript in preparation by Alban Pouplard and Peichun Amy Tsai, "On the Linear Stability Criterion of Viscous Fingering Instability for Complex Fluids in a Tapered Geometry," in preparation, 2021.

Acknowledgements

First, I wish to show my gratitude to my supervisor Dr. Peichun Amy Tsai, who guided me and supported me these last two and a half years. Her patience, motivation, and immense knowledge have helped me mature and be efficient throughout the entirety of my master's study. She and this experience has and will make a significant impact on my future career. Thanks go to all the students who have been part of the research group for the time I was in and who made my Master's study more enjoyable. I want to give my special regards to Ahmed Aldhalei, Ashley Chen, Behnam Dastvareh, Junyi Yang, Tsai-Hsing Ho, and Yichi Zhang. It has been a real pleasure chatting and working in the same group.

I want to express my gratitude to Bernie Faulkner for his immense help and expertise in building the rectangular set-up.

A special thanks to Rémy Samson, Quentin Champdoizeau, and Jonas Valloton for the unforgettable moments we shared during my time in Edmonton.

Finally, I would like to thank all my friends back in France for their support and, I am particularly grateful to my parents, brothers, and girlfriend for all the love and support they gave me during my whole life.

Contents

List of Tables

List of Figures

Nomenclature

α	Gap gradient
$\bar{k}_{max}$	Dimensionless perturbation's wavenumber of maximum growth rate
δ	Aspect ratio (ratio of the channel width to gap the gap thickness)
$\dot{\gamma}$	Shear rate
γ	Interfacial surface tension
$\hat{w}$	Radial frequency
κ	Consistency index
λ	Viscosity ratio
λ_w	Relative width of the finger (ratio of the finger width to the channel width)
μ	Fluid's viscosity
$\overline{\sigma}$	Dimensionless growth rate of the perturbation
$\overline{k}$	Dimensionless wavenumber of the perturbation
ϕ	Porosity of a porous medium
σ	Growth rate of the perturbation
τ	Shear stress

τ_c	Yield stress
τ_w	Shear stress at the wall
θ_c	Contact angle of the wetting fluid
A	Cross-section area of the porous medium
Bn	Bingham number
Bo	Bond number
Ca	Capillary number
D	Mass diffusion coefficient
De	Deborah number
G''	Loss modulus
G'	Storage modulus
h	Gap thickness
h_0	Gap thickness at the interface
h_c	Gap thickness at the central injection point
h_e	Gap thickness of the thicker spacers at the edge of the rectangular cell
h_f	Gap thickness at the edge of the radial cell
I	Ratio of the typical viscous stresses in the fluid to the bending stiffness of the elastic membrane
k	Absolute permeability of a porous medium (Intro)
k	Wavenumber of the perturbation
L	Characteristic length

M	Fluid's mobility
M_w	Molecular weight
n	Power-law index
P	Pressure
Pe	Peclet number
Q	Flow rate
q	Volumetric flow rate
r_0	Radius at the interface
U	Fluid's velocity
U_0	Velocity of the fluid at the interface
W	Width of the rectangular cell

Chapter 1

Introduction

1.1 Porous Media Flow and Saffman-Taylor Instability

Displacement flows in porous media are vital to understand the working processes of many applications in various industrial domains, such as groundwater hydrology, coating processes, petroleum engineering, and electrochemistry applications, etc. [1, 2]. Even though the theory of porous media flow is complex, primarily due to multiphase fluids and broad length scales ranging from microscopic pores to field scales, the subject has been extensively studied since the 19^{th} century.

A porous medium is defined as a material matrix containing pores or voids, which gases or liquids can fill. Some examples of porous media are sand or rocks. A porous medium is primarily characterized by two parameters: porosity and permeability. The porosity, ϕ, is the measure of the volume fraction occupied by connected void space (while isolated voids are not taken into account) to the total volume of the medium. The permeability, characterized by the permeability coefficient k, is the material's ability to transmit fluid when applied pressure difference. These parameters are dependent on the degree of interconnection of void space, the pore sizes, and the pore distribution [1, 2, 3].

From the mass continuity equation and the momentum equation, one can theoretically derive the correlation between the fluid flow rate (Q) in a porous medium to the pressure difference (ΔP) pushing this fluid [3] via

$$Q = -\frac{kA}{\mu L}\Delta P. \tag{1.1}$$

This formula is known as the Darcy's law. It is applied for a single-phase Newtonian fluid without any elevation change. k is the permeability coefficient defined earlier, μ corresponds to the fluid's viscosity, A is the cross-section area of the medium, and L is the length whereby the pressure difference is applied.

However, multiphase flows are particularly interesting for many applications. In this case, the concept of relative permeability, k_i, of the phase indexed i needs to be introduced. The problems of two-phase flow in a porous medium are treated with Darcy's extended law [3]:

$$\vec{U_i} = -k\frac{k_i}{\mu_i}\vec{\nabla}P. \tag{1.2}$$

This expression works for an horizontal, one-dimensional, immiscible, two-phase flow in a homogeneous and isotropic porous medium. Here, k is the absolute permeability of the porous medium. k_i and μ_i are the relative permeability and the viscosity of the fluid i, respectively. From the Darcy's extended law, it is possible to define the mobility of the fluid i as $M_i = \frac{kk_i}{\mu i}$. This mobility parameter is often used to characterize porous media flow [3].

When a more mobile fluid pushes a less mobile one in a porous medium, interfacial instability occurs. This instability is called the Saffman-Taylor instability and was initially discovered by Hill [4] in a vertical Hele-Shaw cell. Saffman and Taylor [5] studied in 1958 the immiscible displacements of more viscous fluids (oil or glycerine) by less viscous ones (water or air) due to pressure difference in a horizontal Hele-Shaw cell of constant permeability. They found that the interface is unstable and dependent on the Capillary number $Ca = \frac{\mu U}{\gamma}$, with the fluid's velocity, U, and the interfacial surface tension, γ. The Capillary number is defined as the ratio of the viscous forces to surface tension. Furthermore, the instability shaping as a finger gave the common name to the Saffman-Taylor instability: Viscous fingering. Since then, numerous studies have been performed in order to understand and control this instability.

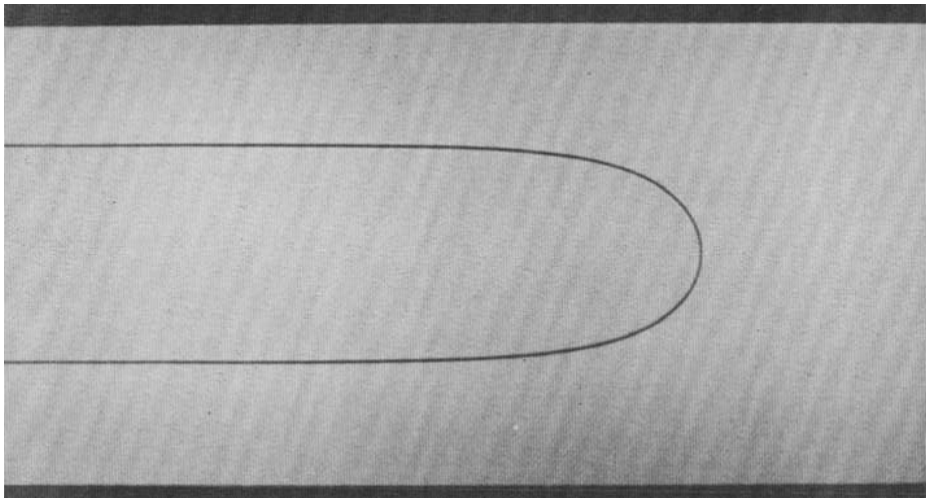

Figure 1.1. Experimental snapshot of air penetrating oil in a horizontal, rectangular Hele-Shaw cell by Tabeling et al. [6].

1.2 Applications

The suppression or the enhancement of the viscous fingering instability is vital to achieving important efficiency in many applications whereby fluids flow through a porous medium. This abundance of applications triggered the motivation of many authors to study this phenomenon. A few examples of applications include chromatographic separation of solvents, fluid mixing in microfluidics, coating flows, and printing devices [7, 8, 9, 10, 11, 12, 13, 14]. Moreover, the Saffman and Taylor instability is an important issue for the geological systems. In this field, the applications impacted by the viscous fingering are numerous due to the porosity of the underground soil. Underground fluid transportation is an ideal example and the applications can be the control of groundwater contamination by a pollutant or any natural element [15, 16], Enhanced Oil Recovery [17, 18, 19, 20, 21, 22, 23] or CO_2 sequestration [2, 24, 25, 26, 23]. Coating flows, Enhanced Oil Recovery, and CO_2 sequestration are three application examples we will discuss in which the instability must, preferably, be avoided.

1.2.1 Coating and Printing Devices

For coating and printing devices, the control of the Saffman–Taylor instability is primordial. Coating is a process by which thin liquid layers are formed and applied to a solid surface. Flows utilized in coating processes are called coating flows. The flows that occur after the coating until the fluid stops moving are also considered as coating flows. There is a good extent of studies around the stability of interfacial flows for coating applications. For example, Pitts et al. and Greener et al. observed that the appearance of ribbing (interfacial) instability for rolling coating or printing experiments depends on the Capillary number and the geometrical parameters of the rollers [7, 8]. These parameters, most famously, are the radius of the rollers and the distance between them. As ribbing instability is a major problem in the coating industry, stability criteria have been searched in all kinds of geometries for years to get rid of the instability. For rolling coating, Savage determined that the requirements are defined in terms of modified Capillary number [9]. In a co-rotating cylinder, the occurrence of the viscous fingering instability depends on the velocity of the cylinders found Rabaud et al. [10]. Grillet et al. and Lee et al. studied the gravity stabilization as a control parameter on the onset of traditional Newtonian viscous fingering in an eccentric cylinder for both Newtonian fluids and Boger fluids [12, 13]. Fig. 1.2 shows a practical example of the ribbing instability in an eccentric cylinder [12].

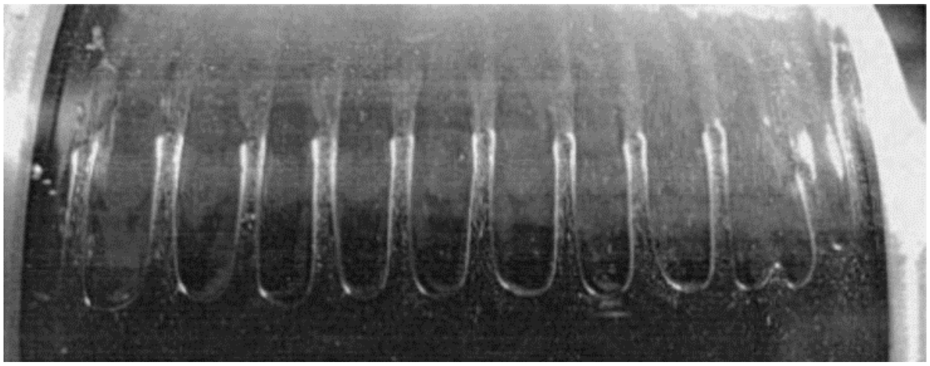

Figure 1.2. Ribbing instability in an eccentric cylinder studied by Grillet et al. [12].

1.2.2 Enhanced Oil Recovery

In the primary oil recovery method to extract oil, it is commonly estimated that around 75% of the light oil and 95% of the heavy oil still remain as residual oil in underground reservoirs [17]. The use of Enhanced Oil Recovery (EOR) is necessary in order to drive out the remaining viscous oil. The first idea used was the water flooding (WF) or water injection (WI). Pushing the remaining oil to the extraction well with water injected via an injection well (see Fig. 1.3). With this method, still, ≈ 60–70% of the original oil in place cannot be mobilized through conventional water floods due to viscous fingering, estimated by Xu et al. [21]. Solutions have been investigated to control the Saffman-Taylor instability or to enhance the efficiency of the oil recovery.

Such an example can be the use of complex fluids such as surfactants [22] or polymers [18, 20] as driving fluids. Surfactants are used to change the wetting properties. In contrast, polymers are usually used to decrease the viscosity (mobility) difference between the driving fluid and the oil and consequently stop the occurrence of fingers in the porous medium. However, both technical and economic factors are essential for the industry and can restrict the practical application of surfactant and polymer flooding. Furthermore, polymer flooding is not recommended for heavy oils with an essential viscosity of thousands of centipoises [18]. With such viscous oils, to enhance the sweep efficiency and suppress viscous fingering, very high concentrations of polymer solution are required to decrease the mobility ratio between driving and receding fluid measurably. Hence, both the cost of chemicals and the difficulty of injection can be drastically increased [18].

A second ingenious solution used for (EOR) is the injection of CO_2. CO_2 flooding is more efficient than water flooding for the same injected volume due to the miscibility of CO_2 with oil observed by Chukwudeme et al. [19]. They also found that the method efficiency is gravely depending on temperature and the pressure of the gas. However, the method has some drawbacks. For instance, it present a poor sweep efficiency attributed to the low viscosity of CO_2. Another issue is gravity segregation. The migration of the CO_2 gas to the top of the reservoir due to buoyancy forces.

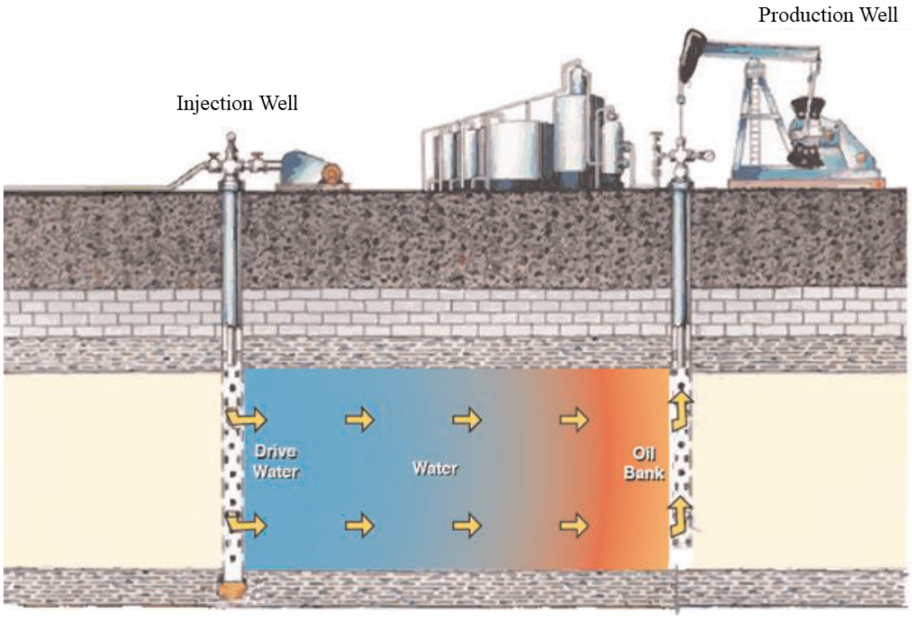

Figure 1.3. A schematic view of Enhanced Oil Recovery. Image from [27].

CO_2 foam flooding water alternating gas (WAG) [22], simultaneous water alternating gas (SWAG), low salinity water injection (LSWI), and carbonated water injection (CWI) [23] are methods to overcome the issues. In terms of sweep efficiency and total recovery, Esene et al. reported CWI as the most promising method [23]. During CWI, CO_2 is dissolved into the water and then injected into the reservoir as a single-phase fluid. Afterwards, the CO_2 diffuse into the oil because both fluids are miscible and change the viscous properties of the oil. This mass transfer of CO_2 improves the mobility ratio and induces a stable displacement of the oil, found by Esene et al. [23]. Moreover, this method shows an additional benefit since with CWI a larger portion of CO_2 is sequestrated into the ground as using a basic CO_2 injection. The necessity of underground CO_2 storage being discuss in the next subsection.

1.2.3 CO_2 Sequestration

Compared to other gases, carbon dioxide is the gas with the highest potential to cause greenhouse effects. CO_2 also accounts for about two-thirds of the global warming potential [23]. For all these environmental issues, it is essential to trap the CO_2 underground instead of letting it flow into the atmosphere. Sequestration of CO_2 in geologic formations has proved to be technologically and financially viable to control CO_2 concentration in the ambient atmosphere [2]. Carbon dioxide sequestration into petroleum reservoirs is being explored to avoid gas release into the atmosphere. This method, consisting of pushing the oil to the extraction well using CO_2, can provide additional efficiency up to 40% of the remaining oil left in reservoirs following primary recovery, observed by Daneshfar et al. [24]. However, the CO_2 storage capability of this approach is very limited. A fraction of the injected CO_2 can eventually come back along with the produced oil at the extraction well. In addition, these geological formations are not large enough to counter-balance the quantity of CO_2 produced by burning the extracted oil. Burning about 1 ft^3 of petroleum product produces 2.2 ft^3 of carbon dioxide [24].

In order to solve this problem, the use of deep saline aquifers has gained interest to sequestrate the CO_2 [25, 26]. Injecting CO_2 into a aqueous solution of $Ca(OH)_2$ in a porous medium, at high pressure, results in a chemical reaction to form $CaCO_3$ deposits in which CO_2 is trapped. However, by injecting a less viscous and less dense gas underground, viscous fingering will occur. It is crucial to control this instability in order to have the best efficiency and store the maximum CO_2. For this application, the control of the Saffman-Taylor instability has already been under investigation. It has been showed by White et al. that the pressure is the stability parameter [25]. At low pressure, the instability is less pronounced, while it is clearly an issue at high pressure. However, the chemical reaction between the CO_2 and $Ca(OH)_2$ being faster at high pressure, the key to efficient CO_2 sequestration is to find the balance between chemical reaction dynamics and the physics of fluid-fluid interfacial instability. To that extent, the use of supercritical CO_2 is being highly investigated in the quest of efficiency [26].

1.3 Immiscible Viscous Fingering in a Hele-Shaw Cell

We saw in the previous section that viscous fingering occurs in many industrial applications. As a consequence, many studies have been done to investigate this instability in a Hele-

Shaw cell. A Hele-Shaw cell consists of two parallel plates separated by a small gap that recreates a quasi-two-dimensional (2D), homogeneous porous medium. This setup is widely used to observe a porous medium flow where direct visualization is usually tricky. A Hele-Shaw cell is characterized by a constant permeability: $k = \frac{h^2}{12}$, with h corresponding to the gap thickness, as well as a porosity equal to the unity as only void is present. The heterogeneous pore structure and distribution are essential aspects of a porous medium that are not captured by Hele-Shaw flows. Nevertheless, this simple geometry is convenient to visualize the quasi-2D pattern morphology and reflect on more complex problems.

Viscous fingering arises when the driving fluid is injected at a sufficient rate so that viscous forces exceed surface tension forces causing the normally stable axisymmetric interface between the two fluids to become linearly unstable to non-axisymmetric perturbations [28]. Different aspects have been studied, for instance, the impact of inertia [29], surface tension [30, 31], gravity [32], three-layer displacement [33] or a chemical reaction at the interface [34, 35]. The instability has been investigated in many different geometries, for example, with rotating Hele-Shaw cells [36, 37, 38]. For our study, we will only focus on the work with horizontal, rectangular (See Fig. 1.1) and radial (See Fig. 1.4) Hele-Shaw cells and two immiscible fluids. The driving fluid is injected, and the receding fluid is pushed.

1.3.1 Newtonian Fluids

Saffman and Taylor were the first to find that a single finger is formed and propagates after the initial instability when a Newtonian fluid of low mobility is pushing another Newtonian fluid of higher mobility in a horizontal rectangular Hele-Shaw cell. This newly named Saffman-Taylor instability is characterized by a dependence of the relative width of the finger λ_w (i.e., the ratio of the finger-width to the channel width) with respect to the Capillary number, $Ca = \frac{\mu U}{\gamma}$ [5]. They found that the ratio of finger-width decreases as Ca increases until it reaches a plateau of $\frac{1}{2}$. Afterward, Saffman observed that λ_w follows a unique curve when scaled with the parameter $1/B = Ca\delta^2$, where the aspect ratio, δ, is the ratio of the channel width to gap thickness between the two plates forming the Hele-Shaw cell [40]. This

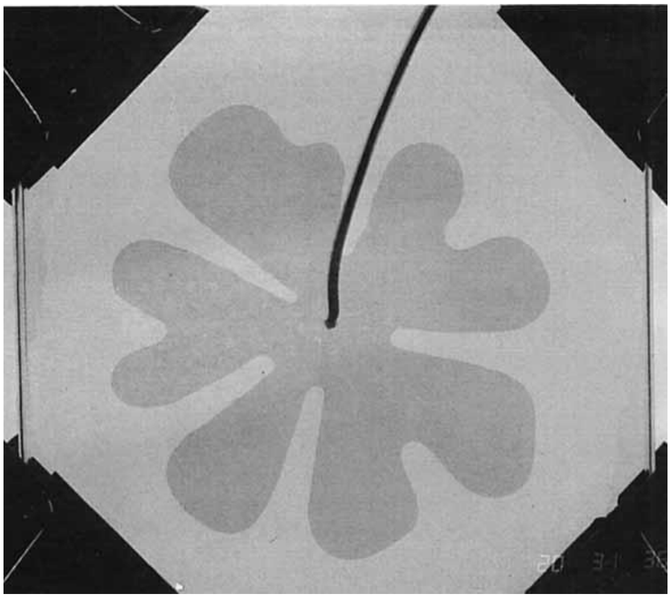

Figure 1.4. Radial pattern of viscous fingering when dyed oil is driving glycerine observed by Chen [39].

observations highlight that viscous forces tend to narrow the finger while the Capillary forces tend to widen it. However, Tabeling et al. did not observe a $\lambda_w = 1/2$ plateau in the λ_w vs. $1/B$ curve for large $1/B$ [6]. This deviation implies that another physical mechanism has to be taken into account, and the authors noticed that the curvature of the meniscus keeps changing with changing Ca.

Tabeling et al. (in 1987) also noticed that with an increasing gap thickness, the finger grows wider, but the plateau value remains the same again, unless for large $1/B$ [6]. Furthermore, they highlighted experimentally the apparition of a new phenomenon when the Capillary number is high enough. The finger tip splits into two new fingers; This pattern is so-called "tip-splitting". In the same year, Homsy defined the immiscible fingering processes as three basic growth mechanisms: spreading, splitting, and shielding [41]. Spreading and splitting have been observed at low and high Ca, respectively. The shielding phenomenon is the reason why there is usually only a single finger at low Ca. In shielding, since the mobile fingers tends to grow in the direction of the pressure gradient in the more viscous fluid, a finger slightly ahead of its neighbors quickly outruns them and shields them from further growth [41].

The usual law of λ_w following a unique curve when scaled with $1/B$ for small values of $1/B$ is still used for Newtonian viscous fingering investigations. However, some started to challenges the validation of such model. As an example, Moore et al. found that for high aspect ratio ($\delta > 250$) the mean finger width no longer scale as $1/B$ [42]. They observed the average finger width narrows at low $1/B$, while the maximum finger width increases. Moreover, they noticed that the finger-width fluctuation (i.e., the difference between the maximum and average finger width) follows a power-law with respect to the Capillary number in the form of $CCa^{-0.64}$, where C is a constant [42].

In a radial Hele-Shaw cell, when a displacing less-viscous fluid is injected, an early circular interface forms and then becomes wavy before several fingers eventually appear and develop symmetrically [43]. The pattern grows forming fingers by successive tip-splitting. When the flow rate increases, the interface becomes more unstable, and the number of fingers increases. The fingers become narrower and side-branching can occur. Side-branching is the apparition of secondary instabilities on the side of the fingers [43].

Paterson analyzed the linear instability of an expanding circular interface when an inviscid fluid is displacing an immiscible viscous fluid at a constant volumetric flow rate q in a Hele-Shaw cell [44]. He defined the most rapidly growing linearly unstable wavelength as a function of the interface radius, the outer fluid viscosity, the flow rate and the surface tension. Experimentally, it has been showed that as the flow rate increases, the fingers become narrower and more side branching will occur [43]. However, he also observed that interfacial tension disturbs the development of small-side finger. As a consequence, increasing the interfacial tension will stop the side-branched fingers from developing. In another work, Chen observed geometrically identical radial fingers patterns at the same dimensionless time and length scales [39]. More detailedly, the two patterns being similar, they present the same number of splitting as well [39].

Non-linear stability analysis reveals the role of sub-harmonic and harmonic perturbations at the onset of pattern formation such as the symmetry breaking [45]. Miranda and Widom theoretically showed that finger splitting in a radial flow geometry is driven by curvature of the unperturbed interface and may be controlled by adjusting this interfacial curvature [45]. They also investigated the relation between the interfacial asymmetry and a newly defined viscosity contrast, $\frac{\mu_2 - \mu_1}{\mu_2 + \mu_1}$ with μ_2 and μ_1 the viscosity of the pushed and driving fluids, respectively, in the Saffman-Taylor problem. They observed that the fingering pattern are becoming more complex with more asymetric instabilities as the viscosity contrast increases [45]. In short, Newtonian viscous fingering instability can generate a variety of patterns and morphologies. Additionally, new and complex patterns can be observed using non-Newtonian fluids, which will be discussed in the next subsection.

1.3.2 Non-Newtonian Fluids

Understanding the viscous fingering instability with Newtonian fluid is particularly essential to explain the fundamental physical phenomenon. However, nowadays, we observe an increase in using complex fluids, such as polymers or surfactants, in industrial applications, leading to research interest in Saffman-Taylor problems with complex, non-Newtonian fluids.

Generally, complex fluids are mixtures of two or more phases: solid-liquid such as suspensions or polymers, solid-gas such as granular mixtures, liquid–gas such as foams [46], or liquid-liquid such as emulsions [47]. Complex fluids exhibit unusual mechanical responses to applied stress or strain due to the geometrical constraints imposed by the phase coexistence. These fluids can be described as non-Newtonian and/or elastic fluids. A non-Newtonian fluid is characterized by not following a linear Newtonian viscosity law regarding the shear rate. For a Newtonian fluid, the shear stress (τ) linearly relates to the shear rate ($\dot{\gamma}$) as $\tau = \mu\dot{\gamma}$. In most cases, the viscosity of non-Newtonian fluids is not constant and can either increase for shear-thickening fluids or decrease for shear-thinning fluids with an increasing shear rate. The viscosity of a non-Newtonian fluid can be constant if the fluid requires finite yield stress to start to flow. In this particular case, it is called a Bingham fluid.

Furthermore, complex fluids can show elastic properties. The fluids can deform when stress is applied and come back to their original state after the release of the applied stress. Fluids exhibiting both elastic and viscous effects are characterized as viscoelastic fluids. In the following subsection, we will describe the work done on the Saffman-Taylor instability with some specific complex fluids.

1.3.2.1 Shear-Thinning, Shear-Thickening, and Flexible Polymers

Additive polymers can make complex fluids with interesting rheological behaviors. Here, we focus on three types of complex fluids made with polymers: shear-thinning, shear-thickening, and flexible polymers. Both shear-thinning and shear-thickening solutions show a strong shear rate dependence of the viscosity, but the normal stresses can be neglected. The fluid is said to be shear-thinning (shear-thickening) when the viscosity, μ, decreases (increases) with increasing shear rate, $\dot{\gamma}$. Changing the polymer concentration allows the complex fluid to change from weak shear-thinning (shear-thickening) behavior at low concentrations to strong behavior at high concentrations. The strength of the shear-thinning (shear-thickening) corresponds to the speed of the decrease (increase) of viscosity with respect to the shear rate. In contrast, flexible polymer exhibits strong elastic effects (i.e., normal stresses) while its viscosity is nearly independent of the shear rate.

As in the case of Newtonian fluids, Bonn et al. noticed that the finger width decreases with increasing the finger velocity for shear-thinning solutions in a rectangular Hele-Shaw cell [48]. However, the plateau value reached by λ_w (ratio of finger width over cell width) is smaller than that for Newtonian fluids. Moreover, this plateau value decreases with increasing polymer concentration. For low polymer concentrations, the finger width as a function of the parameter $1/B$ falls on the universal curve for if the shear-dependent viscosity of shear-thinning fluids replaces the constant viscosity of the Newtonian fluid, observed by Lindner et al. [49]. However, their results of the finger width start to deviate from the universal curve for greater polymer concentrations. The deviation is slight for small values of $1/B$ but more pronounced as the value of $1/B$ increases. The final key observation from Lindner et al. is that the fingers become narrower as the shear-thinning behavior becomes more pronounced.

The same phenomena is observed by Amar et al. with shear-thickening fluids, however, this time, fingers are wider than Newtonian fluids, and the plateau value at high finger velocity is more important than 1/2 [30]. Based on the findings by Lindner et al., anisotropy is likely to cause the finger to narrow or widen for the polymer solution [50]. Taking the example of a shear-thinning fluid, the fluid velocity is high in the region in front of the fingertip, leading to high shear rates and a small viscosity, whereas the viscosity is more important at the side of the finger. It results in the creation of a preferred growth direction and an anisotropy.

For flexible complex fluids, the evolution of λ_w is rather different than for shear-dependent complex fluids [48, 50]. For low polymer concentrations, λ_w decreases with increasing the finger velocity to reach a higher plateau value than the classical value of 1/2 of Newtonian fluids. For higher polymer concentrations, λ_w decreases first to a minimum and then increases to a plateau value that is again higher than 1/2. They reasoned that normal stresses are likely to cause the difference between the results for shear-dependent and flexible polymers. The normal stress cause thickening of the thin wetting film between the viscous finger and the glass plates of the Hele-Shaw cell. This extra pressure applied on the finger is accountable for the finger widening [48, 50].

Focusing on the effects of polymers solutions, some noticed that shear-thinning (shear-thickening) behavior significantly modifies the morphology of the viscous fingering pattern [51, 52]. Generally, the viscous fingering pattern for shear-thinning and shear-thickening fluids depends on four dimensionless groups: the mobility ratio, the Capillary number, the Deborah number, and the power-law index or the strength of the shear-thinning (shear-thickening) [52]. Fast et al. noticed for shear-thinning fluid, there is a delay or even a suppression on the splitting at the tip of the finger. The delay or the suppression of such a phenomenon depends on the strength of the shear-thinning behavior. At high Capillary numbers, the growth of shorter wavelengths is enhanced, leading to more pronounced side branching [51, 52]. As a result, dendritic structures can occur. These trends are only true for a small Deborah (De) number, shown by Lee et al. [53]. The Deborah number is the ratio of the time it takes for a material to adjust to applied stresses or deformations over the characteristic time scale of an experiment. They noticed that as De further increases, new fingers are developed via multiple-tip splitting and side branching, resulting in more complex interfacial structures. Interfacial instabilities also set in at an earlier time for high values of De.

For shear-thickening solutions, an apparent change in viscous fingering patterns with increasing De is also observed [53]. First, larger values of De tend to attenuate the instability, resulting in an almost stable interface. This pseudo-stability does not last long as stronger interfacial instabilities develop when the Deborah number further increases. The interface becomes less unstable, and tip-splitting is delayed when the shear-thickening behavior is weak. However, interfacial instabilities start to grow again and become stronger when shear-thickening is getting stronger [53].

1.3.2.2 Surfactants

The addition of surfactants into a fluid creates a surfactant solution which can show complex non-Newtonian behavior. Some surfactant solutions have been used to study viscous fingering. Visually, the addition of surfactants has an effect on the unstable interface obtained due to the Saffman-Taylor instability. The propagating VF finger is typically wider with surfactants in a rectangular Hele-Shaw cell [54]. Just as in the case of Newtonian fluids, the relative width of the finger decreases until reaching a plateau, noticed by multiple authors [48, 50, 54]. However, the observed plateau value is larger than half the cell width. At low surfactant concentration, the evolution of the relative width (λ_w) with respect to the finger velocity is surprising. First, λ_w decreases until reaching a minimum and then increases towards the plateau value. Both the evolution of λ_w and the plateau value depend on the surfactant's concentration [48, 50, 54]. The widening of the finger is due to an anisotropic surface tension. During the viscous fingering experiment, the hydrodynamic flow sweeps away the surfactant film from the tip to the back of the finger whereas the interface is supplied with fresh surfactant by molecular diffusion from the bulk. The consequence is an anisotropic surface tension, which decreases from the tip to the back of the finger, inducing a widening of the finger [48, 50, 54].

Surfactants can be added to another complex fluid as well. It has been observed by Ahmadikhamsi et al. that the injection of surfactant solutions affects fingering competition and tends to produce fewer and broader fingers [55]. However, as the instability grows, the fingertip is propagating away from the injection source, and the shear-thinning viscous fluid behavior seems to prevail. As a consequence, the surfactant solutions recover the same relative finger width as for the pure high-viscosity polymer [55].

1.3.2.3 Colloids and Suspensions

Some investigations on viscous fingering have been done using colloidal or suspensions solutions. Starting with colloidal solutions such as clay water solution, different patterns of interfacial instability are observed by Van Damme et al. and Lemaire et al. [56, 57]. On the one hand, they noticed that the patterns are typical viscous fingering patterns with side-branching and tip-splitting at low flow rate. On the other hand, the fingers resemble cracks at high flow rates and have a sharp tip. The transition between these two different regimes depends on the concentration of clay and the flow rate [56, 57].

For a water/clay paste displacement, the radial fingering development is intrinsically a fractal growth process [58]. The interface between the two fluids is, in fact, a water/water interface. Hence, the interfacial surface tension between the fluids is zero, and fractal patterns with numerous tip-splitting and side-branching are easily obtained. Moreover, the displacement efficiency is no longer a value dependent on the width of the finger. For colloidal solution, it is almost totally dominated by the branching, or tip-splitting cascade of the fingers [58].

Two critical parameters for suspension flows are the initial volume fraction of particles and the ratio of gap thickness to particle diameter. The distribution of suspensions is uniform at low volume fraction; there are no deformations of the interface [59]. Whereas when the volume fraction increases, the particles accumulate on the meniscus and form clusters. This increase in particle concentration correlates to the rise in the effective suspension viscosity. The consequence of this increase in viscosity is the deformation of the interface, resulting in miscible viscous fingering beyond a critical value of particle concentration. The forming fingers are hence short and large, observed by Xu et al. [59]. The same type of fingers can be observed by doing experiments in a Hele-Shaw cell with an elastic membrane (See Fig. 1.6). In brief, the key to particle-induced viscous fingering is the unfavorable viscosity difference of a less viscous fluid invading a more viscous one [59]. This viscosity difference is caused by the non-uniform distribution of particles. Finally, the interface is deforming due to a greater flow resistance through the viscous suspensions clusters relative to the surrounding medium [59].

Luo et al. show another type of wider fingers using suspensions solutions [60]. They are called band fingering and result from a very dense concentration of suspensions at the interface inside the band. This way, the band resistance to the flow is entirely different from the rest of the solution with dilute suspension. A condition to observe band fingering is that the ratio between the Hele-Shaw cell gap thickness and the diameter of the suspension particles must not exceed a critical value equal to 5 [60].

1.3.2.4 Yield-Stress Fluids

Complex fluids that require finite yield stress to start to flow are called yield stress fluids. The shear stress of such fluids follows the Herschel-Bulkley law $\tau = \tau_c + \kappa\dot{\gamma}^n$. τ_c, κ, $\dot{\gamma}$ and n corresponding to the yield stress, the consistency index, the shear rate, and the power-law index, respectively [61]. When $n = 1$, it corresponds to a Bingham fluids. Studies about viscous fingering with yield-stress fluids have been done in static Hele-Shaw cells, as well as lifted Hele-Shaw cells [62, 63].

When a wetting yield-stress fluid is displaced by air, three different finger structures have been observed [64, 65, 66, 67]. Firstly, ramified structures are observed at low velocities. The process initially starts with a finger whose tip quickly splits, and hence asymmetric fingers are formed. The splitting continues until a ramified structure is obtained (See Fig 1.5). The finger-width does not depend on the propagation velocity, according to Eslami et al. [67]. However, the finger width does increase with increasing the gap thickness. Since the yield stress dominates over the viscous stress at low finger velocity, thereby in the yield-stress regime.

Secondly, the vicious regime where a single but narrow finger is observed at larger velocities is reached. The shape of the finger is very similar to the classical viscous fingering of Newtonian fluids (See Fig. 1.5). This regime will be named the viscous regime. Similar to the cases for Newtonian fluids, the yield-stress fluid's finger width decreases with fingertip velocity, noticed by Eslami et al. [67]. However, as in the cases of the shear-thinning fluids, the relative finger width λ_w plateau value is significantly below the limit of $\lambda_w = 0.5$ found for Newtonian fluids. Lindner et al. found that the evolution of the finger width follows a curve scaling as $Ca\delta$ rather than $1/B = Ca\delta^2$ with δ, the aspect ratio [64]. This shows that the dependence on Ca is stronger or the dependence on δ is weaker than for the Newtonian case. Moreover, in this regime, tip-splittings are suppressed.

Thirdly, the authors observed fractal patterns at high speeds [64, 65, 67]. In the elasto-inertial or side-branching regime, there is usually an asymmetric finger in the middle of the channel with secondary instabilities at the finger sides, leading to a side-branching structure (See Fig. 1.5). The side-branched fingers are attributed to the elastic effects of the yield-stress fluid [67]. Moreover, they found that the finger width decreases and then increases drastically until reaching a plateau value in this regime.

In the cases of non-wetting yield-stress fluid displaced by oil, a different regime or pattern has been observed by Eslami et al. with a wide finger with a smooth and uniform interface formed at very low velocity [68]. This pattern corresponds to the capillary regime due to the importance of interfacial tension stresses at very low velocities. In this regime, the finger width seems to be constant. The limits between the yield-stress and the viscous regimes has been expressed in terms of modified Capillary number (Ca^*) and Bond number (Bo^*) for all rectangular channels either the gravity is neglected or not [68, 69].

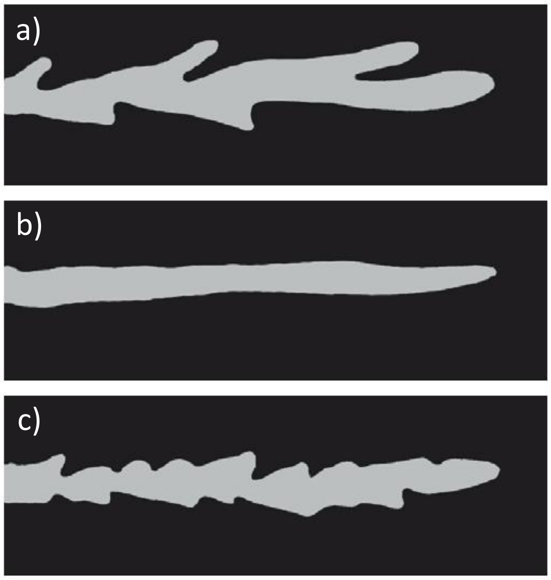

Figure 1.5. Viscous fingering pattern of using Yield stress fluids in a rectangular, flat Hele-Shaw cell, captured by Eslami et al. [67]. (a), (b), and (c) correspond to the yield-stress, viscous, side-branching regimes, respectively.

Besides the impact of finger velocity on the fingering pattern, discussed above, the gap thickness has an impact [69]. When the gap thickness increases, resulting in increasing buoyancy, the finger goes from the yield stress-dominated regime to one in which buoyancy dominates, where a unified wide finger is observed. An opposite effect than the gap thickness and the finger velocity is noticed with the cell width. For small width values, the unified wide finger is observed while the finger is destabilized at higher values. The appearance of the ramified fingering pattern is due to the dominance of the yield stress over the other forces, according to [69]. However, for important values of Bo^* (Ca^*), the buoyant (viscous) stress dominates, resulting in the unified fingering pattern. The modified Capillary number and Bond number being expressed as $Ca^* = \frac{Ca}{Bn}$ and $Bo^* = \frac{Bo}{\delta}$, with Bn and δ the Bingham number and aspect ratio, respectively. The ramified finger is observed by the authors at small values of Bo^* and Ca^*. In contrast, the unified fingering can be investigated when Bo^* is superior to a critical value, regardless of the value of Ca^*. A similar transition happens when Ca^* is superior to a critical value. Finally, both the yield stress and the geometrical properties of the channel have an impact on the pattern evolution [69].

Other studies with yield-stress fluids has been done this last few years. Most notably, Coussot did a linear stability analysis for flows of yield-stress fluids through an uniform radial Hele-Shaw cell [70]. In the cell, the interface between a pushing Newtonian fluid and a driven yield stress fluid will be stable if $\tau_w > \frac{2\gamma h}{r_0^2}$, with the τ_w the shear stress at the wall expressed as $\tau_w = \tau_c[1 + c(\frac{\kappa U^n}{\tau_c h^n})^d]$, where c and d two parameters which depend on n, the power-law index in the Herschel -Bulkley law [70].

1.4 Miscible Viscous Fingering in a Hele-Shaw Cell

In addition to the viscosity or mobility ratio, the Peclet number (Pe) plays an important role in miscible fluid displacement in a Hele-Shaw cell. The Peclet number corresponds to the ratio between inertia and diffusion. This dimensionless number is expressed as $Pe = \frac{hU}{D}$ for a rectangular cell of gap thickness h, with U and D, the flow velocity and the mass diffusion coefficient, respectively. An increase of the Peclet number almost always acts to increase interfacial instability, where an increase of the mobility ratio increases the growth rate of perturbations just like immiscible viscous fingering [71, 72]. Previous studies noted that advection is necessary for viscous fingering, but diffusion stabilizes the interfacial instability in miscible systems. Linear stability analyses have been performed for rectangular [71] and radial Hele-Shaw cell [72] to study the interfacial stability of miscible viscous fingering. Ledesma et al. showed that the interface between the two miscible fluids remains stable for low Capillary number and Peclet number, when surface tension and diffusion dominate over viscous stresses and advection, respectively [71]. For radial geometry, the stability is achieved for low values of Peclet number and the mobility ratio [72]. Moreover, Fu et al. observed that fluid dissolution or exsolution due to partial miscibility can either hinder or enhance viscous fingering, respectively [73].

Overall, like immiscible viscous fingering, the phenomena of shielding, spreading, and splitting are all important in determining the fingering dynamics in miscible displacements. However, the miscible fingering patterns can be somewhat different from those of immiscible

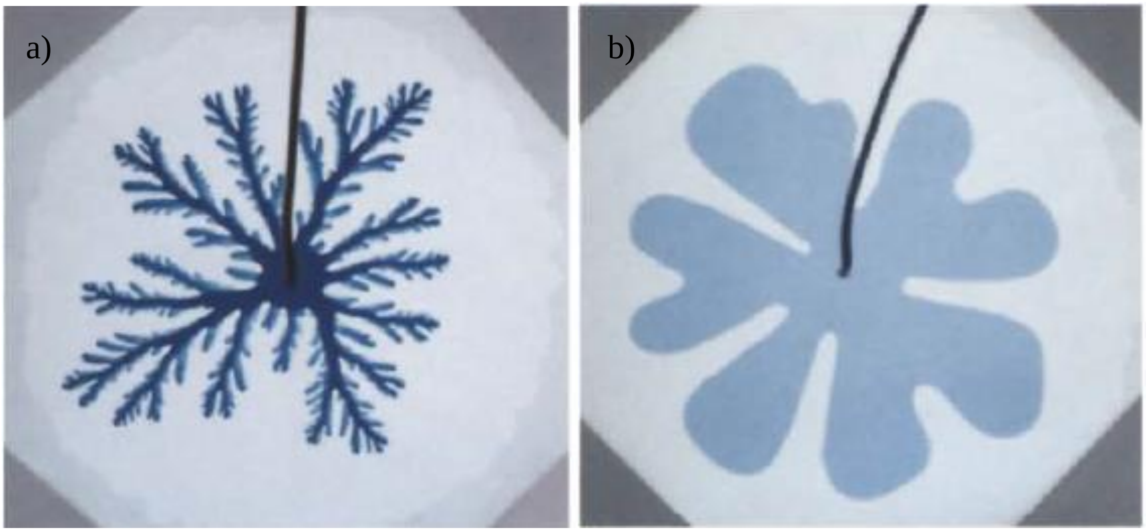

Figure 1.6. Radial patterns of miscible and immiscible viscous fingering in a identical Hele-Shaw cell at the same flow rate. a) Miscible displacement: dyed water is drivig glycerine b) Immiscible displacement: dyed oil is pushing glycerine by Chen [43].

ones, as observed many authors [39, 41, 43, 74]. The number of splitting is much more, and the size of the fingers is much less for miscible displacement (See Fig. 1.6). Maes et al. differentiated two different regimes of fingering patterns or shapes [16]. One is an advective regime where the length of the finger is proportional with time, and the other is a dispersive regime where the finger length evolves as a square root of time. The Peclet number is the essential parameter to determine which regime dominates [16].

At larger Peclet number and mobility-ratio, exciting and complex behavior are observed [41, 72]. Maes et al. showed that the larger the mobility ratio or the injection speed, the larger the distortion of the sample [16]. They observed more tip-splitting happening, and the viscous fingering can form a dendritic pattern. Other mechanisms become dominant for miscible fluids at high viscosity ratio. These non-linear effects are double coalescence, side-branching, gradual coalescence, single-sided tip-splitting, stretched coalescence, trailing lobe detachment, alternating side-branching, and skewering. All these mechanisms have been observed by Sesini et al., and they added that dense branching is the reason for the complexity of the fingering patterns of miscible displacement in comparison with immiscible displacement [75].

1.5 Controlling Viscous Fingering

It is vital to control viscous fingering, suppress it, or enhance it to increase the potential efficiency of industrial applications. Theoretical studies are essential in helping industries to decide the best injection rate, the best geometry, or the best fluid to use for the application. Different methods have been studied to control this interfacial instability. Firstly, one of them is the use of a time-dependent variational scheme for the flow rate instead of a constant flow rate. It has been found effective both theoretically and experimentally [76, 77, 78, 79]. Secondly, another way is to modify the geometry of the setup. Using a Hele-Shaw cell modified with edged pattern, dendritic or chaotic fingering is observed for both miscible or immiscible VF by Chen [43]. Thirdly, the use of a Hele-Shaw cell that can be lifted has an impact on the interface stability for both Newtonian and a power-law complex fluid by Amar and Bonn [80]. Fourthly, having a structured porous media with a pore size gradient or a deformable porous media by adding beads in a Hele-Shaw cell are imaginative ways to control viscous fingering [81, 82]. The presence of Capillarity in the porous medium increases the capillary forces and plays a positive effect on the stability by slowing down the growth of VF instabilities [83]. Finally, adding a low dose of nanoparticles can help to control the flow [84]. Among all the different solutions possible to control the Saffman-Taylor instability, we will focus on using a tapered plate and an elastic membrane in Hele-Shaw cells.

1.5.1 Utilization of a Tapered Hele-Shaw Cell

The use of converging or diverging tapered Hele-Shaw cells has been a significant research subject for the past decade. The apparition of a gap gradient can either negatively affect the propagation of the instability or can enhance the fingering phenomenon. Al-Housseiny and Stone [78] derived theoretically a stability criterion for Newtonian fluid in rectangular and radial geometry with a gap gradient: α. Using the depth-averaged Darcy law and the mass conservation to perform linear stability analysis, they found the two stability criterion. For the rectangular geometry, it is $1 - \lambda + \frac{2\alpha cos\theta_c}{Ca} \leq 0$ where λ is the viscosity ratio of the pushing fluid over the receding fluid, and θ_c is the contact angle of the wetting fluid. From this expression, they were able to estimate a critical Capillary number at which the interface undergoes a change in stability. For the radial geometry, the interface is always stable, for all perturbation's wavenumber, if $1 + \frac{2\alpha + h_0^2/r_0^2}{Ca} < 0$ where this time r_0 and h_0 correspond to the radius of the interface and the gap thickness in the Hele-Shaw cell at the interface.

These criteria have been put to the test experimentally by Housseiny et al. and Bongrand et al. for rectangular [85] and radial geometry [86] and show good agreement. From the experiments and the theory, it is possible for the interface to become stable when the cell becomes shallower. However, above the critical Capillary number, the interface destabilize and fingers are forming. Housseiny et al. noticed that the fingers are wider than half the cell, the plateau obtained for the usual homogeneous Hele-Shaw cell [85]. Moreover, using the same converging cell, they demonstrated the possibility to destabilize an interface even when it should be stable in terms of the viscosity ratio.

Anjos et al. performed a nonlinear analysis of the viscous fingering patterns in tapered (converging and diverging) and flat radial cells and found that the interface is stabilized at lower Ca in a converging cell, compared to the case of the uniform cell interface [87]. However, they noticed that the interface is even more destabilized than homogeneous cells at higher Ca. Interestingly, the effects are exactly reversed in the diverging cell cases. In addition, the shape of the finger does not change from converging to diverging cell. They observed fingers with round tips at low Capillary number. The tips are flattened when the dimensionless Ca increases, and tip-splitting will occur above a specific value of Ca. This nonlinear analysis [87] shows good agreement with a recent numerical simulation by Jackson et al. [88].

The studies of complex fluid displacement in a tapered Hele-Shaw cell are recent and rare. The topic of complex fluid displacement in a flat Hele-Shaw cell has be investigated for decades but never in the idea of controlling the Saffman-Taylor instability.

Eslami et al. experimentally noticed two pattern structures when using a rectangular tapered cell [89]. They observed, on one hand, a ramified structure pattern with several asymmetric air fingers that frequently splits. On the other hand, a single narrow viscous finger in the middle of the cell at higher velocities [89]. The critical velocity characterizing the transition between the two patterns of finger being dependent on the gap gradient, α. Moreover, the finger becomes wider and narrower in the diverging and converging cells, respectively, compared with the case of flat Hele-Shaw cells [89].

They justified that observation saying that in a converging cell, the finger starts moving slowly through but speeds up as the cross-section becomes narrower. Consequently, as the finger tip velocity increases, its local width decreases. In the diverging configuration, the presence of a positive gap gradient leads to the opposite scheme. In the presence of a gap gradient, the cross-sectional area of the cell increases or decreases in the flow direction. It results in the finger tip velocity to decrease (increase) in the diverging (converging) cell but also affects the surface tension at the tip of the finger, which can modify the flow patterns in the nonuniform cells [89].

Similar to the cases with Newtonian fluid, the converging cell has a stabilizing effect on the interface at lower velocities or Capillary number for complex yield-stress fluids. The mean finger width in the converging cell is larger than that in the diverging cell [89]. However, the roles are swapped between converging and diverging cells after a critical velocity or Capillary number. Finally, they observed that the flow pattern becomes nearly independent of the gap gradient as the velocity reached a critical value, when the viscous stresses starts to dominate the flow. The same transition is observed for uniform cell [68]. The method of using Hele-Shaw cell with a gap gradient to control the viscous fingering is still an active research topic nowadays.

1.5.2 Utilization of an Elastic Membrane

Wall elasticity can affect the onset of the instability. As a consequence, modified Hele-Shaw cells replacing one of the plates by an elasic sheet has been used, and elastic boundaries are effective to delay the onset of viscous fingering. It has been proven theoretically [90] experimentally and observed with numerical simulations [91, 92] that at low radius and low flow rate, the viscous fingering instability can be suppressed in a Hele-Shaw cell with elastic membrane. They found three reasons for this phenomenon. First, a decrease of the velocity of the fluids interface because a fraction of the injected volume is accommodated by the deflection of the elastic upper boundary. Secondly, as the fluid is injected, the membrane will deform and tends towards creating a converging tapered geometry. The Hele-Shaw upper plate will inflate starting by the center, implying that the gap thickness will decrease in the direction of the flow. With this taper, the destabilizing effects of an increase (decrease) in the driving pressure gradient are counteracted by the variation, decrease or increase in the gap thickness. The final stabilizing effect is that with the modification of the interface curvature, Pihler et al. observed an increase in the stabilizing capillary forces [92].

The wall elasticity equally impacts the structure of the fingers that develop. Using this particular Hele-Shaw set-up, less or almost zero tip-splitting and no dendrite form has been observed [91]. The entire interface propagates so that a large number of very short fingers grow. This type of interfacial instability is reminiscent of the printer's instability [91]. In another work, Pihler et al. argued that the severity of the Saffman-Taylor instability is impacted by the wrinkling instability of the membrane [93]. A non-dimensional number, I, is defined as the ratio of the typical viscous stresses in the fluid to the bending stiffness of the elastic membrane. This number provides a measure of the importance of the fluid-structure interaction. It has already been used by Pihler et al. to study the competition and interaction between the Saffman-Taylor instability and the wrinkling instability of the membrane [92]. An increase in I increases the transverse deflection of the membrane. This deformation weakens (and ultimately suppresses) the viscous fingering instability. However, for sufficiently thin membranes, an increase of the parameter I leads to an earlier onset of wrinkling and an increase in the severity of the fluids' interfacial instability [92].

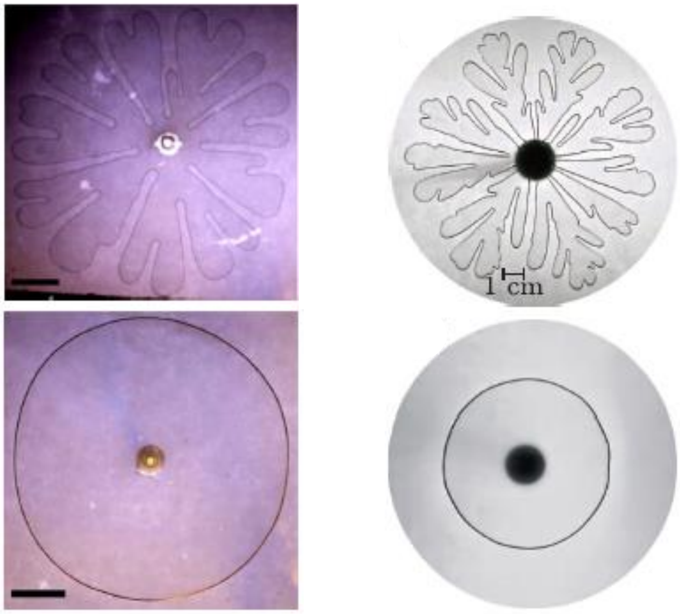

Figure 1.7. Suppression of viscous fingering due to a change of cell geometry. On the left hand side, effect of a converging gap gradient [86]. On the right hand side, impact of the addition of an elastic membrane [93].

1.6 Overview of the Thesis

The primary objective of this thesis work is to give a better understanding of the viscous fingering phenomenon for complex, yield-stress fluids. We use both radial and rectangular heterogeneous porous media of modified Hele-Shaw cells. In Chapter 2, we perform experiments with an inviscid, Newtonian fluid pushing a yield-stress fluid in rectangular tapered cells. We also carry out linear stability analysis using an effective Darcy's law model. Our first study investigates the control of viscously-unfavorable fluid-fluid immiscible displacements of a yield-stress fluid by a Newtonian fluid in rectangularly tapered Hele-Shaw cells. We study the flow stability diagram of the viscous fingering instability depending on the flow rate, depth gradient, the interface coordinates. We compare our experimental results with the stability criterion derived theoretically. Subsequently, in Chapter 3, we investigate very similar complex fluid displacement to the first study, but we extend the both experiments and theory to a radial tapered Hele-Shaw cell. In Chapter 4, we investigate the impact of the Bingham number on the interface stability by performing a more complex linear stability analysis within the boundaries of a radially tapered Hele-Shaw cell.

Chapter 2

Controlling Viscous Fingering of Complex Yield-Stress Solutions in a Tapered Rectangular Hele-Shaw Cell

1

2.1 Introduction

Occurring in many natural and industrial processes, the displacement of a more viscous fluid by a less viscous one is common in many applications such as coating flows [8, 12, 13], chromatographic separation [11], printing devices [7], oil well cementing [94], enhanced oil recovery (EOR) [19, 22] or even CO_2 sequestration [24, 25, 26]. However, the unfavorable mobility or viscosity contrast in a porous medium leads to an interfacial instability between the two fluids. This instability manifested in a fingering shape is responsible for a loss of efficiency in many industrial applications. This viscous fingering or Saffman-Taylor instability has been extensively studied for decades with Hele-Shaw cells, used to simulate

---

[1] The material presented in this chapter is based on a manuscript in preparation by Alban Pouplard and Peichun Amy Tsai, "Control of Viscous Fingering Instability of Complex Yield-Stress Fluids using a Rectangular Tapered Cell Geometry," in preparation, 2021.

a homogeneous porous medium [5, 40, 41, 43, 44, 74]. In recent years, the studies have been extended to complex fluids whereby more complex and wider fingers are observed [49, 54]. With yield-stress fluids, a new pattern of side-branching fingers has been observed with smaller fingers forming to the side of the major one [50, 67, 68, 70].

To increase the efficiency of the aforementioned industrial processes, the control or inhibiting of the viscous fingering is essential. Several strategies have been studied recently to suppress the fingering instability for simple Newtonian fluids. Some examples include the use of time-dependent flow rate [76, 77, 79], an elastic membrane as the top plate of a Hele-Shaw cell [90, 91, 92], or a tapered cell [78, 85, 86]. However, such control has never been investigated for complex fluids, which are commonly present in industrial settings. Very recently, it has been showed that for a yield-stress fluid the side-finger appearance can be affected by the addition of a converging or diverging gap gradient [89], but the total annihilation of the perturbation and total sweep efficiency have never been achieved yet.

In this chapter, using a rectangular tapered Hele-Shaw cell, we examine the possibility of inhibiting the primary viscous fingering instability of complex, yield stress fluids in a narrow confinement. First, we investigate the effects of flow rates and depth gradients on the Saffman-Taylor instability with experiments of a gas pushing a yield-stress, shear-thinning fluid. Secondly, we theoretically derive a linear stability criterion generalized for two complex yield-stress fluids pushing one another in a gap-converging cell. Finally, using the experimental results of interface velocity and gap thickness, good agreement between the theoretical stability criterion and the experimental results is found.

2.2 Experimental

Three different aqueous solutions of PolyAcrylic Acid solution (PAA, SigmaAldrich, $M_w \approx 1,250,000$) were prepared and used as a wetting yield-stress fluid to investigate complex fluids' viscous fingering. PAA is a water-soluble polyelectrolyte and widely used as a fluid thickener and a dispersing, suspending, and emulsifying agent in pharmaceuticals and cosmetics [95, 96]. For the experiments, we first fill in one complex PAA solution in a rectangular

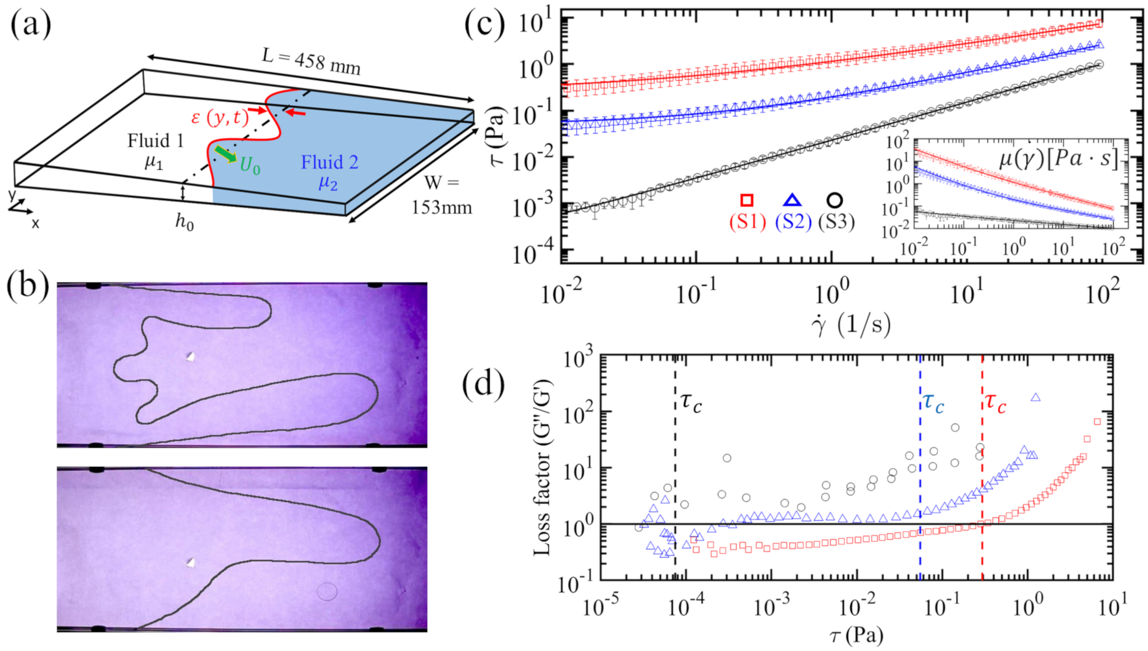

Figure 2.1. (a) Schematics of a fluid-fluid displacement experiment where one more viscous complex fluid (of viscosity, μ_2, varying with shear rate, $\dot{\gamma}$), is pushed by another immiscible one. The cell length and width are L = 458 mm and W = 153 mm, respectively. (b) Experimental snapshots of complex viscous fingering produced by a complex yield-stress (PAA) solution (S2) displaced by a gas injected with a flow rate Q = 0.2 slpm and Q = 0.02 slpm in a flat Hele-Shaw cell. (c) Flow curves of shear stress (τ) and viscosity (μ), depending on the shear rate ($\dot{\gamma}$) for the three complex yield-stress fluids: (S1, □), (S2, △), and (S3, ○). The lines correspond to the Herschel-Bulkley model parameters fitted to data. (d) Oscillation amplitude sweep test at constant frequency ($\hat{w}$ = 1 rad/s). Loss factor, ratio of the loss modulus (G'') to the storage modulus (G') with respect to the shear stress (τ). The dashed lines represent the yield stress values of the fluids.

Hele-Shaw or tapered cell and subsequently inject a gas (nitrogen, viscosity $\mu_1 = 1.76 \times 10^{-5}$ Pa.s at 20 ° C) as a pushing fluid (see Fig. 2.1(a)). The gas is injected at a constant flow rate, Q, ranging from 0.02 slpm to 2 slpm (Alicat mass flow controller) with an accuracy of 1 ml/min.

The three aqueous solutions of PAA are prepared to obtain various viscosity contrast, λ, spanning $4.47{\times}10^4 - 1.68{\times}10^6$, $1.55{\times}10^4 - 2.64{\times}10^5$, and $5.83{\times}10^2 - 3.13{\times}10^3$ for the complex fluids (S1), (S2), and (S3), respectively. The procedures of preparing the solutions include, first, slowly adding the polymer powder in water and, subsequently, stirring the mixture at high speed for 1 hr. The mixture generates an acid solution that can be neutralized using a basic solution. To do so, sodium hydroxyde (NaOH) is added to the solution and then stirred for another 10 hours at medium speed. Finally, after the agitation, the solution is rest for a day before performing any rheological measurements.

The rheological measurements of the three complex solutions with a rheometer (Anton-Paar MCR302) are presented in Fig. 2.1(c). Neglecting the elastic properties, the common rheological model of the Herschel–Bulkley (HB) model [61] reveals an excellent fit of the shear stress (τ) varying with shear rate:

$$\tau = \tau_c + \kappa\dot{\gamma}^n, \tag{2.1}$$

with τ_c, κ and n corresponding to the yield stress, the consistensy index, and the power-law index, respectively. The fluid's viscosity (μ) varying with $\dot{\gamma}$ and its variation is well described by the corresponding HB model with $\mu = \frac{\tau_c}{\dot{\gamma}} + \kappa\dot{\gamma}^{n-1}$. Shown in Table 2.1 are the best nonlinear fit results of the rheological measurements of $\tau = f(\dot{\gamma})$ from our three complex solutions for the experimental range of $\dot{\gamma}$ (between 0.014 and 93 1/s). Overall, all the complex solutions are shear-thinning, with decreasing viscosity with increasing shear rate $\dot{\gamma}$, i.e., $n < 1$.

Yield-stress solution	PAA (wt %)	NaOH (wt %)	τ_c (Pa)	κ (Pa.s^n)	n
(S1)	0.025	0.0106	0.2940	0.8641	0.4623
(S2)	0.10	0	0.0552	0.1442	0.6286
(S3)	0.015	0.008	7.51e-5	0.0231	0.8208

Table 2.1

Rheological parameters found for the three complex, yield-stress fluids with the HB model [Eq. (2.1)].

Oscillation amplitude sweep tests at constant frequency ($\hat{\omega}$ = 1 rad/s) is perform to validate negligible elasticity of the complex fluids. In Fig. 2.1(d), the results of the loss factor, the ratio of G'', the loss modulus, representing the viscous properties of the complex fluids over the storage modulus G' corresponding to the fluid elasticity is plotted with respect to the shear stress τ. When the G''/G' is more important than the unity, the viscous behavior prevails while the elasticity of the fluid is prevailing when the ratio is less than 1. The dashed lines in the figure represent the values of the yield-stress for the fluids (S1), (S2) and (S3). We will only focus on the fluids when they are flowing, i.e, $\tau > \tau_c$. Whenever this condition is respected, The loss factor is more or less superior to 1, meaning the viscous prevails. From this observation, we are able to neglect the elastic effects of the three complex yield-stress fluids.

During our experiments, a rectangular cell consisting of two glass plates with a converging gap is used to control the interfacial instability (see Fig. 2.1(a)). Spacers of different thickness (ranging from 0 to 23.0 mm) are placed at the four corners to form a taper with a negative gradient, $\alpha = dh(x)/dx$, the ratio of the height to length of the tapered area. The plates are surrounded by rubber bands to make an hermetic set-up. The gap thickness inside the cell evolves linearly as $h(x) = h_e + \alpha x$, with h_e the gap thickness at the edge of the cell, where the thicker spacers are placed and the thickness of cell gap is greatest. The experimental snapshots are captured, via bottom view, with a camera (Canon EOS 70D) at 30 fps (frames per second). To enhanced contract at the interface, a light is placed and used above the cell. We use ImageJ and Matlab to analyse the experimental snapshots and track the interface position. The interface velocity, U_0 is calculated by deriving the interface position over a short period of time (t). The values of h_0 and α are determined from image analysis using the values of the interface velocity (U_0) and flow rate (Q). The Reynolds number in our experiments ranges from 4.27×10^{-4} to 10.9 and the corresponding cell permeability values are between 2.08×10^{-8} and 1.77×10^{-5} m^2.

2.3 Results and Discussions

Using flat and tapered rectangular Hele-Shaw cells, we performed approximately 550 experiments of viscous fingering. With the flat Hele-Shaw cell of a constant gap thickness, we always observe unstable interface with one or multiple fingers of the complex fluid developing at the interface, consistent with previous similar observations using more viscous complex fluids [67, 68]. Shown in Fig. 2.1(b) are two representative snapshots obtained in our ex-

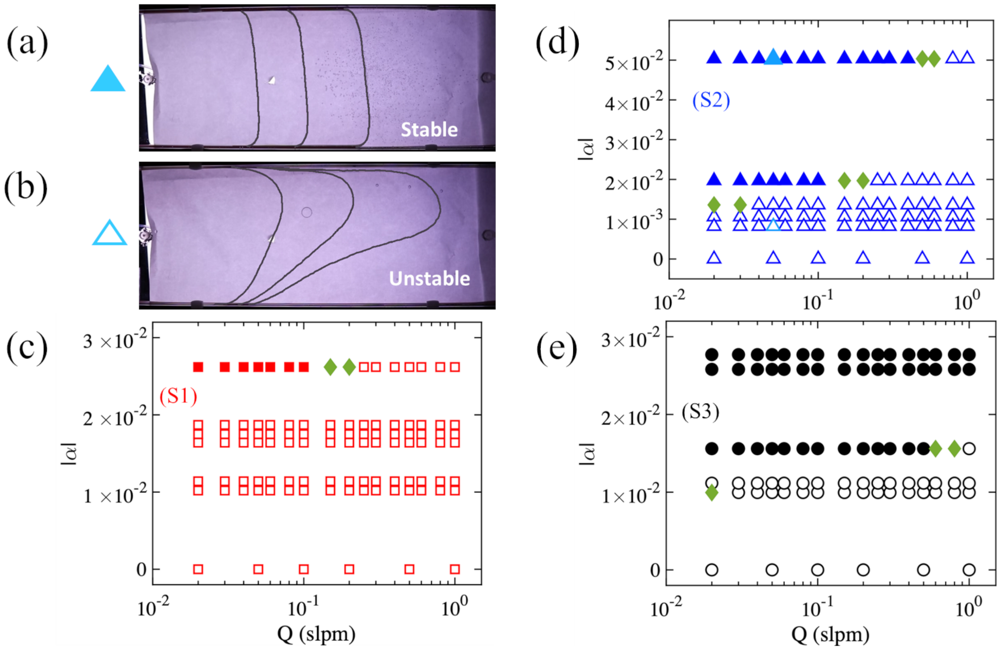

Figure 2.2. **Control of complex viscous fingering** using a rectangular tapered cell, with a linearly varying gap thickness ($h = h_e + \alpha x$), demonstrated by the overlay of experimental snapshots from a stable and an unstable displacement in (a) and (b), respectively. (a) the stable displacement is obtained when nitrogen is pushing complex fluid (S2) in a tapered Hele-Shaw cell with $h_e = 23.24$ mm, $\alpha = -5.03e{-}2$ and $Q = 0.05$ slpm. The time step between the snapshots is $\delta t = 100$ s. (b) the unstable displacement is observed when a gas is pushing complex solution (S2) in another tapered Hele-Shaw cell with $h_e = 3.76$ mm , $\alpha = -8.20e-3$ and and $Q = 0.05$ slpm. The time step is equal to $\delta t = 20$ s. (c), (d), and (e) are experimental results of stability diagrams for fluids (S1), (S2) and (S3), respectively, with uniform stable (■, ▲ and ●) vs. fingering/wavy unstable interfaces (□, △ and ○) under various Q and α values. Finally, green diamonds (♦) correspond to the transitional state where the interface starts to develop a wavy profile.

periments when the complex yield-stress fluid (S2) is pushed by nitrogen at a constant flow rate $Q = 0.2$ slpm and $Q = 0.02$ slpm, respectively. Furthermore, for the two more viscous fluids (S1) and (S2) and with greater flow rates, small fingers are forming on the side of the major one. This observed pattern corresponds to the side-branching regime [65] or the elasto-inertial regime [67]. The side-fingering pattern is observed when the injection flow rate is above a critical value, Q_c. For our fluids, $Q_c = 0.5$ slpm for (S1), whereas $Q_c = 1$ slpm for (S2).

By contrast, we do not observe the side-branching patterns when the converging cells are used. Instead, the interfacial patterns observed either resembling the usual viscous fingers with Newtonian fluids or stable interface, which occurs at a low flow rate but depends on viscosity contrast and depth gradient. The critical flow rates, below which we observe a stable displacement, for each complex fluid and α are summarized in Fig. 2.2(c-e). The stable displacement being characterized by a perfect sweep efficiency as illustrated by Fig. 2.2(a). Such inhibition of the primary viscous fingering instability is only possible for suitable rheological and flow parameters, as revealed by the stability phase diagram of Fig. 2.2(c-e) for the complex fluids (S1) to (S3), respectively. The essential experimental finding includes, for all the fluids (S1) to (S3), stable interfaces are observed for higher flow rate (Q) as the gap gradient ($|\alpha|$) increases. For a constant gap gradient, the stable interfaces occur at low Q. These similar trends concerning the phase diagrams in Fig. 2.2 have been observed in previous investigation of viscous fingering using Newtonian fluids [86].

Here, we differentiate three types of experimental results made using the complex fluids: first, uniform and stable displacements represented represented by filled symbols (S1, ■), (S2, ▲), and (S3, ●); second, unstable displacements with fingering or wavy interfaces by open symbols: (S1, □), (S2, △) and (S3, ○); third, the transitional state when the interface starts to develop a wavy profile (♦ for all the fluids). The contrast between the stability diagrams of the three different complex solutions highlight not only the complicity of controlling complex viscous fingering but also the importance of rheological parameters via τ_c, κ, n, and the local shear rate ($\dot{\gamma}$).

2.4 Theoretical Background

To obtain a better understanding of the important parameters to control the viscous fingering instability of complex fluids, we carry out a linear stability analysis using two yield-stress, complex fluids (Fluid 1 pushing Fluid 2) of viscosity μ_1 and μ_2, respectively, in a rectangular, tapered cell of a length, L, and width, W (see Fig. 2.1(a)). The introduction of gap gradient produces a linearly varying height (h) between the two plates of the cell. We consider a lubrication flow confined in the thin gap, whose height varies linearly in x direction as

$h(x) = h_0 + \alpha x$. h_0 denotes the gap thickness at the two fluids' interface, located at $x = 0$.

In the theoretical derivation, we use the effective Darcy's law replacing the constant viscosity, μ, by the effective shear-dependent viscosity, μ_{eff}. This approach has been used in modeling the problems of non-Newtonian fluid-fluid displacement in a flat Hele-Shaw cell [30, 49, 54], but here we extend the approach to a tapered geometry. Neglecting the elastic properties of the two yield-stress fluids [70], the governing equations are 2D-depth-average Darcy's law and the depth-average continuity equation, given below:

$$\mathbf{U}_j = -\frac{h^2}{12\mu_{\text{eff}j}}\vec{\nabla}P_j \ , \tag{2.2}$$

$$\nabla \cdot (h\mathbf{U}_j) = 0. \tag{2.3}$$

$\mathbf{U}_j(x,y) = (u_{xj}, u_{yj})$ and $P_j(x,y)$ are the depth-average velocity and pressure fields of the fluid indexed j, respectively. j represents the two complex fluids during the fluid-fluid displacement process; $j = 1$ (2) denotes the pushing (displaced) complex fluid.

The complex fluid's viscosity ($\mu_{\text{eff}j}$) is modeled using the Herschel-Bulkley law [61] for yield-stress fluids, with the local shear rate $\dot{\gamma} = \frac{u_{xj}}{h}$, and expressed as:

$$\mu_{\text{eff}j} = \frac{\tau_{cj}}{\dot{\gamma}} + \kappa_j \dot{\gamma}^{n_j - 1}, \tag{2.4}$$

where τ_{cj}, κ_j, and n_j correspond to the yield stress, the consistensy index, and the power-law index of the complex fluid j, respectively.

The Bingham number is defined as the ratio of the yield to viscous stress: $Bn_j = \frac{\tau_{cj}}{\kappa_j \left(\frac{u_{xj}}{h}\right)^{n_j}}$, we hence can express $\frac{\tau_{cj}}{\frac{h}{12}\frac{\partial P_j}{\partial x}} = -\frac{1}{1+\frac{1}{Bn_j}}$. Assuming small ratio of gap change, i.e, $\frac{\alpha x}{h_0} << 1$, we can linearize the expression of the gap thickness as $h = h_0\left(1 + \frac{\alpha x}{h_0}\right)$ and neglect the terms of $O\left(\alpha^2\right)$. With Eqs. (2.2)–(2.4), the depth-average continuity Eq. (2.3) can be expressed using pressure field (P_j) and simplified into:

$$\begin{aligned} &\frac{\partial^2 P_j}{\partial x^2} + \frac{(2n_j + 1)\,\alpha}{h_0}\frac{\partial P_j}{\partial x} + \frac{24 n_j \alpha \tau_{cj}}{{h_0}^2} + \frac{\partial^2 P_j}{\partial y^2}\left(1 - \frac{1}{1 + \frac{1}{Bn_j}}\right) n_j \\ &+ \frac{\partial P_j}{\partial y}\left[(1 - n_j)\frac{\frac{\partial^2 P_j}{\partial y \partial x}}{\frac{\partial P_j}{\partial x}} - n_j \frac{\tau_{cj}\frac{\partial^2 P_j}{\partial y \partial x}}{\frac{h}{12}\left(\frac{\partial P_j}{\partial x}\right)^2}\right] = 0. \end{aligned} \tag{2.5}$$

If $n_j = 1$ and $\tau_{cj} = 0$, we find the following equation: $\frac{\partial^2 P_j}{\partial x^2} + \frac{3\alpha}{h}\frac{\partial P_j}{\partial x} + \frac{\partial^2 P_j}{\partial y^2} = 0$, recovering to the one found by Al-Housseiny and Stone for the case of Newtonian fluids [78].

In our linear stability analysis, the pressure is expressed as the addition of base state and perturbation:

$$P_j(x, y, t) = f_j(x) + g_{kj}(x)\epsilon(y, t), \tag{2.6}$$

where $f_j(x)$ corresponds to the base-state, pressure field when the interface is stable and does not depend on y. The term $g_{kj}(x)\epsilon$ term represents the perturbation that propagates along the interface, with the perturbation $\epsilon(y, t) = \epsilon_0 \exp\left(iky + \sigma t\right)$ depending on the wavenumber (k) and the growth rate (σ) of the perturbation.

When the interface is stable, i.e, $\epsilon = 0$ the base-state pressure obeys the following equation:

$$f_j''(x) + \frac{\left(2n_j + 1\right)\alpha}{h_0} f_j'(x) + \frac{24 n_j \alpha \tau_{cj}}{h_0^2} = 0. \tag{2.7}$$

When the interface is unstable, focusing at the moment when the perturbation starts to propagate, implying a small perturbation $(\epsilon << 1)$, $g_{kj}'(x)\epsilon << f_j'(x)$ and the higher-order terms of $O\left(\epsilon^2\right)$ can be neglected. We then obtain the following ODE for solving the perturbed states by substituting Eq. (2.6) in Eq. (2.5):

$$g_{kj}''(x) + \frac{\left(2n_j + 1\right)\alpha}{h_0} g_{kj}'(x) - n_j k^2 g_{kj}(x)\left(1 - \frac{1}{1 + \frac{1}{Bn_j}}\right) = 0. \tag{2.8}$$

At the interface, for $x = 0$, from the Darcy's law and with the fact that $g_{kj}'(x)\epsilon << f_j'(x)$, the solution of the base-state pressure, f_j, in Eq. (2.7) is:

$$f_j(x) = F_j \exp\left(\frac{-\left(2n_j + 1\right)\alpha}{h_0} x\right) - \frac{24 n_j \tau_{cj}}{(2n_j + 1)h_0} x. \tag{2.9}$$

$$F_j = \frac{12}{\left(2n_j + 1\right)\alpha}\left[\tau_{cj} + \kappa_j \left(\frac{U_0}{h_0}\right)^{n_j}\right] - \frac{24 n_j \tau_{cj}}{\left(2n_j + 1\right)^2 \alpha},$$

where U_0 is the velocity of the interface.

To solve the perturbation Eq. (2.8) analytically, we assume $\frac{1}{1+\frac{1}{Bn_j}} << 1$. This assumption is equivalent to suppose $Bn_j << 1$, when the yield stress is negligible compared to the viscous stress, i.e., the fluid is totally yielded. Furthermore, we assume that the characteristic length scale over which the depths varies (i.e., $|\frac{h_0}{\alpha}|$) is much larger than the characteristic length scale of the perturbation scaling as $\frac{1}{k}$, we have $|\frac{kh_0}{\alpha}| >> 1$. We obtain a simplified, general solution for a small $Bn_j << 1$ as:

$$g_{kj}(x) = B_{kj} \exp\left(r_{kj+}x\right) + C_{kj} \exp\left(r_{kj-}x\right),$$
$$r_{kj+} = -\sqrt{n_j}k, \quad r_{kj-} = \sqrt{n_j}k. \tag{2.10}$$

Moreover, physically, it is impossible for the perturbation to grows in space from its origin. This implies the following constraints: $g_{k1}|_{x\to-\infty} = 0$ and $g_{k2}|_{x\to+\infty} = 0$, for a fluid indexed 1 pushing a fluid indexed 2.

As a consequence, the solution can be written as:

$$g_{kj} = B_{kj} \exp\left(m_{kj}x\right),$$
$$m_{kj+} = (-1)^{j+1}\sqrt{n_j}k, \tag{2.11}$$

By linearizing the above exponential terms in Eq. (2.9)-(2.11), we can evaluate the pressure at the interface, for $x = \epsilon$:

$$P_j|_{x=\epsilon} = F_j - \frac{(2n_j+1)\,\alpha}{h_0}F_j\epsilon - \frac{24n_j\tau_{cj}}{(2n_j+1)\,h_0}\epsilon + B_{kj}\epsilon + O\left(\epsilon^2\right). \tag{2.12}$$

To determine the coefficient B_{kj}, we use the velocity continuity condition at the interface for $x = \epsilon$:

$$U_0 + \frac{\partial\epsilon}{\partial t} = u_{xj}|_{x=\epsilon} + \frac{\partial\epsilon}{\partial y}u_{yj}.$$

Focusing on the vicinity of the perturbation, we assume that the perturbation is relatively small, i.e., $\epsilon << 1$, allowing us to linearize the exponential terms of the pressure's derivatives. By neglecting the higher-order terms of $O\left(\epsilon^2\right)$, assuming $U_0 >> \sigma\epsilon$ and $\frac{\alpha\epsilon}{h_0} << 1$, we find the final expression of B_{kj} as:

$$B_{kj} = -\frac{12\kappa_j n_j {U_0}^{n_j}}{m_{kj}{h_0}^{n_j+1}}\left(\frac{\sigma}{U_0} + \frac{\alpha}{h_0}\right). \tag{2.13}$$

For simple Newtonian fluids with $n_j = 1$ and $\kappa_j = \mu_j$, we find the same expression for $B_{kj} = -\frac{12\mu_j U_0}{m_{kj} {h_0}^2}\left(\frac{\sigma}{U_0} + \frac{\alpha}{h_0}\right)$ as previously found by Al-Housseiny and Stone [78].

The Capillary pressure jump at the interface is described by the Young-Laplace equation, which accounts for both the lateral curvature, Ψ, and the curvature, $1/h$, due to the depth of the Hele-Shaw cell. Here, we neglect the viscous stresses. At the interface, $x = \epsilon(y,t)$, for a fluid indexed 1 pushing a fluid indexed 2, the pressure difference across the interface hence is expressed as:

$$P_1 - P_2 = \frac{2\gamma\cos\theta_c}{h_0 + \alpha\epsilon} + \gamma\Psi, \tag{2.14}$$

$$\Psi = \frac{\frac{\partial^2\epsilon}{\partial y^2}}{\left(1 + \left(\frac{\partial\epsilon}{\partial y}\right)^2\right)^{\frac{3}{2}}}, \tag{2.15}$$

where θ_c is the contact angle of the wetting fluid to the side wall, and γ corresponds to the interfacial tension between the two fluids.

With the assumptions $\epsilon << 1$ and $\frac{\alpha\epsilon}{h_0} << 1$ and by neglecting the terms $O\left(\alpha^2\right)$, the second term can be simplified to:

$$\gamma\Psi = -\gamma\frac{(ik)^2\epsilon}{\left(1 + (ik)^2\epsilon^2\right)^{3/2}}.$$

Since $\epsilon^2 (ik)^2 << 1$, $\gamma\Psi = \gamma k^2\epsilon + O\left(\epsilon^2\right)$. Finally, the pressure jump at the interface, for $x = \epsilon(y,t)$ can be expressed as

$$P_1 - P_2 = \frac{2\gamma\cos\theta_c}{h_0} + \gamma\epsilon\left(k^2 - \frac{2\alpha\cos\theta_c}{{h_0}^2}\right) + O\left(\epsilon^2\right). \tag{2.16}$$

The term $\frac{2\gamma\cos\theta_c}{h_0}$ corresponds to the base state, that is the pressure difference at the interface between the two fluids when the interface is stable. The second term is the additional Laplace pressure due to the perturbation at the interface.

By substituting the expression of the linearized pressure Eq. (2.12), along with Eqs. (2.9) and (2.13), into the pressure jump Eq. (2.16) and removing all the base state components, the Laplace pressure Eq. transforms into the following dimensionless dispersion-relation with the dimensionless growth rate of the perturbation defined as $\overline{\sigma} = \frac{\sigma h_0}{U_0}$, and the dimensionless wavenumber of the perturbation, $\overline{k} = h_0 k$:

$$\frac{12\overline{\sigma} h_0 \left(\kappa_1 \sqrt{n_1} \left(\frac{U_0}{h_0} \right)^{n_1} + \kappa_2 \sqrt{n_2} \left(\frac{U_0}{h_0} \right)^{n_2} \right)}{\gamma} = - \frac{12 \alpha h_0}{\gamma} \left(\kappa_1 \sqrt{n_1} \left(\frac{U_0}{h_0} \right)^{n_1} + \kappa_2 \sqrt{n_2} \left(\frac{U_0}{h_0} \right)^{n_2} \right) + \overline{k} \left(2\alpha \cos\theta_c + \frac{12 U_0}{\gamma} \left(\mu_2|_{x=0} - \mu_1|_{x=0} \right) \right) - \overline{k}^3 \tag{2.17}$$

To find the wavenumber at the maximum growth, we take the derivative of Eq. (2.17) w.r.t. $\overline{k}$ and find:

$$\frac{\partial \overline{\sigma}}{\partial \overline{k}} = 2\alpha \cos\theta_c + \frac{12 U_0}{\gamma} \left(\mu_2|_{x=0} - \mu_1|_{x=0} \right) - 3\overline{k}^2.$$

As a consequence, by setting $\frac{\partial \overline{\sigma}}{\partial \overline{k}} = 0$, we find the wavenumber of maximum growth ($\bar{k}_{max}$) equal to:

$$\bar{k}_{max} = \left(\frac{2\alpha \cos\theta_c + \frac{12 U_0}{\gamma} \left(\mu_2|_{x=0} - \mu_1|_{x=0} \right)}{3} \right)^{\frac{1}{2}}. \tag{2.18}$$

The resultant wavelength of maximum growth, $\lambda_{max} = \frac{2\pi h_0}{\bar{k}_{max}}$, is:

$$\lambda_{max} = 2\pi h_0 \left(\frac{3}{2\alpha \cos\theta_c + \frac{12 U_0}{\gamma} \left(\mu_2|_{x=0} - \mu_1|_{x=0} \right)} \right)^{\frac{1}{2}}.$$

The viscous fingering instability of complex fluids will be apparent when $\lambda_{max} < W$ (where W is the width of the Hele-Shaw cell), leading to the following criterion for a visible fingering pattern:

$$-3 \left(\frac{2\pi h_0}{W} \right)^2 + 2\alpha \cos\theta_c + \frac{12 U_0}{\gamma} \left(\mu_2|_{x=0} - \mu_1|_{x=0} \right) > 0. \tag{2.19}$$

We conveniently define a dimensionless term (C^*) using the above stability criterion:

$$C^* = -3 \left(\frac{2\pi h_0}{W} \right)^2 + 2\alpha \cos\theta_c + \frac{12 U_0}{\gamma} \left(\mu_2|_{x=0} - \mu_1|_{x=0} \right). \tag{2.20}$$

so that unstable displacement would occur when $C^* > 0$, whereas stable when $C^* < 0$ theoretically.

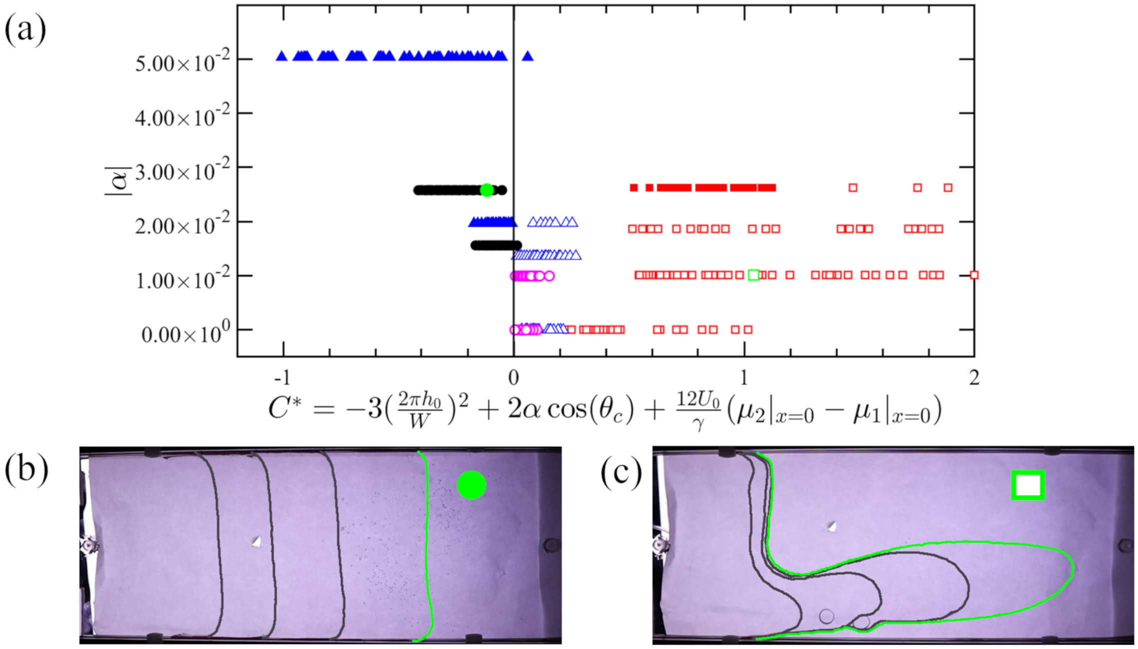

Figure 2.3. **Comparison between experimental and theoretical results:** (a) Dimensionless term C^* [Eq. (2.20)] for different experiments performed with different gap gradient (α). The values of U_0 and h_0 are taken from the experiments. The stable experiments with solution (S1), (S2) and (S3) are represented by (■, ▲ and ●), respectively. The unstable interfaces for the three complex solutions by □, △ and ○. (b) and (c) show the overlay of experimental snapshots with one stable and one unstable displacement, respectively. The interfaces highlighted in green correspond to the two symbols used in (a). The time steps are δt = 150 s and δt = 4 s in (b) and (c), respectively.

Alternatively, from the dispersion-relation Eq. (2.17), the interface would always be stable for a negative growth rate of the perturbation ($\overline{\sigma} < 0$) when the following stability criterion is fulfilled:

$$\left[-\frac{12\alpha h_0}{\gamma}\left(\kappa_1\sqrt{n_1}\left(\frac{U_0}{h_0}\right)^{n_1} + \kappa_2\sqrt{n_2}\left(\frac{U_0}{h_0}\right)^{n_2}\right)\right.$$
$$\left. + \overline{k}\left(2\alpha\cos\theta_c + \frac{12U_0}{\gamma}\left(\mu_2|_{x=0} - \mu_1|_{x=0}\right)\right) - \overline{k}^3\right]\frac{\gamma}{12h_0\left(\kappa_1\sqrt{n_1}\left(\frac{U_0}{h_0}\right)^{n_1} + \kappa_2\sqrt{n_2}\left(\frac{U_0}{h_0}\right)^{n_2}\right)} < 0. \tag{2.21}$$

2.5 Comparing experimental vs. Theoretical results

In the linear stability analysis, we use the effective Darcy's law and obtain a criterion concerning the wavelength for a visible viscous fingering, i.e., Eq. (2.19). This criterion depends on the local rheological properties of the fluids $(\kappa_j, n_j, \tau_{cj})$, the gap gradient (α) as well as the velocity (U_0) and gap thickness (h_0) at the interface, in addition to various factors such as the wetting angle (θ_c) and the interfacial tension between the pushing and the driven fluid. We further compare our experimental results with this theoretical criterion Eq. (2.19) for a visible complex viscous finger. Using the experimental values of U_0, h_0, and α, we plot the values of our dimensionless term [Eq. (2.20)] in Fig. 2.3(a). Here, we consider a stable displacement when the fluid-fluid interface is uniform and stable throughout the entire experiment.

Shown in Fig. 2.3(a), in accordance with our theory, a clear separation between stable (■, ▲ and ●) and unstable displacements (□, △ and ○) for a criterion around 0. However, for the more viscous fluid (S1), we observe stable experiments that are off the expected chart. This deviation can be explained by the few assumptions we made. The impact of the gravity, the elastic properties have been ignored. We are using the constant static contact angle in our theoretical derivation. Moreover, whenever the gap gradient α is getting bigger, the assumptions of small ratio of gap change $(\frac{\alpha x}{h_0} << 1)$ as well as the characteristic length scale over which the depths varies being much larger than the characteristic length scale of the perturbation scaling $(\frac{kh_0}{\alpha} >> 1)$ are starting to be unjustified. Finally, we neglected the yield stress with respect to the viscous stress. We can expect the differences to be explained by these assumptions.

2.6 Concluding remarks

We demonstrate experimentally and theoretically a useful and powerful method of inhibiting the viscous fingering (or Saffman-Taylor) instability for complex yield-stress fluids by using a converging tapered rectangular cell. We perform a linear stability analysis using an effective

Darcy's law and derive a stability criterion concerning the perturbation wavelength. For the Newtonian fluids, the stability of the interface is determined by four parameters, namely the gap gradient, the contact angle to the side wall, the viscosity contrast, and the Capillary number (α, θ_c, λ and Ca, respectively). In contrast, for complex yield-stress fluids, in addition to the above four parameters, the width of the cell (W), the interface's velocity and gap thickness (U_0 and h_0), as well as the Herschel-Bulkley coefficients (τ_c, κ and n) determining the local fluid viscosity influence the viscous fingering stability through Eq. (2.19).

For various gap gradient, α, ranging from -5.03×10^{-2} to 0, we observe a transition from stable and unstable interfaces when the dimensionless term C^* in Eq. (2.20) is approximately equal to 0 in Fig. 2.3(a). However, for the more viscous fluid (S1), we observe a discrepancy when the gap gradient (α) is greater. This drifting of values might be due to some assumptions we made in the derivation. The impact of the gravity, the elastic properties of the fluids and the Bingham number (ratio of yield stress over the viscous stress) have all been neglected. Moreover, we made assumptions by using of the static contact angle and a small gap gradient (α). All these assumptions are important for the final criterion and are surely playing a role in our discrepancy. In addition to our theoretical criterion, in a more simplistic way, we were able to plot a stability diagram (α v.s Q) and observe a transition, above a critical injection flow rate, between a complete sweep experience and the experiences where unstable interfaces appears for our three complex fluids. A more complex derivation without neglecting the impact of the yield stress should be investigated to provide more accurate prediction of the viscous fingering stability criterion for the complex fluids.

Chapter 3

Controlling Viscous Fingering of Complex Yield-Stress Solutions in a Tapered Radial Hele-Shaw Cell [1]

3.1 Introduction

The displacement of a more viscous fluid by another less viscous one in a porous medium is a common theme occurring in a myriad of natural and industrial processes, ranging from small-scale applications such as chromatographic separation [11], coating flows [8, 12, 13], printing devices [7], oil well cementing [94], to large-scale technologies of groundwater [15, 16], enhanced oil recovery (EOR) [19, 22], as well as carbon capture, utilization and storage [24, 25, 26]. The unfavorable mobility or viscosity contrast, λ, triggers a fingering pattern during fluid-fluid displacement, hindering a full swipe and impeding oil recovery in EOR. This classical fingering (so-called Saffman-Taylor) instability [40, 41, 43, 44, 74] has been extensively studied for decades, particularly for Newtonian fluids using a paradigm of Hele-Shaw cell consisting of two parallel plates with a constant and narrow gap thickness. The influences of inertia [29], surface tension [31], and complex geometry such as rotating Hele-

---

[1] The material presented in this chapter is based on a manuscript in preparation by Alban Pouplard and Peichun Amy Tsai, "Controlling Viscous Fingering of Complex Fluids," in preparation, 2021.

Shaw cell [38] on the viscous fingering instability have been studied. More specifically, the inertia has a tendency to increase the width of the fingers above a critical Weber number [29]; the effect of a curvature-dependent surface tension can theoretically lead to the stabilization (destabilization) of conventionally unstable (stable) situations [31]. In recent two decades, studies of viscous fingering have been extended to complex fluids, usually leading to wider fingers compared to the Newtonian counterparts [46, 49, 54]. Intriguing side-branching patterns, with multiple small fingers forming on the side of the major ones, are often observed with complex, yield-stress fluids [50, 67, 68, 70].

The control of the fingering instability is significant to enhance the efficiency of various industrial applications. For simple Newtonian fluids, several strategies have been recently developed to suppress the fingering instability, e.g., using time-dependent injection flow rate [76, 77, 79], an elastic confinement [90, 91, 92], a gap-gradient cell [78, 85, 86], and an external electric field [97]. Nevertheless, such control of the primary viscous fingering instability has not been reported for complex fluids. In this chapter, we demonstrate the feasibility of inhibit a viscous fingering instability of complex, yield stress fluids using a radially-tapered Hele-Shaw cell. First, we systematically carry out experiments of a gas pushing a yield-stress, shear-thinning fluid to investigate the effects of flow rates and gap gradients on the viscous fingering patterns. Subsequently, we analytically derive a linear stability criterion for two immiscible yield-stress fluids pushing one another in a radially-converging cell. In comparison, the analytical prediction is in fair agreement with the experimental results, highlighting the local rheological parameters plays a crucial role in altering the viscous fingering stability, in addition to the viscosity contrast (λ) and Capillary number (Ca) for the simple Newtonian fluid cases.

3.2 Experimental

To examine complex fluids' viscous fingering, we use two different aqueous solutions of PolyAcrylic Acid (PAA, SigmaAldrich, molecular weight: $M_w \approx 1,250,000$) as a wetting yield-stress fluid. PAA is a water-soluble polyelectrolyte that has wide applications as a

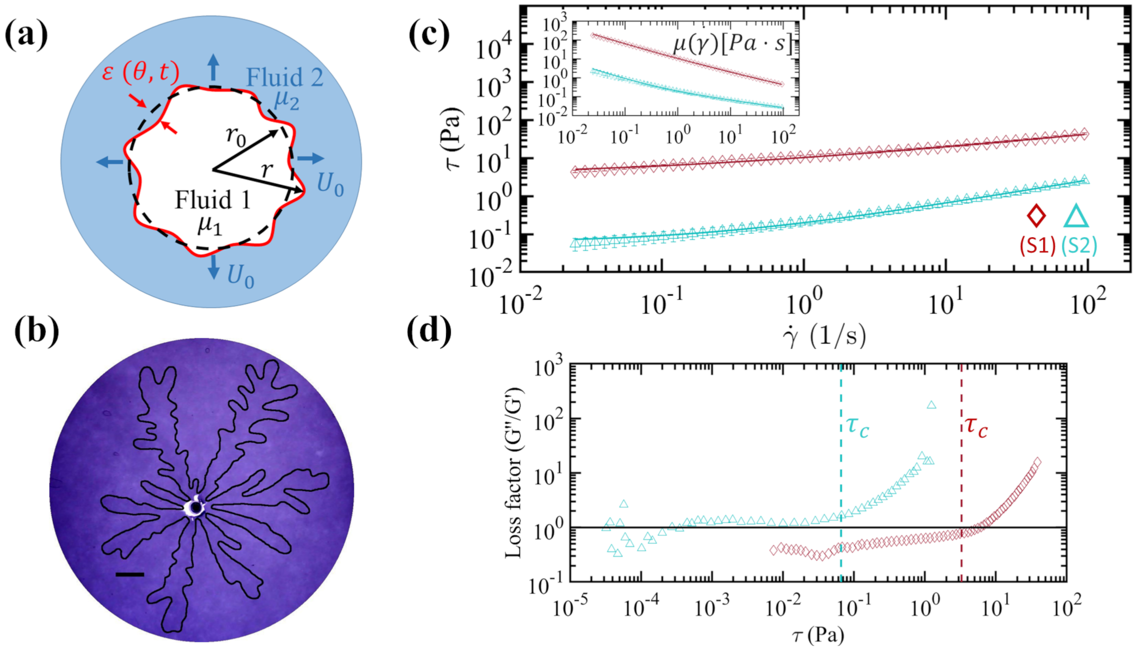

Figure 3.1. (a) Top-view schematic of the fluid-fluid displacement experiment where one less viscous complex fluid 1 of varying viscosity (μ_1) with shear rate ($\dot{\gamma}$) is pushing another immiscible one, denoted as complex fluid 2 with changing viscosity μ_2. (b) Representative experimental snapshot of complex viscous fingering produced with a complex yield-stress (PAA) solution (S1) displaced by a gas injected with a flow rate $Q = 0.2$ slpm in a flat Hele-Shaw cell, under the viscosity contrast $\lambda = \mu_2/\mu_1 = 5.58 \times 10^4$ and at the interface velocity $U_0 = 14.3$ mm/s. The scale bar corresponds to 20 mm. (c) Flow curves of shear stress, τ, and viscosity, μ, depending on the shear rate, $\dot{\gamma}$, for the two complex yield-stress solutions used: (S1, ◇) and (S2, △) . The lines in (c) correspond to the best fits of the data to the Herschel-Bulkley model described by Eq. (3.1). (d) The data of loss factor, the ratio of the loss modulus (G'') to the storage modulus (G'), varying with the shear stress, τ, obtained during oscillation amplitude sweep test at constant frequency ($\hat{w} = 1$ rad/s). The vertical dashed lines represent the yield-stress (τ_c) values of the two fluids.

fluid thickener as well as a dispersing, suspending, and emulsifying agent in pharmaceuticals and cosmetics [95, 96]. Experimentally, we first fill in one complex PAA solution in a radial cell and subsequently inject a gas (Nitrogen, viscosity $\mu_1 = 1.76 \times 10^{-5}$ Pa.s at 20°C) as a pushing fluid (see Fig. 3.1(a)). The gas is injected at a constant flow rate, Q, ranging from 0.02 to 2 slpm (standard liter per minute) by a flow controller (Alicat) with an accuracy of 1 ml/min.

The two aqueous solutions of PAA are prepared to produce different viscosity contrasts.

Both solutions have the same polymer concentration, by slowly adding the polymer powder in water and subsequently stirring the mixture at high speed for 1 hr. The mixture generates an acid solution that can be neutralized using a basic solution. The two PAA solutions are prepared with (S1) and without NaOH (S2), stirred for another 10 hours at medium speed. Finally, after the agitation, the solution is rest for a day before performing rheological measurements.

Fig. 3.1(c) shows the rheological measurements (AntonPaar MCR302) of the two complex solutions. Neglecting the elastic properties, we use the common rheological model of Herschel–Bulkley (HB) to fit the shear stress (τ) varying with the shear rate ($\dot{\gamma}$) [61]:

$$\tau = \tau_c + \kappa \dot{\gamma}^n, \tag{3.1}$$

with τ_c, κ and n corresponding to the yield stress, the consistensy index, and the power-law index, respectively. The complex fluids' viscosity data ($\mu = \frac{\tau}{\dot{\gamma}}$) varying with $\dot{\gamma}$ is well described by the corresponding HB model of $\mu = \frac{\tau_c}{\dot{\gamma}} + \kappa \dot{\gamma}^{n-1}$. Table 3.1 summarizes the best nonlinear fit results of the rheological measurements of $\tau = f(\dot{\gamma})$ for the experimental range of $\dot{\gamma}$ between 0.025 and 86 s^{-1}, and the corresponding fits are plotted as lines in Fig. 3.1(c). Overall, both complex solutions are shear-thinning, with decreasing viscosity with increasing shear rate $\dot{\gamma}$, i.e., $n < 1$. However, the neutralized PAA solution with NaOH (S1) is more viscous, has a greater yield-stress (τ_c) but a smaller power-law index (n).

Yield-stress solution	PAA (wt %)	NaOH (wt %)	τ_c (Pa)	κ (Pa.s^n)	n
(S1)	0.10	0.034	3.2857	7.1179	0.3721
(S2)	0.10	0	0.0596	0.1413	0.6333

Table 3.1

Rheological parameters for the two complex, yield-stress fluids with the HB model [Eq. (3.1)].

We further perform oscillation amplitude sweep tests at constant frequency ($\hat{\omega} = 1$ rad/s) to validate negligible elasticity of the complex fluids. Shown in Fig. 3.1(d) are the results of the loss factor–the ratio of the loss modulus (G'') to the storage modulus (G'). The former (G'') represents the viscous properties of the complex fluids, while the latter (G')

fluid elasticity with respect to the shear stress, τ. The fluid's viscous behavior prevails when the loss factor (G''/G') is greater than the unity, whereas elastic for G''/G' less than 1. The vertical dashed lines represents the yield-stress values for the both fluids (S1) and (S2). We only focus on the regime when fluids are flowing, i.e, $\tau > \tau_c$, where the loss factor is more or less greater than 1, meaning that the viscous prevails and we could neglect the elastic effects of the fluids.

In our experiments, a radial Hele-Shaw cell with a converging gap is used to control the interfacial viscous fingering instability (see Fig. 3.2(a)). The bottom plate is made of glass, while the upper of Acrylic cast. The upper plates are tapered with a negative gradient, $\alpha = dh/dr < 0$, the ratio of the height (h) to the radial length (r) of the tapered cell. Spacers of constant thickness $h_f = 0.5$ mm are placed at the edges of the upper cell to create a separation between the two plates' edges. The gap thickness inside the cell evolves linearly as $h = h_c + \alpha r$, with h_c the gap thickness at the central injection point. The experimental snapshots are captured, from below, with a camera (Canon EOS 70D) at 30 fps (frames per second). To enhanced contract at the interface, a light is placed and used above the cell. We use ImageJ and Matlab to analyze the experimental snapshots and track the interface position. The interface velocity, U_0 is calculated by deriving the interface radius position over a short period of time (t). The values of the Reynolds number for our experiments are ranging from 5.90×10^{-6} to 1.33. The permeability of the cell ranges from 2.08×10^{-8} to 5.46×10^{-6} m^2.

3.3 Results and Discussions

We carry out over 700 experiments using both flat Hele-Shaw and tapered cells. With flat Hele-Shaw cells, as illustrated by Fig. 3.2(b), we can observe classical primary fingers similar to those for Newtonian fluids. However, more complex patterns in the form of tiny fingers as secondary instability at the side of the major fingers are found (See Fig. 3.1(b)). Such side-fingering patterns are consistent with previous Non-Newtonian fluid data and are referred to as a side-branching regime [65] or the elasto-inertial regime [67, 68]. These side-branched

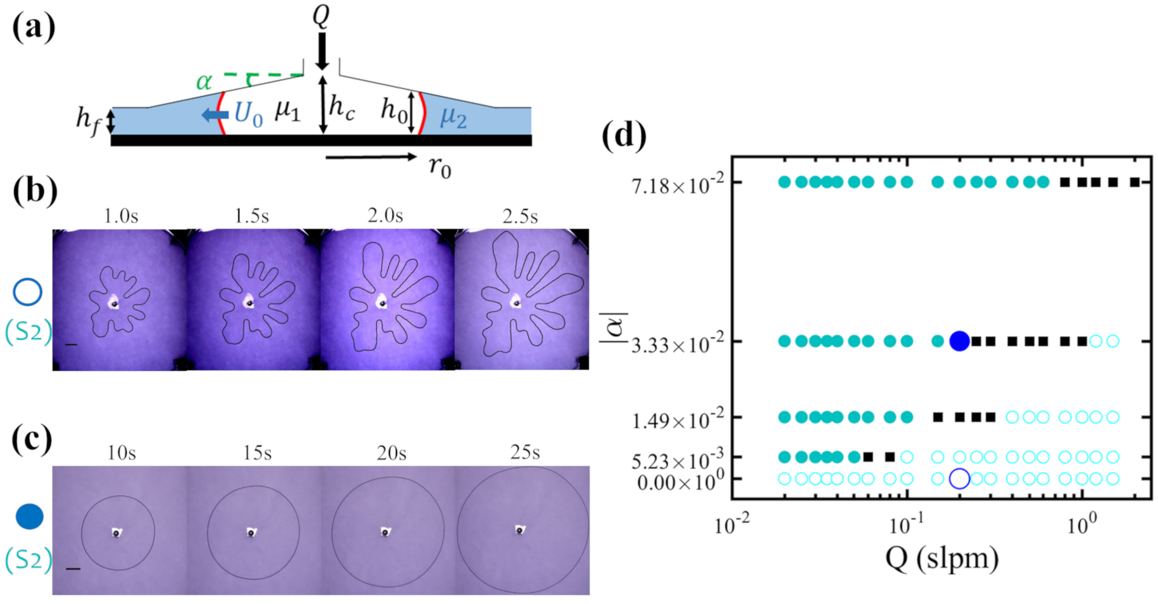

Figure 3.2. **Control of complex viscous fingering** using a radially-tapered cell, with a linearly varying gap thickness ($h = h_c + \alpha r$), schematically shown in (a), the side-view of the experiment. (b) Experimental snapshots of a branched viscous fingering pattern observed when a gas is pushing the complex solution (S2) in a flat Hele-Shaw cell with $h_c = 0.5$ mm and $Q = 0.2$ slpm. (c) By contrast, snapshot of a stable interface obtained when the gas is pushing (S2) in a tapered Hele-Shaw cell of the gap gradient $\alpha = -3.33 \times 10^{-2}$, with $h_c = 5.16$ mm and $Q = 0.2$ slpm. The scale bars in (b) and (c) correspond to a distance of 20 mm.(d) Experimental results of stability diagram, with uniform stable (●) vs. fingering/wavy unstable interfaces (○) under various values of flow rate, Q, and the tapered gap gradient, α. Black squares (■) represent a transitional state where the interface starts to develop a wavy profile.

fingers are being obtained only at a high flow rate ($Q \geq 1.5$ slpm) for the fluid (S2) but observed for every injection flow rate explored (0.02 – 1.5 slpm) for the more-viscous fluid (S1). In the rest of the paper, we will not differentiate the classical finger pattern and the side-branching pattern; both will be considered as unstable displacement.

When using converging cells, we stopped observing side-branched fingers but smooth classical viscous fingers under the flow rate ranging from 0.02 slpm to 1.5 slpm. This observation is consistent with a recent experimental study [89] revealing mitigation of side-branching (but not inhibition of the primary VF) for a complex yield-stress fluid in a rectangular tapered cell. However, with suitable rheological and flow parameters, remarkably we can control or inhibit the primary fingering instability and observe complete stable and flat interfaces between the pushing Newtonian gas and the yield-stress fluid, as illustrated by Fig. 3.2(c). During our experiments, we often observe a stable interface at the earlier times of the injection as it takes time to develop a flow instability. However, in most cases, the Saffman-Taylor instability propagates after a steady-state is reached. For our analysis, a displacement will be considered stable if the interface is uniform and stable throughout the entirety of the experiment.

The first crucial observation is that the fluid-fluid interface is stable at lower injection flow rate when keeping α and h_c constant. Revealed in Fig. 3.2(d) is a phase diagram of three flow patterns observed under different α and Q. We differentiate the three types of patterns observed during the experiments with the complex fluid (S2), namely uniform stable interfaces and displacements (●), fingering/wavy unstable interfaces (○), and transitional state (■) where the interface starts to develop a wavy profile.

The addition of a converging gap gradient helps the interface to stabilize and the transition between stable and unstable interfaces happens at higher flow rate. Such figures can be observed in previous papers with Newtonian fluids [86]. Here, we are only able to plot the stability diagram for the fluid (S2) because a complete sweep has never been observed with the more viscous complex fluid (S1) of a viscosity contrast $\lambda = \mu_2/\mu_1$ ranging from 2.68×10^4 to 1.16×10^7, with $\mu_1 = 1.76 \times 10^{-5}$ Pa.s as the nitrogen viscosity. The viscosity contrast for the fluid (S2) ranges from 1.61×10^3 to 1.67×10^5 in our experiments. These contrast results between the two complex solutions (S1 and S2) highlight not only the complicity of controlling complex viscous fingering but also the importance of rheological parameters through κ, n, and the local shear rate, $\dot{\gamma}$.

3.4 Theoretical Background

To gain physical insights into crucial parameters controlling the primary complex viscous fingering instability, we develop a linear stability analysis generalized to both yield-stress, power-law complex fluids (Fluid 1 pushing Fluid 2) in a radial, tapered Hele-Shaw cell (see Fig. 3.2(a)). The introduction of a constant gap gradient (α) produces a linearly-varying height $h(r) = h_c + \alpha r$ between the two plates of the cell. Considering the fluids' interface at $r = r_0$, the height h can be expressed as $h(r) = h_0 + \alpha\left(r - r_0\right)$, with h_0 the gap thickness at the interface.

In the theoretical derivation based on the lubrication theory, we use the effective Darcy's law replacing the constant viscosity, μ, by the effective shear-dependent viscosity, μ_{eff}. This approach has been used in other derivations to model non-Newtonian flow in a homogeneous porous medium or a uniform Hele-Shaw cell [30, 49, 54]. Neglecting the fluids' elastic properties [70], the governing equations are the continuity equation and 2D depth-average Darcy's law:

$$\nabla \cdot \left(h\mathbf{U}_j\right) = 0, \tag{3.2}$$

$$\mathbf{U}_j = -\frac{h^2}{12\mu_{\text{eff}j}}\vec{\nabla}P_j. \tag{3.3}$$

$\mathbf{U}_j(r,\theta) = \left(u_{rj}, u_{\theta j}\right)$ and $P_j(r,\theta)$ are the depth-average velocity and pressure fields of the fluid indexed j, respectively. j represents the two complex fluids during the fluid-fluid displacement process; $j = 1$ (2) denotes the pushing (displaced) complex fluid.

The complex fluid's viscosity ($\mu_{\text{eff}j}$) is modeled using the Herschel-Bulkley law [61] for yield-stress fluids, with the local shear rate $\dot{\gamma} = u_{rj}/h$, and expressed as:

$$\mu_{\text{eff}j} = \frac{\tau_{cj}}{\dot{\gamma}} + \kappa_j \dot{\gamma}^{n_j - 1}, \tag{3.4}$$

where τ_{cj}, κ_j and n_j correspond to the yield stress, the consistensy index, and the power-law index, respectively.

By defining the Bingham number as the ratio of the yield to viscous stress: $Bn_j = \frac{\tau_{cj}}{\kappa_j\left(\frac{u_{rj}}{h}\right)^{n_j}}$, we express $\frac{\tau_{cj}}{\frac{h}{12}\frac{\partial P_j}{\partial r}} = -\frac{1}{1+\frac{1}{Bn_j}}$. Assuming a small ratio of gap change, i.e., $\frac{\alpha(r-r_0)}{h_0} << 1$, we can linearize the expression of the gap thickness as $h = h_0\left(1 + \frac{\alpha(r-r_0)}{h_0}\right)$ and neglect the higher-order terms of $O\left(\alpha^2\right)$. With Eqs. (3.3)–(3.4), the depth-average continuity Eq. (3.2) can be expressed using pressure field (P_j) and simplified into:

$$\frac{\partial^2 P_j}{\partial r^2} + \frac{n_j}{r}\frac{\partial P_j}{\partial r} + \frac{(2n_j+1)\,\alpha}{h_0}\frac{\partial P_j}{\partial r} + \frac{12 n_j \alpha \tau_{cj}}{h_0^2} + \frac{12 n_j \tau_{cj}}{h_0 r} + \frac{12 n_j \tau_{cj} \alpha}{{h_0}^2}\frac{r_0}{r}$$
$$+ \frac{n_j}{r^2}\frac{\partial^2 P_j}{\partial \theta^2}\left(1 - \frac{1}{1+\frac{1}{Bn}}\right) + \frac{1}{r^2}\frac{\partial P_j}{\partial \theta}\left[(1-n_j)\frac{\frac{\partial^2 P_j}{\partial\theta\partial r}}{\frac{\partial P_j}{\partial r}} - n_j \frac{\tau_{cj}\frac{\partial^2 P_j}{\partial\theta\partial r}}{\frac{h}{12}\left(\frac{\partial P_j}{\partial r}\right)^2}\right] = 0. \tag{3.5}$$

By setting $n_j = 1$ and $\tau_{cj} = 0$, the above Eq. recovers to the simple Newtonian fluid case: $\frac{\partial^2 P_j}{\partial r^2} + \frac{1}{r}\frac{\partial P_j}{\partial r} + \frac{3\alpha}{h}\frac{\partial P_j}{\partial r} + \frac{1}{r^2}\frac{\partial^2 P_j}{\partial \theta^2} = 0$, reported by Al-Housseiny and Stone [78].

In the linear stability analysis, the pressure field is expressed as the solutions of the base state and the perturbation, $\epsilon(\theta,t) = \epsilon_0 r_0(t)\exp(ik\theta + \sigma t)$:

$$P_j(r,\theta,t) = f_j(r) + g_{kj}(r)\epsilon(\theta,t). \tag{3.6}$$

Here, $f_j(r)$ corresponds to the base-state pressure when the interface is stable and independent of θ. The term of $g_{kj}(r)\epsilon$ represents the perturbation that propagates along the interface, with wavenumber (k) and the growth rate (σ) of the perturbation.

We focus at the moment when the perturbation starts to propagate, implying small perturbation ($\epsilon << 1$), $g'_{kj}(r)\epsilon << f'_j(r)$, and negligible high-order terms of $O\left(\epsilon^2\right)$. Since we are interested in the solution of P_j in the vicinity of the perturbed interface, we can linearize around the base state such that: $r = r_0(1+\epsilon_0 z)$ with $\epsilon_0 << 1$. Substituting Eq. (3.6) into Eq. (3.5), using $\epsilon_0 << 1$ to linearize terms and neglecting $O\left({\epsilon_0}^2\right)$ but not $O\left({\epsilon_0}^2 k^2\right)$, the solutions of the base and perturbed states can be found with the following Eqns:

$$\frac{\partial^2 f_j(z)}{\partial z^2} + n_j\epsilon_0\frac{\partial f_j(z)}{\partial z} + \frac{(2n_j+1)\,\alpha}{h_0}\epsilon_0 r_0\frac{\partial f_j(z)}{\partial z} = 0. \tag{3.7}$$

$$\frac{\partial^2 g_{kj}(z)}{\partial z^2} + n_j\epsilon_0\frac{\partial g_{kj}(z)}{\partial z} + \frac{(2n_j+1)\,\alpha}{h_0}\epsilon_0 r_0\frac{\partial g_{kj}(z)}{\partial z} - n_j k^2 {\epsilon_0}^2 g_{kj}\left(1 - \frac{1}{1+\frac{1}{Bn_j}}\right) = 0. \tag{3.8}$$

At $r = r_0$, from the Darcy's law and with the fact that $g'_{kj}(r)\epsilon << f'_j(r)$, we solve for the specific solution for the base-state pressure, $f_j(r)$, expressed with $z = \frac{r-r_0}{\epsilon_0 r_0}$:

$$f_j(r) = F_j \exp\left(-\left(n_j + \frac{(2n_j+1)\,\alpha r_0}{h_0}\right)\frac{r-r_0}{r_0}\right),$$

$$F_j = \frac{12\left[\tau_{cj} + \kappa_j\left(\frac{U_0}{h_0}\right)^{n_j}\right]}{h_0}\frac{r_0}{n_j + \frac{(2n_j+1)\alpha r_0}{h_0}}. \tag{3.9}$$

To solve the perturbation Eq. (3.8) analytically, we assume $(1+\frac{1}{Bn_j})^{-1} << 1$, equivalent to small $Bn_j(<< 1)$ situation when the yield stress is negligible compared to the viscous stress. Let's assume that the length scale of the interfacial perturbation (i.e, $|\frac{r_0}{k}|$) is much smaller than the length scale over which the depth varies scaling as $|\frac{h_0}{\alpha}|$. Under this assumption, we have $|\frac{\alpha r_0}{kh_0}| = O(\epsilon)$. We then obtain a simplified solution for a small Bn_j $(<< 1)$ as

$$g_{kj}(z) = B_{kj}\exp\left(r_{kj+}z\right) + C_{kj}\exp\left(r_{kj-}z\right),$$

$$r_{kj+} = -\epsilon_0\sqrt{n_j}k, \quad r_{kj-} = \epsilon_0\sqrt{n_j}k.$$

Moreover, physically, it is impossible for the perturbation to grows in space from its origin. It means that for a fluid indexed 1 pushing a fluid indexed 2, we have the following constraints: $g_{k1}|_{r\to 0} = 0,\ g_{k2}|_{r\to+\infty} = 0,\ g_{k1}|_{z\to-\infty} = 0,\ g_{k2}|_{z\to+\infty} = 0$. As a consequence, the solution can be expressed with $z = \frac{r-r_0}{r_0\epsilon_0}$:

$$g_{kj} = B_{kj}\exp\left(m_{kj}\frac{r-r_0}{r_0}\right), \tag{3.10}$$

$$m_{kj} = (-1)^{j+1}\sqrt{n_j}k. \tag{3.11}$$

By linearizing the exponential terms in Eq. (3.9)-(3.10), we can evaluate the pressure at the interface ($r_{\text{int}} = r_0 + \epsilon$).

$$P_j|_{r=r_0+\epsilon} = \frac{12\left[\tau_{cj} + \kappa_j\left(\frac{U_0}{h_0}\right)^{n_j}\right]}{h_0}\frac{r_0}{n_j + \frac{(2n_j+1)\alpha r_0}{h_0}} - \frac{12\left(\tau_{cj} + \kappa_j\left(\frac{U_0}{h_0}\right)^{n_j}\right)}{h_0}\epsilon + B_{kj}\epsilon + O\left(\epsilon^2\right). \tag{3.12}$$

To determine the coefficient B_{kj}, we use the velocity continuity condition at the interface for $r = r_{\text{int}} = r_0 + \epsilon$, i.e. $\frac{\partial r_{\text{int}}}{\partial t} = u_{rj}|_{r=r_0+\epsilon}$. By linearizing $\frac{\partial P_j}{\partial r}$ at the interface, using the assumptions of $U_0 >> \sigma\epsilon$ and $\frac{\alpha\epsilon}{h_0} << 1$, but neglecting $O\left(\epsilon^2\right)$, we find the expression for B_{kj}:

$$B_{kj} = -\frac{12\kappa_j}{m_{kj}{h_0}^{n_j+1}}\left(n_j\sigma {U_0}^{n_j-1}r_0 + n_j{U_0}^{n_j}\frac{\alpha r_0}{h_0} + n_j\frac{{h_0}^{n_j}\tau_{cj}}{\kappa_j} + 2n_j\frac{{h_0}^{n_j}\tau_{cj}}{\kappa_j}\frac{\alpha r_0}{h_0} + n_j{U_0}^{n_j}\right). \tag{3.13}$$

For simple Newtonian fluids as $n_j = 1$ and $\kappa_j = \mu_j$, we find the same expression for $B_{kj} = -\frac{12\mu_j U_0}{m_{kj}{h_0}^2}\left(\frac{\sigma r_0}{U_0} + \frac{\alpha r_0}{h_0} + 1\right)$ as the solution found previously by Al-Housseiny and Stone [78].

The Capillary pressure jump at the interface is described by the Young-Laplace equation, which accounts for both the lateral curvature (Ψ) and the curvature because of the cell depth $\left(\frac{1}{h}\right)$. However, we will neglect the viscous stresses. At the interface, $r = r_0 + \epsilon(\theta, t)$, for a fluid indexed 1 pushing a fluid indexed 2, the pressure difference across the interface is:

$$P_1 - P_2 = \frac{2\gamma\cos\theta_c}{h_0 + \alpha\epsilon} + \gamma\Psi, \tag{3.14}$$

$$\Psi = \frac{r^2 + 2\left(\frac{\partial r}{\partial\theta}\right)^2 - r\frac{\partial^2 r}{\partial\theta^2}}{\left(r^2 + \left(\frac{\partial r}{\partial\theta}\right)^2\right)^{\frac{3}{2}}}, \tag{3.15}$$

where γ is the interfacial tension, and θ_c corresponds to the contact angle of the wetting fluid to the side wall. Since ${r_0}^2 >> \epsilon^2$, using the linearization around r_0, and neglecting $O\left(\epsilon^2\right)$, the second term in Eq. (3.14) can be simplified to:

$$\gamma\Psi = \gamma\left(\frac{1}{r_0} - \frac{\epsilon}{{r_0}^2} + \frac{k^2\epsilon}{{r_0}^2}\right).$$

Finally, the pressure jump at the interface $r = r_0 + \epsilon(\theta, t)$ can be expressed by:

$$P_1 - P_2 = \frac{2\gamma\cos\theta_c}{h_0} + \frac{\gamma}{r_0} + \gamma\epsilon\left(\frac{k^2 - 1}{{r_0}^2} - \frac{2\alpha\cos\theta_c}{{h_0}^2}\right) + O\left(\epsilon^2\right). \tag{3.16}$$

The terms $\frac{2\gamma\cos\theta_c}{h_0} + \frac{\gamma}{r_0}$ corresponds to the base state, that is the pressure difference at the interface between the two fluids where the interface is stable. The rest are the additional Laplace pressure due to the perturbation at the interface.

We substitute the expression of the linearized pressure Eq. (3.12), along with (3.13), into the pressure jump Eq. (3.16), and remove all the base state components, the Laplace pressure equation transforms into the following dimensionless dispersion-relation with the dimensionless growth rate of the perturbation, $\bar{\sigma} = \frac{\sigma r_0}{U_0}$, and the dimensionless wavenumber of the perturbation, $\bar{k} = k$:

$$\frac{12\bar{\sigma} h_0}{\gamma}\left(\kappa_1\sqrt{n_1}\left(\frac{U_0}{h_0}\right)^{n_1}+\kappa_2\sqrt{n_2}\left(\frac{U_0}{h_0}\right)^{n_2}\right) = -\frac{12U_0}{\gamma}\left(\sqrt{n_1}\mu_1|_{r=r_0}+\sqrt{n_2}\mu_2|_{r=r_0}\right)$$
$$-\frac{12\alpha r_0}{\gamma}\left(2\sqrt{n_1}\tau_{c1}+2\sqrt{n_2}\tau_{c2}+\sqrt{n_1}\kappa_1\left(\frac{U_0}{h_0}\right)^{n_1}+\sqrt{n_2}\kappa_2\left(\frac{U_0}{h_0}\right)^{n_2}\right)$$
$$+\bar{k}\left(\frac{12U_0}{\gamma}\left(\mu_2|_{r=r_0}-\mu_1|_{r=r_0}\right)+2\alpha\cos\theta_c+\frac{{h_0}^2}{{r_0}^2}\right)-\frac{{h_0}^2}{{r_0}^2}\bar{k}^3. \tag{3.17}$$

Consequently, with $\tau_{cj} = 0$, $n_j = 1$, $\kappa_j = \mu_j$ for simple Newtonian fluids, and defining $\lambda = \frac{\mu_1}{\mu_2}$ and $Ca = \frac{12U_0\mu_2}{\gamma}$, the dispersion relation transforms into:

$$\frac{\sigma Ca r_0}{U_0}(\lambda+1) = -Ca(1+\lambda)\left(1+\frac{\alpha r_0}{h_0}\right)+\bar{k}\left(2\alpha\cos\theta_c+\frac{{h_0}^2}{{r_0}^2}+Ca(1-\lambda)\right)-\frac{{h_0}^2}{{r_0}^2}\bar{k}^3,$$

which is the same relation found by Al-Housseiny and Stone for simple Newtonian fluids [78].

To find the wavenumber at the maximum growth, we take the derivative of above Eq. (3.17) w.r.t. $\bar{k}$ by setting $\frac{\partial\bar{\sigma}}{\partial\bar{k}} = 0$, we find the wavenumber of maximum growth ($\bar{k}_{max}$) equal to:

$$\bar{k}_{max} = \left(\frac{\frac{{h_0}^2}{{r_0}^2}+2\alpha\cos\theta_c+\frac{12U_0}{\gamma}\left(\mu_2|_{r=r_0}-\mu_1|_{r=r_0}\right)}{3\frac{{h_0}^2}{{r_0}^2}}\right)^{\frac{1}{2}}. \tag{3.18}$$

The resultant wavelength of maximum growth, $\lambda_{max} = 2\pi r/\bar{k}_{max}$, hence is:

$$\lambda_{max} = 2\pi r\left(\frac{3\frac{{h_0}^2}{{r_0}^2}}{\frac{{h_0}^2}{{r_0}^2}+2\alpha\cos\theta_c+\frac{12U_0}{\gamma}\left(\mu_2|_{r=r_0}-\mu_1|_{r=r_0}\right)}\right)^{\frac{1}{2}}.$$

The viscous fingering instability of complex fluids would be apparent when $\lambda_{max} < 2\pi r$, leading to the following criterion for a visible fingering pattern:

$$-2\frac{{h_0}^2}{{r_0}^2}+2\alpha\cos\theta_c+\frac{12U_0}{\gamma}\left(\mu_2|_{r=r_0}-\mu_1|_{r=r_0}\right) > 0. \tag{3.19}$$

Alternatively, from the dispersion-relation Eq. (3.17), the interface would always be stable for a negative growth rate of the perturbation ($\bar{\sigma} < 0$) when the following stability criterion is fulfilled:

$$\Bigg[-\frac{12U_0}{\gamma}\left(\sqrt{n_1}\mu_1|_{r=r_0}+\sqrt{n_2}\mu_2|_{r=r_0}\right)-\frac{12\alpha r_0}{\gamma}\left(2\sqrt{n_1}\tau_{c1}+2\sqrt{n_2}\tau_{c2}+\sqrt{n_1}\kappa_1\left(\frac{U_0}{h_0}\right)^{n_1}+\sqrt{n_2}\kappa_2\left(\frac{U_0}{h_0}\right)^{n_2}\right)$$
$$+\overline{k}\left(\frac{12U_0}{\gamma}\left(\mu_2|_{r=r_0}-\mu_1|_{r=r_0}\right)+2\alpha\cos\theta_c+\frac{{h_0}^2}{{r_0}^2}\right)-\frac{{h_0}^2}{{r_0}^2}\overline{k}^3\Bigg]\frac{\gamma}{12h_0\left(\kappa_1\sqrt{n_1}\left(\frac{U_0}{h_0}\right)^{n_1}+\kappa_2\sqrt{n_2}\left(\frac{U_0}{h_0}\right)^{n_2}\right)}<0. \tag{3.20}$$

3.5 Comparison between experimental and theoretical results

Using the linear stability analysis with an effective Darcy's law model, we derive the expression of the dimensionless perturbation growth rate ($\overline{\sigma}$) depending on the dimensionless wavenumber of the perturbation ($\overline{k}$) in Eq. (3.17), rheological properties of the fluids (κ_j, n_j, τ_{cj}), the gap gradient (α) as well as the velocity, radius, and gap thickness at the interface (U_0, r_0, h_0, respectively), in addition to various factors affecting simple Newtonian fluid counterpart, such as viscosity contrast λ, Ca, γ and wetting angle (θ_c).

If the pertubation's growth rate is less than zero for every dimensionless wavenumber, $\overline{k}$, the interface will always be stable. We obtain the growth rate at the most unstable mode by substituting the wavenumber of maximum growth $\bar{k}_{max}$ [Eq. (3.18)] and into [Eq. (3.17)]. Taking the values of viscosity (μ_1 and μ_2), U_0, r_0 and h_0 from the experiments, we plotted the $\overline{\sigma}(\bar{k}_{max})$ using Eq. (3.17) in Fig. 3.3(a). Theoretically, we would expect the transition between stable and unstable experiments around 0 as the perturbation decays (or grow) for a negative (positive) growth rate. Fig. 3.3(a) shows a clear transition from stable to unstable interfaces for (S2), revealing unstable interfaces with fingering pattern when $\overline{\sigma}(\bar{k}_{max}) > 7.5$.

The deviation between our experimental results and the theory can be explained by the few assumptions made. The impact of the gravity and the elastic properties have been neglected. Moreover, whenever the gap-gradient, α, is sufficiently large, the assumptions of small ratio of gap change ($\frac{\alpha(r-r_0)}{h_0} << 1$) as well as the characteristic length scale over which the depths varies being much larger than that of the perturbation scaling (i.e., $\frac{kh_0}{\alpha r_0} >> 1$)

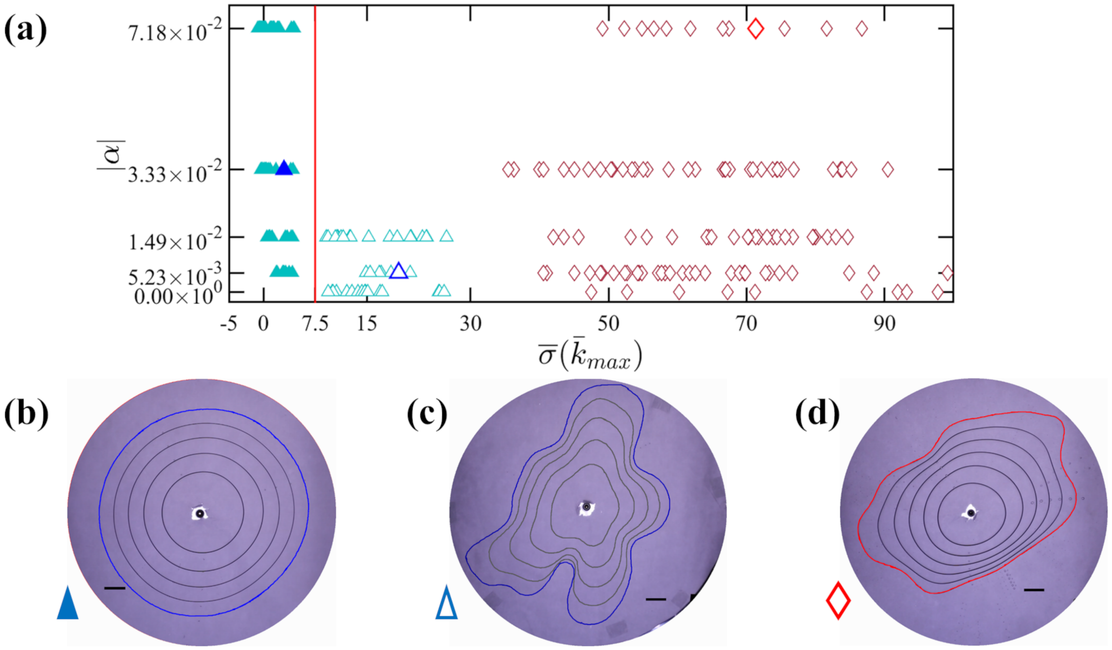

Figure 3.3. **Comparison between experimental and theoretical results**: (a) The growth rate of the perturbation at the most unstable mode of k_{max}, $\overline{\sigma}(\bar{k}_{max})$ using Eq. (3.17) and (3.18) for different experiments performed with various gap gradient, $|\alpha|$. The values of U_0, r_0, and h_0 are taken from the experiments. The wavenumber here corresponds to the wavenumber of maximum growth, $\overline{k} = \bar{k}_{max}$ [Eq. (3.18)]. On the one hand, the experiments with the more viscous solution (S1) always show unstable wavy interface (with data points ◇). On the other, for the less viscous complex fluid (S2), stable displacement (▲) and unstable interface (△) are observed with nearly-zero and relatively-large growth rate $\overline{\sigma}$, respectively. (b)-(d) are the overlays of experimental snapshots, revealing the evolution of the fluid-fluid interface profiles for the three big symbols (▲, △, ◇) in (a), respectively. The interfaces highlighted in red or blue correspond to the data of these symbols analyzed in (a). The time steps are $\delta t = 22$ s, $\delta t = 0.6$ s and $\delta t = 1$ s in (b), (c) and (d), respectively. Each scale bar represent a length scale of 20 mm.

are not fulfilled. Finally, we also neglect the yield stress with respect to the viscous stress. All these assumptions could explain the shift of the experimental critical $\overline{\sigma}(\bar{k}_{max})$ from the theoretical value of 0 to 7.5.

3.6 Conclusions

The stabilization of the viscous fingering instability of complex, yield-stress fluids using a tapered cell has been demonstrated experimentally and theoretically for the first time. Notably, for the less-viscous complex fluids (S2), we obtain a stability diagram (α v.s Q) that shows a clear transition from a stable interface regime showing a complete sweep to an unstable regime with fingering pattern. With a linear stability analysis using an effective Darcy's law, we derive the dispersion relation for the perturbation, Eq. (3.17), and a stability criterion Eq. (3.20). The latter depends on three important types of parameters: first, the fluid's rheological parameters, namely κ, τ_c and n, γ, θ_c; second, the gap gradient (α); lastly, the interface position, gap thickness and velocity (r_0, h_0 and U_0, respectively). Taking the experimental values of U_0, r_0 and h_0, we calculate the perturbation's growth rate ($\overline{\sigma}$) for the most unstable mode of the perturbation ($\bar{k}_{max}$), we compare this theoretical criterion to the experimental results using two distinct yield-stress fluids.

For the very viscous fluid (S1), our theory always predicts unstable displacements which is in total agreement with our experimental results. For the second fluid (S2), we observe a transition between stable and unstable interfaces for $\overline{\sigma}(\bar{k}_{max}) = 7.5$. Theoretically, one would expect the transition to be around 0, as a negative perturbation's growth rate for a stable interface. This discrepancy may be due to some assumptions we made in the analytical derivation. For example, the impact of the gravity, the elastic properties of the fluids, and the yield stress with respect to the viscous stress have been neglected. Further assumptions include the use of the static contact angle, small relative perturbation, and small gap-thickness change. All these assumptions may play a role in the final criterion of the derivation and cause the discrepancy and require future investigations.

Chapter 4

Viscous Fingering of Yield-Stress Fluids in a Tapered Radial Hele-Shaw Cell: Impact of the Bingham Number

1

4.1 Introduction

When a less viscous fluid is pushing another more viscous one in a porous medium, an interfacial instability occurs producing an incomplete sweep of displaced fluid. This instability, so-called viscous fingering due to the wavy finger-like shape of the interface, was first observed in an horizontal Hele-Shaw cell by Saffman and Taylor [5]. Such perturbation of the interface is detrimental for many applications in various natural and industrial fields. Some examplary applications include chromatographic separation of solvents [11], coating flows [8, 12, 13], printing devices [7], groundwater pollution [15, 16], enhanced oil recovery (EOR) process [19, 22], or CO_2 storage and sequestration technologies [24, 25, 26]. Due

---

[1] The material presented in this chapter is based on a manuscript in preparation by Alban Pouplard and Peichun Amy Tsai, "On the Linear Stability Criterion of Viscous Fingering Instability for Complex Fluids in a Tapered Geometry," in preparation, 2021.

to its extensive impact on myriads of industrial processes, the classical viscous fingering has been extensively studied for the past decades. However, most investigations concern Newtonian fluids in a Hele-Shaw cell, consisting of two parallel plates with a constant gap thickness, as set-up [40, 41, 44, 43, 74]. Recently, the investigation of the phenomenon has been extended to complex non-Newtonian fluids. Using shear-thinning (shear-thickening) fluids, the fingers are getting thicker (wider) than the usual fingers for simple Newtonian fluids [30, 48, 49, 64]. With the addition of surfactants, viscous fingers become wider as well [54]. Moreover, previous experiments with colloidal solutions or with yield-stress fluids show new interesting pattern with multiple small fingers forming on the side of the major ones [50, 57, 67, 68, 70].

In order to enhance the efficiency of various industrial applications, the feasibility of controlling or inhibiting the viscous fingering has been investigated with simple Newtonian fluids. Several strategies have already been developed to suppress the primary Saffman-Taylor instability, e.g., using time-dependent injection flow rate [76, 77, 79], the use of an elastic membrane [90, 91, 92], and a thickness-gradient [78, 85, 86]. However, such primary control has not been reported for complex fluids. In this chapter, we study the feasibility of inhibiting the apparition of the viscous fingering instability for nitrogen pushing a complex yield-stress solution in a radially-tapered cell. To this end, we perform a linear stability analysis generalized for two complex, yield-stress fluids pushing one another in a converging gap. We start from the continuity equation and the Darcy's law in which we replaced the constant viscosity, μ, by an effective shear-dependent viscosity, μ_{eff}. In addition to Chapter 3, without any assumption regarding the Bingham number, we obtain a new expression for the dimensionless perturbation's growth rate, which depends on the fluid's rheology, the gap gradient (α), and the interface's local parameters such as the gap thickness, velocity and radius. We further compare the theoretical prediction with our very recent experimental results presented in Chapter 3 and find good agreement.

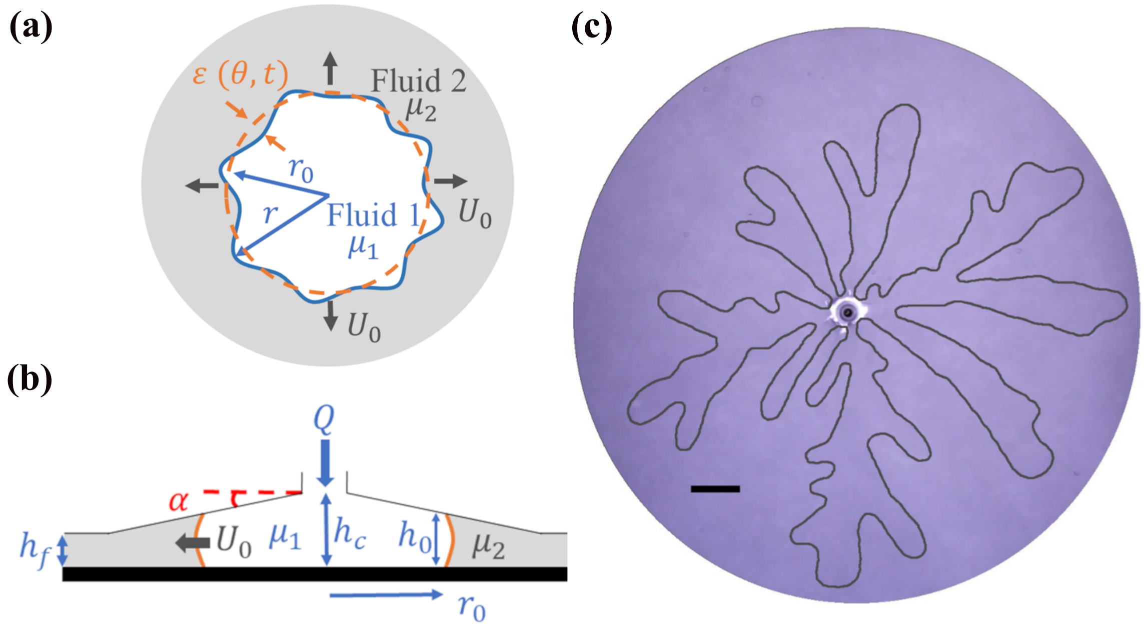

Figure 4.1. (a)–(b) Schematics of top-view and side-view fluid-fluid displacement experimental setup, where a more-viscous complex fluid of viscosity μ_2 varying with shear rate ($\dot{\gamma}$), is pushed by another immiscible one. (c) Representative experimental snapshot of complex viscous fingering obtained when the complex yield-stress (PAA) solution (S1) is displaced by nitrogen gas injected with a flow rate $Q = 0.03$ slpm in a flat Hele-Shaw cell. The scale bar corresponds to 20 mm.

4.2 Experimental

The experiments are conducted using both flat Hele-Shaw and converging-tapered cells under a radial injection (See Fig.4.1(a)-(b)). We use two aqueous solutions of PolyAcrylic Acid (PAA) of different concentrations, denoted as (S1) and (S2), for the wetting and receding fluid to examine complex fluids' viscous fingering. The displacing fluid is gaseous nitrogen of viscosity $\mu_1 = 1.76 \times 10^{-5}$ Pa.s (at 20 °C), achieving the viscosity contrast of $\lambda = \mu_2/\mu_1$ ranging from 2.68×10^4 to 1.16×10^7 and from 1.61×10^3 to 1.67×10^5 for (S1) and (S2), respectively. Other major control parameters are the gap gradient of the cell, α, and the constant flow injection rate, Q, ranging from 0.02 slpm to 2 slpm. The detailed experimental setup and procedures can be found in Chapter 3.

The two yield-stress solutions possess different viscosity values, but both can be modeled

Yield-stress solution	PAA (wt %)	NaOH (wt %)	τ_c (Pa)	κ (Pa.s^n)	n
(S1)	0.10	0.034	3.2857	7.1179	0.3721
(S2)	0.10	0	0.0596	0.1413	0.6333

Table 4.1

Empirical rheological parameters of the two complex, yield-stress fluids, (S1) and (S2), with the Herschel–Bulkley (HB) model [Eq. (4.1)].

well by the Herschel–Bulkley (HB) model [61] of shear stress (τ) varying with shear rate ($\dot{\gamma}$) as:

$$\tau = \tau_c + \kappa\dot{\gamma}^n, \tag{4.1}$$

with τ_c, κ and n corresponding to the yield stress, the consistensy index, and the power-law index, respectively. The different parameters constituting the (HB) model, for both fluid (S1) and (S2), are summarized in Table 4.1.

With flat Hele-Shaw cells we observe side-branched fingering pattern (see Fig. 4.1(c)), as typical characteristic for yield-stress fluids by previous studies [65, 67, 68] as well as more usual viscous fingers pattern (Fig. 4.2(a)). This second type of viscous fingering having already been observed with Newtonian fluids in earlier works. By contrast, using converging cells we observe the elimination of side-branching fingers for both fluids (S1) and (S2), replaced by typical smoother classical VF, as also found lately by Eslami et al. [89]. More significantly, we are able to experimentally observe the inhibition the primary viscous fingering instability under suitable rheological and flow parameters (Q, α, h_c), as illustrated by Fig. 4.2(b). The detailed experimental stability diagram of controlling VF under various α and Q for the complex fluid (S2) can be found in our previous chapter (Ch. 3).

The significant observations of our recent experiments using complex fluids include, first, the interface can become stable at lower Q while keeping α and h_c constant. Second, the transition between stable and unstable displacements occurs at higher Q as the converging gap gradient becomes steeper. Finally, the controlling criterion of the Viscous Fingering instability with yield-stress fluids is rather complex in that α, Q, and the rheological parameters (via κ, n, and local $\dot{\gamma}$) all have a crucial influence on the stabilizing effort of the

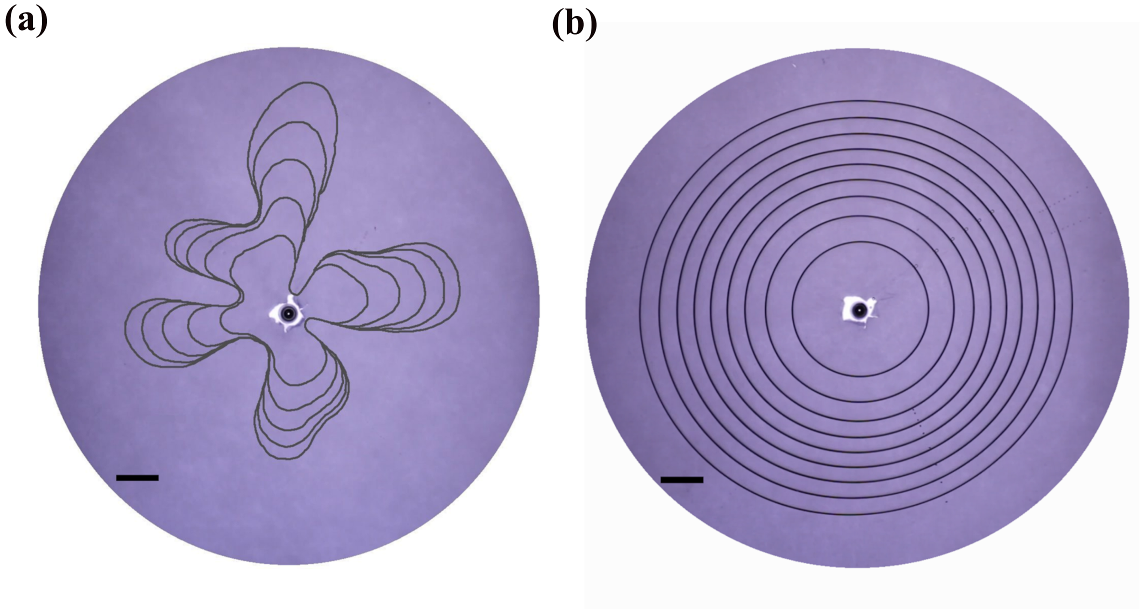

Figure 4.2. **Experimental Data of interfacial profiles** obtained when a gas displaces a yield-stress fluid using different cells. (a) Overlay of experimental snapshots of a viscous fingering pattern observed when a gas is pushing complex solution (S2) in a flat Hele-Shaw cell with $h_c = 0.5$ mm and $Q = 0.025$ slpm (with the time step of $\delta t = 2$ s). (b) By contrast, overlay of experiment snapshots of a stable interface obtained when the gas is pushing (S2) in a radially-tapered cell with a linearly converging gap-thickness: $h = h_c + \alpha r$, where $\alpha = -7.18 \times 10^{-2}$ with $h_c = 10.39$ mm and $Q = 0.025$ slpm. The time interval is $\delta t = 40$ s. Both scale bars correspond to a distance of 20 mm.

fluid-fluid interface.

4.3 Theoretical Analysis

We carry out a linear stability analysis to shed light on the feasibility of controlling the viscous fingering instability for complex, yield stress fluids using a radial tapered Hele-Shaw cell. The problem considered is one complex yield-stress fluid (Fluid 1) of viscosity (μ_1) pushing another yield-stress fluid (Fluid 2) of viscosity (μ_2) in a radially-tapered cell (see Fig. 4.1). The gap gradient (α) introduced produces a linearly-varying height (h) between the two plates of the cell. We consider a lubrication flow confined in the thin gap, whose height varies linearly in r direction as $h(r) = h_c + \alpha r$. Here, h_c denotes the gap thickness at the center of the cell. Considering the fluids' interface at $r = r_0$, the height h is expressed as $h(r) = h_0 + \alpha\,(r - r_0)$, where h_0 the gap thickness between the two plates at the fluid-fluid interface.

In the theoretical derivation, we use the effective Darcy's law replacing the conventional Newtonian fluid' constant viscosity with the effective shear-dependent viscosity, μ_{eff}, for complex fluids. This approach has been used to model non-Newtonian flow in a homogeneous porous medium [30, 49, 54], but here we extend the approach to a tapered geometry. Neglecting the fluids' elastic properties [70], the governing equations of the problem are 2D-depth-average Darcy's law and continuity equation:

$$\mathbf{U}_j = -\frac{h^2}{12\mu_{\text{eff}j}}\vec{\nabla}P_j \ , \tag{4.2}$$

$$\nabla \cdot (h\mathbf{U}_j) = 0. \tag{4.3}$$

$\mathbf{U}_j(r,\theta) = (u_{rj}, u_{\theta j})$ and $P_j(r,\theta)$ are the depth-average velocity and pressure fields of the fluid indexed j, respectively. j represents the two complex fluids during the fluid-fluid displacement process; $j = 1$ (2) denotes the pushing (displaced) complex fluid.

The complex fluid's viscosity ($\mu_{\text{eff}j}$) is modeled using the Herschel-Bulkley law for yield-stress fluids [61], with the local shear rate $\dot{\gamma} = \frac{u_{rj}}{h}$, and expressed as

$$\mu_{\text{eff}j} = \frac{\tau_{cj}}{\dot{\gamma}} + \kappa_j\dot{\gamma}^{n_j-1}, \tag{4.4}$$

where τ_{cj}, κ_j and n_j correspond to the yield stress, the consistensy index, and the power-law index, respectively.

By defining the Bingham number as the ratio of the yield to viscous stress: $Bn_j = \frac{\tau_{cj}}{\kappa_j\left(\frac{u_{rj}}{h}\right)^{n_j}}$, we express $\frac{\tau_{cj}}{\frac{h}{12}\frac{\partial P_j}{\partial r}} = -\frac{1}{1+\frac{1}{Bn_j}}$. Assuming a small ratio of gap-thickness change, i.e., $\frac{\alpha(r-r_0)}{h_0} << 1$, we can linearize the expression of the gap thickness as $h = h_0\left(1 + \frac{\alpha(r-r_0)}{h_0}\right)$ by neglecting the high-order terms of $\mathcal{O}(\alpha^2)$. With Eqs. (4.2)–(4.4), the depth-average continuity Eq. (4.3) can be expressed using the pressure field (P_j) and simplified into

$$\frac{\partial^2 P_j}{\partial r^2} + \frac{n_j}{r}\frac{\partial P_j}{\partial r} + \frac{(2n_j+1)\,\alpha}{h_0}\frac{\partial P_j}{\partial r} + \frac{12 n_j \alpha \tau_{cj}}{h_0^2} + \frac{12 n_j \tau_{cj}}{h_0 r} + \frac{12 n_j \tau_{cj}\alpha}{{h_0}^2}\frac{r_0}{r}$$
$$+ \frac{n_j}{r^2}\frac{\partial^2 P_j}{\partial \theta^2}\left(1 - \frac{1}{1+\frac{1}{Bn}}\right) + \frac{1}{r^2}\frac{\partial P_j}{\partial \theta}\left[(1-n_j)\frac{\frac{\partial^2 P_j}{\partial\theta\partial r}}{\frac{\partial P_j}{\partial r}} - n_j \frac{\tau_{cj}\frac{\partial^2 P_j}{\partial\theta\partial r}}{\frac{h}{12}\left(\frac{\partial P_j}{\partial r}\right)^2}\right] = 0. \tag{4.5}$$

For the simple Newtonian fluids with $n_j = 1$ and $\tau_{cj} = 0$, we find the following equation: $\frac{\partial^2 P_j}{\partial r^2} + \frac{1}{r}\frac{\partial P_j}{\partial r} + \frac{3\alpha}{h}\frac{\partial P_j}{\partial r} + \frac{1}{r^2}\frac{\partial^2 P_j}{\partial \theta^2} = 0$, which is identical and recovered to the case found by Stone et al. [78] for Newtonian fluids.

To solve for the pressure field, P_j, we decompose the solutions into the base and perturbed states with

$$P_j(r,\theta,t) = f_j(r) + g_{kj}(r)\epsilon(\theta,t), \tag{4.6}$$

where the perturbation $\epsilon(\theta,t) = \epsilon_0 r_0(t)\exp(ik\theta + \sigma t)$. Here, $f_j(r)$ corresponds to the base-state, pressure field when the interface does not depend on θ. The $g_{kj}(r)\epsilon$ term represents the perturbation propagating from the interface with wavenumber, k, and growth rate, σ, of the perturbation.

Focusing on the moment when the perturbation starts to propagates, the perturbation is still small ($\epsilon << 1$) so that $g'_{kj}(r)\epsilon << f'_j(r)$. Linearizing around the base state, we can express $r = r_0(1+\epsilon_0 z)$ with $\epsilon_0 << 1$. Substituting the pressure expression Eq. (4.6) into Eq. (4.5), neglecting higher-order terms of $\mathcal{O}(\epsilon^2)$ but not $\mathcal{O}({\epsilon_0}^2 k^2)$, and linearizing $\frac{1}{1+\epsilon_0 z}$ and $\frac{1}{(1+\epsilon_0 z)^2}$, the solutions of the base and perturbed states can be found with the following Eqns:

$$\frac{\partial^2 f_j(z)}{\partial z^2} + n_j \epsilon_0 \frac{\partial f_j(z)}{\partial z} + \frac{(2n_j+1)\,\alpha}{h_0}\epsilon_0 r_0 \frac{\partial f_j(z)}{\partial z} = 0. \tag{4.7}$$

$$\frac{\partial^2 g_{kj}(z)}{\partial z^2} + n_j \epsilon_0 \frac{\partial g_{kj}(z)}{\partial z} + \frac{(2n_j+1)\,\alpha}{h_0}\epsilon_0 r_0 \frac{\partial g_{kj}(z)}{\partial z} - n_j k^2 {\epsilon_0}^2 g_{kj}\left(1 + \frac{\tau_{cj}}{\frac{h}{12}\frac{\partial P_j}{\partial r}}\right) = 0. \tag{4.8}$$

From the Darcy's law, with the fact that $g'_{kj}(r)\epsilon << f'_j(r)$ at $r = r_0$, and $z = \frac{r-r_0}{\epsilon_0 r_0}$, we solve Eqn. (4.7) for the base-state pressure solution:

$$\begin{aligned}
f_j(r) &= F_j \exp\left(-\left(n_j + \frac{(2n_j+1)\,\alpha r_0}{h_0}\right)\frac{r-r_0}{r_0}\right),\\
F_j &= \frac{12\left[\tau_{cj} + \kappa_j\left(\frac{U_0}{h_0}\right)^{n_j}\right]}{h_0}\frac{r_0}{n_j + \frac{(2n_j+1)\alpha r_0}{h_0}},
\end{aligned} \tag{4.9}$$

where U_0 is the velocity at the interface.

Assuming $\epsilon_0 << 1$, we have $\frac{\partial P_j}{\partial r} \approx f_j'(r)$, linearizing $h_0 + \alpha\,(r - r_0) = h_0\left(1 + \frac{\alpha r_0 \epsilon_0 z}{h_0}\right)$ around h_0, and neglecting the terms $\mathcal{O}\left(\epsilon^2\right)$, $\mathcal{O}(\epsilon_0{}^3 k^2)$ but not $\mathcal{O}\left(\epsilon_0{}^2 k^2\right)$, Eq. (4.8) transforms into:

$$\begin{aligned}
&\frac{\partial^2 g_{jk}(z)}{\partial z^2} + n_j \epsilon_0 \frac{\partial g_{kj}(z)}{\partial z} + \frac{(2n_j+1)\,\alpha}{h_0}\epsilon_0 r_0 \frac{\partial g_{kj}(z)}{\partial z}\\
&- n_j k^2 \epsilon_0{}^2 g_{kj}\left(1 - \frac{\tau_{cj}}{\tau_{cj} + \kappa_j\left(\frac{U_0}{h_0}\right)^{n_j}}\exp\left(\left(n_j + \frac{(2n_j+1)\,\alpha r_0}{h_0}\right)\epsilon_0 z\right)\right) = 0.
\end{aligned} \tag{4.10}$$

We define the following constants to simplify the above expression:

$$\begin{aligned}
A_j &= \left(n_j + \frac{(2n_j+1)\,\alpha r_0}{h_0}\right),\\
B_j &= n_j k^2,\\
C_j &= \frac{\tau_{cj}}{\left(\tau_{cj} + \kappa_j\left(\frac{U_0}{h_0}\right)^{n_j}\right)} = \frac{\tau_{cj}}{\tau_{tj}},
\end{aligned} \tag{4.11}$$

where A_j, B_j and C_j correspond to the characteristic length of the exponential term of the base-state pressure [see Eq. (4.9)], the impact of the perturbation's wavenumber, and the ratio of the yield stress (τ_c) to the total stress (τ_t), respectively.

The general solution ($u_{\mathrm{Sol\ j}}$) for the above Eq. (4.10) is a linear combination of the first-order and second-order Bessel functions, $J(\beta, z)$ and $Y(\beta, z)$, respectively. By defining

$$\begin{aligned}
N_j &= \frac{\sqrt{A_j{}^2 + 4B_j}}{A_j},\\
M_j(z) &= \frac{2\sqrt{B_j C_j}}{A_j}\exp\left(\frac{A_j \epsilon_0 z}{2}\right),
\end{aligned} \tag{4.12}$$

the general solution is:

$$\begin{aligned}
&u_{\text{Sol j}}(z) = C1_{kj}\exp\left(\frac{-A_j\epsilon_0 z}{2}\right)J\left(N_j, M_j(z)\right) + C2_{kj}\exp\left(\frac{-A_j\epsilon_0 z}{2}\right)Y\left(N_j, M_j(z)\right) \\
&+ C3_{kj}\exp\left(\frac{-A_j\epsilon_0 z}{2}\right)J\left(-N_j, M_j(z)\right) + C4_{kj}\exp\left(\frac{-A_j\epsilon_0 z}{2}\right)Y\left(-N_j, M_j(z)\right) \\
&+ C5_{kj}\exp\left(\frac{-A_j\epsilon_0 z}{2}\right)J\left(-N_j, -M_j(z)\right) + C6_{kj}\exp\left(\frac{-A_j\epsilon_0 z}{2}\right)Y\left(-N_j, -M_j(z)\right) \\
&+ C7_{kj}\exp\left(\frac{-A_j\epsilon_0 z}{2}\right)J\left(N_j, -M_j(z)\right) + C8_{kj}\exp\left(\frac{-A_j\epsilon_0 z}{2}\right)Y\left(N_j, -M_j(z)\right). \qquad (4.13)
\end{aligned}$$

Note that $J(\beta, z)$ or $Y(\beta, z)$ are regular functions throughout the z-plane cut along the negative real axis [98], meaning $J(\beta, \mathcal{M}(z))$ or $Y(\beta, \mathcal{M}(z))$ are only defined for $\mathcal{M}(z) > 0$. We can then simplify the solution for Eq. (4.13) as

$$\begin{aligned}
u_{\text{Sol j}}(z) =&C1_{kj}\exp\left(\frac{-A_j\epsilon_0 z}{2}\right)J\left(N_j, \frac{2\sqrt{\exp(A_j\epsilon_0 z)B_jC_j}}{|A_j|}\right) \\
&+ C2_{kj}\exp\left(\frac{-A_j\epsilon_0 z}{2}\right)Y\left(N_j, \frac{2\sqrt{\exp(A_j\epsilon_0 z)B_jC_j}}{|A_j|}\right) \\
&+ C3_{kj}\exp\left(\frac{-A_j\epsilon_0 z}{2}\right)J\left(-N_j, \frac{2\sqrt{\exp(A_j\epsilon_0 z)B_jC_j}}{|A_j|}\right) \\
&+ C4_{kj}\exp\left(\frac{-A_j\epsilon_0 z}{2}\right)Y\left(-N_j, \frac{2\sqrt{\exp(A_j\epsilon_0 z)B_jC_j}}{|A_j|}\right).
\end{aligned}$$

Moreover, physically, it is impossible for the perturbation to grows in space from its origin, implying that for a fluid indexed 1 pushing a fluid indexed 2 we have

$$\begin{aligned}
u_{\text{Sol 1}}|_{r\to 0} &= 0, \\
u_{\text{Sol 2}}|_{r\to +\infty} &= 0, \\
u_{\text{Sol 1}}|_{z\to -\infty} &= 0, \\
u_{\text{Sol 2}}|_{z\to +\infty} &= 0.
\end{aligned}$$

Performing analyses on the functional limits as z approaching to $-\infty$ and $+\infty$, we observe that only $\exp\left(\frac{-A_j\epsilon_0 z}{2}\right)J\left(N_j, \frac{2\sqrt{\exp(A_j\epsilon_0 z)B_jC_j}}{|A_j|}\right) \to 0$ as $z \to -\infty$, and only $\exp\left(\frac{-A_j\epsilon_0 z}{2}\right)J\left(-N_j, \frac{2\sqrt{\exp(A_j\epsilon_0 z)B_jC_j}}{|A_j|}\right) \to 0$ as $z \to +\infty$. In summary, the final solution of r-dependent perturbed state of pressure, $g_{kj}(r)$, fulfilling Eq. (4.10) is expressed by $u_{\text{Sol j}}$

below:

$$u_{\text{Sol j}}(z) = C1_{kj} \exp\left(\frac{-A_j \epsilon_0 z}{2}\right) J((-1)^{j+1} N_j,\ |M_j(z)|), \tag{4.14}$$

where A_j, B_j, and C_j are defined in Eq. (4.11), while N_j and M_j in Eq. (4.12) above.

Assuming that the length scale of the interfacial perturbation ($|\frac{r_0}{k}|$) is much smaller than that of the depth variation characterized by $|\frac{h_0}{\alpha}|$, i.e., $|\frac{\alpha r_0}{k h_0}| = O(\epsilon)$, and transforming $z = \frac{r - r_0}{r_0 \epsilon_0}$, Eq. (4.14) can be further simplified to

$$u_{\text{sol j}}(r) = C1_{kj} \exp\left(\frac{-A_j}{2} \frac{r - r_0}{r_0}\right) J\left((-1)^{j+1} \frac{2\sqrt{n_j} k}{A_j}, \frac{2\sqrt{n_j} k \sqrt{\frac{\tau_{cj}}{\tau_{tj}}} \exp\left(\frac{A_j}{2} \frac{r - r_0}{r_0}\right)}{|A_j|}\right). \tag{4.15}$$

The final solution of the pressure field is then expressed as

$$P_j(r, \theta, t) = f_j(r) + u_{\text{sol j}}(r) \epsilon(\theta, t).$$

We linearize the pressure expression around the interface, $r_{int} = r_0 + \epsilon$, neglect the higher-order terms of $\mathcal{O}(\epsilon^2)$, and obtain

$$P_j|_{r = r_0 + \epsilon} = \frac{12 \tau_{tj} r_0}{A_j h_0} - \frac{12 \tau_{tj}}{h_0} \epsilon + C1_{kj}\ J\left((-1)^{j+1} \frac{2\sqrt{n_j} k}{A_j}, \frac{2\sqrt{n_j} k \sqrt{\frac{\tau_{cj}}{\tau_{tj}}}}{|A_j|}\right) \epsilon. \tag{4.16}$$

We further use the properties of the Bessel functions of the first order (J) and the second order (Y) [98]:

$$J'(N_j, M_j(z)) = M_j'(z) \left(\frac{N_j}{M_j(z)} J(N_j, M_j(z)) - J(N_j + 1, M_j(z))\right), \tag{4.17}$$

$$\frac{2N_j}{M_j(z)} J(N_j, M_j(z)) = J(N_j + 1, M_j(z)) + J(N_j - 1, M_j(z)). \tag{4.18}$$

We linearize the first derivative of P_j at the interface, $r = r_{int} = r_0 + \epsilon$, neglect the higher-order terms of $\mathcal{O}(\epsilon^2)$, and obtain

$$\begin{aligned} \left.\frac{\partial P_j}{\partial r}\right|_{r = r_0 + \epsilon} = & - \frac{12 \tau_{t_j}}{h_0} + \frac{12 \tau_{tj}}{h_0} A_j \frac{\epsilon}{r_0} - C1_{kj} \frac{A_j}{2 r_0}\ J\left((-1)^{j+1} \frac{2\sqrt{n_j} k}{A_j}, \frac{2\sqrt{n_j} k \sqrt{\frac{\tau_{cj}}{\tau_{tj}}}}{|A_j|}\right) \epsilon \\ & + (-1)^{j+1} C1_{kj} \frac{\sqrt{n_j} k}{r_0}\ J\left((-1)^{j+1} \frac{2\sqrt{n_j} k}{A_j}, \frac{2\sqrt{n_j} k \sqrt{\frac{\tau_{cj}}{\tau_{tj}}}}{|A_j|}\right) \epsilon \\ & - C1_{kj} \frac{\sqrt{n_j} k}{r_0} \sqrt{\frac{\tau_{cj}}{\tau_{tj}}} \frac{A_j}{|A_j|}\ J\left((-1)^{j+1} \frac{2\sqrt{n_j} k}{A_j} + 1, \frac{2\sqrt{n_j} k \sqrt{\frac{\tau_{cj}}{\tau_{tj}}}}{|A_j|}\right) \epsilon. \end{aligned} \tag{4.19}$$

To obtain the values of the different constants $C1_{k1}$ and $C1_{k2}$, we will use the velocity continuity condition at the interface:

$$\begin{aligned}\frac{\partial r_{\text{int}}}{\partial t} &= u_{rj}|_{r=r_0+\epsilon},\\ \frac{\partial r_0}{\partial t} + \frac{\partial \epsilon}{\partial t} &= u_{rj}|_{r=r_0+\epsilon},\\ U_0 + \sigma\epsilon &= u_{rj}|_{r=r_0+\epsilon}.\end{aligned} \tag{4.20}$$

With the assumption of $\epsilon << 1$, neglecting the higher order terms of $O(\epsilon^2)$, linearizing $h|_{r=r_0+\epsilon} = h_0\left(1+\frac{\alpha\epsilon}{h_0}\right)$ with $\frac{\alpha\epsilon}{h_0} << 1$, and using the previous approximation $\left|\frac{kh_0}{\alpha r_0}\right| >> 1$ to assume $(-1)^{j+1}\,\frac{2\sqrt{n_j}k}{A_j}+1$ to be equal to $(-1)^{j+1}\,\frac{2\sqrt{n_j}k}{A_j}$, we obtain:
$$J\left((-1)^{j+1}\,\frac{2\sqrt{n_j}k}{A_j}, \frac{2\sqrt{n_j}k\sqrt{\frac{\tau_{cj}}{\tau_{tj}}}}{|A_j|}\right) \approx J\left((-1)^{j+1}\,\frac{2\sqrt{n_j}k}{A_j}+1, \frac{2\sqrt{n_j}k\sqrt{\frac{\tau_{cj}}{\tau_{tj}}}}{|A_j|}\right).$$

Finally, the constant $C1_{kj}$ can be expressed as

$$C1_{kj} = \frac{12\kappa_j}{{h_0}^{n_j+1}} \frac{\left(n_j\sigma r_0 U_0^{n_j-1} + 2n_j{h_0}^{n_j}\frac{\tau_{cj}}{\kappa_j}\frac{\alpha r_0}{h_0} + n_j{h_0}^{n_j}\frac{\tau_{cj}}{\kappa_j} + n_j{U_0}^{n_j} + n_j{U_0}^{n_j}\frac{\alpha r_0}{h_0}\right)}{J\left((-1)^{j+1}\,\frac{2\sqrt{n_j}k}{A_j}, \frac{2\sqrt{n_j}k\sqrt{\frac{\tau_{cj}}{\tau_{tj}}}}{|A_j|}\right)\left(\frac{A_j}{2} + (-1)^j\,\sqrt{n_j}k + \sqrt{n_j}k\sqrt{\frac{\tau_{cj}}{\tau_{tj}}}\frac{A_j}{|A_j|}\right)}. \tag{4.21}$$

The Capillary pressure jump at the interface is described by the Young-Laplace equation, which accounts for both the lateral curvature (Ψ) and the curvature due to the depth of the Hele-Shaw cell $\left(\frac{1}{h}\right)$. However, here we neglect the contributions of the viscous stresses to the pressure difference across the interface. At the interface, $r = r_0 + \epsilon(\theta, t)$, for a fluid indexed 1 pushing a fluid indexed 2, the pressure difference across the interface is approximated by the Young-Laplace pressure [78]:

$$P_1 - P_2 = \frac{2\gamma\cos\theta_c}{h_0 + \alpha\epsilon} + \gamma\Psi, \tag{4.22}$$

$$\Psi = \frac{r^2 + 2\left(\frac{\partial r}{\partial\theta}\right)^2 - r\frac{\partial^2 r}{\partial\theta^2}}{\left(r^2 + \left(\frac{\partial r}{\partial\theta}\right)^2\right)^{\frac{3}{2}}}, \tag{4.23}$$

with γ and θ_c corresponding to the interfacial tension and the contact angle of the wetting fluid to the side wall, respectively.

With the assumptions of $\epsilon << 1$ and $\frac{\alpha\epsilon}{h_0} << 1$, neglecting the higher-order terms of $O\left(\alpha^2\right)$, we can linearize the term $\frac{2\gamma\cos\theta_c}{h_0+\alpha\epsilon}$. Moreover, with the fact that ${r_0}^2 >> \epsilon^2$, by linearizing around r_0 and neglecting $\mathcal{O}(\epsilon^2)$, the Young-Laplace equation at the interface for $r = r_0 + \epsilon(\theta, t)$ transforms into

$$P_1 - P_2 = \frac{2\gamma\cos\theta_c}{h_0} + \frac{\gamma}{r_0} + \gamma\epsilon\left(\frac{k^2-1}{{r_0}^2} - \frac{2\alpha\cos\theta_c}{{h_0}^2}\right) + O\left(\epsilon^2\right). \tag{4.24}$$

The first two terms on the right hand side (RHS) correspond to the base state, i.e., the pressure difference at the interface between the two fluids when the interface is stable. The third term on the RHS of Eq. (4.24) is the additional Laplace pressure due to the perturbation at the interface.

We substitute the expression of the linearized pressure Eq. (4.16) into Eq. (4.24) and remove all the components corresponding to the base state. With the result of Eq. (4.21), we finally derive the dimensionless dispersion-relation with the dimensionless growth rate of the perturbation ($\overline{\sigma} = \frac{\sigma r_0}{U_0}$) and the dimensionless wavenumber of the perturbation ($\overline{k} = k$):

$$\begin{aligned}\overline{\sigma} = &\left[\frac{\gamma\overline{k}^2{h_0}^2}{12{r_0}^2U_0} - \frac{\gamma{h_0}^2}{12{r_0}^2U_0} - \frac{2\gamma\alpha\cos\theta_c}{12U_0} + \left(\mu_1|_{r=r_0} - \mu_2|_{r=r_0}\right) + \frac{n_2\mu_2|_{r=r_0} + n_2\frac{\alpha r_0}{U_0}\left(\tau_{t2}+\tau_{c2}\right)}{\frac{A_2}{2} + \sqrt{n_2}\overline{k}\left(1+\sqrt{\frac{\tau_{c2}}{\tau_{t2}}\frac{A_2}{|A_2|}}\right)}\right.\\ &\left.+\frac{n_1\mu_1|_{r=r_0} + n_1\frac{\alpha r_0}{U_0}\left(\tau_{t1}+\tau_{c1}\right)}{-\frac{A_1}{2} + \sqrt{n_1}\overline{k}\left(1-\sqrt{\frac{\tau_{c1}}{\tau_1}\frac{A_1}{|A_1|}}\right)}\right]\frac{-1}{\frac{n_1\kappa_1\left(\frac{U_0}{h_0}\right)^{n_1-1}}{-\frac{A_1}{2}+\sqrt{n_1}\overline{k}\left(1-\sqrt{\frac{\tau_{c1}}{\tau_{t1}}\frac{A_1}{|A_1|}}\right)} + \frac{n_2\kappa_2\left(\frac{U_0}{h_0}\right)^{n_2-1}}{\frac{A_2}{2}+\sqrt{n_2}\overline{k}\left(1+\sqrt{\frac{\tau_{c2}}{\tau_{t2}}\frac{A_2}{|A_2|}}\right)}}.\end{aligned} \tag{4.25}$$

By setting $\frac{\partial\overline{\sigma}}{\partial\overline{k}} = 0$ in the dispersion relation Eq. (4.25), we can find the dimensionless wavenumber of maximum growth ($\bar{k}_{max}$). Furthermore, for each unstable $\bar{k}$, the corresponding dimensionless growth rate ($\bar{\sigma}$) is given by Eq. (4.25) and depends primarily on the rheological parameters of the two complex fluids and the shear rates at the fluid-fluid interface.

From the dispersion-relation Eq. (4.25), the interface would always be stable for a negative perturbation's growth rate ($\overline{\sigma} < 0$) when the following stability criterion is fulfilled:

$$\Bigg[-\frac{\gamma\overline{k}^2{h_0}^2}{12{r_0}^2U_0}+\frac{\gamma{h_0}^2}{12{r_0}^2U_0}+\frac{2\gamma\alpha\cos\left(\theta_c\right)}{12U_0}+\left(\mu_2|_{r=r_0}-\mu_1|_{r=r_0}\right)-\frac{n_2\mu_2|_{r=r_0}+n_2\frac{\alpha r_0}{U_0}\left(\tau_{t2}+\tau_{c2}\right)}{\frac{A_2}{2}+\sqrt{n_2}\overline{k}\left(1+\sqrt{\frac{\tau_{c2}}{\tau_{t2}}\frac{A_2}{|A_2|}}\right)}$$
$$-\frac{n_1\mu_1|_{r=r_0}+n_1\frac{\alpha r_0}{U_0}\left(\tau_{t1}+\tau_{c1}\right)}{-\frac{A_1}{2}+\sqrt{n_1}\overline{k}\left(1-\sqrt{\frac{\tau_{c1}}{\tau_1}\frac{A_1}{|A_1|}}\right)}\Bigg]\frac{1}{\frac{n_1\kappa_1\left(\frac{U_0}{h_0}\right)^{n_1-1}}{-\frac{A_1}{2}+\sqrt{n_1}\overline{k}\left(1-\sqrt{\frac{\tau_{c1}}{\tau_{t1}}\frac{A_1}{|A_1|}}\right)}+\frac{n_2\kappa_2\left(\frac{U_0}{h_0}\right)^{n_2-1}}{\frac{A_2}{2}+\sqrt{n_2}\overline{k}\left(1+\sqrt{\frac{\tau_{c2}}{\tau_{t2}}\frac{A_2}{|A_2|}}\right)}} < 0. \qquad (4.26)$$

4.4 Comparing Experimental vs. Theoretical Results

The linear stability analysis performed above gives a complex expression of the dimensionless perturbation's growth rate (Eq.(4.25)) depending on the dimensionless wavenumber ($\bar{k}$) of the perturbation, rheological properties of the fluids (κ_j, n_j, τ_{cj}), the gap gradient (α) as well as the velocity, radius, and gap thickness at the interface (U_0, h_0, r_0, respectively). Additional factors such as the wetting angle (θ_c), the interfacial tension (γ) also affect the VF stability. Whenever the growth rate is less than 0, the interface would remain stable for the decaying perturbation.

With the experimental values of U_0, h_0 and r_0, we use Matlab to determine numerically the wavenumber of maximum growth ($\bar{k}_{max}$) with an accuracy of 0.001. We then substitute it into the dispersion Eq. (4.25) to obtain the growth rate at the most unstable mode, $\overline{\sigma}(\bar{k}_{max})$. We plot such results for different converging gap gradients (α) in Fig. 4.3. Theoretically, one would expect a transition between stable (●) and unstable displacements (△ and ○) at $\overline{\sigma}(\bar{k}_{max}) = 0$. From Fig. 4.3, we find and highlight the lowest boundary for unstable displacement. The value being for $\overline{\sigma}(\bar{k}_{max}) \approx 4$. For lower values of $|\alpha|$ and up to 1.49×10^{-2}, this boundary could be used as a border to differentiate the stable and the unstable displacements.

However, from Fig. 4.3, one can notice that $\overline{\sigma}(\bar{k}_{max})$ is superior to 4 for stable displacements for higher values of α. This difference may be explained by the assumptions we made concerning α. We assume a small ratio of gap change ($\frac{\alpha(r-r_0)}{h_0} << 1$) as well as much larger characteristic length scale over which the depth varies than that of the perturbation ($\frac{kh_0}{\alpha r_0} >> 1$). Such deviation between theoretical and experimental results for higher values

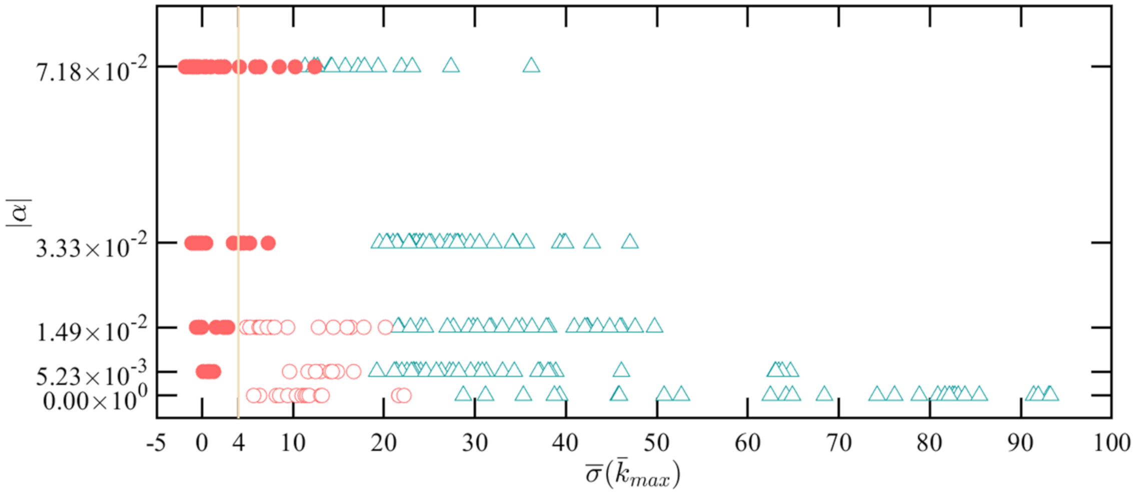

Figure 4.3. **Comparison between experimental and theoretical results** of the perturbation's growth rate of the most unstable mode, $\overline{\sigma}(\bar{k} = \bar{k}_{max})$ [Eq. (4.25)]. The values of U_0, r_0 and h_0 are taken from the experiments. The wavenumber corresponding to the wavenumber of maximum growth ($\bar{k} = \bar{k}_{max}$) is obtained numerically using Matlab. We compare with the experimental results performed with various $|\alpha|$ and differentiate stable displacements (●), obtained solely during experiments with the less-viscous fluid (S2), and unstable wavy interface (△ and ○ for the fluid (S1) and (S2), respectively).

of α has already been noticed in the past when the theoretical stability criterion derived by Stone et al. [78] has been used and compared to radial experimental results from Bongrand et al. [86]. In such work, they compared their experimental results obtained in radially-tapered Hele-Shaw cells with the theoretical stability criterion derived by Stone et al. [78]. They were able to find good agreement for smaller values of α. However, once the absolute value of the gap gradient increases, they found a clear deviation between experiments and theory. Finally, the discrepancy observed by the experimental result of $\overline{\sigma}(\bar{k}_{max}) \approx 4$ may stem from few assumptions made as we neglect the influence of the gravity and the fluid's elastic properties in our linear stability analysis.

4.5 Concluding Remarks

We theoretically derive the stability criterion for the viscous fingering instability of complex yield-stress fluids using a tapered narrow cell. Experimentally, for the very viscous fluid (S1) of viscosity contrast, λ, ranging from 2.68×10^4 to 1.16×10^7, we could observe the elimination of small side-branching fingers but not the primary finger with the tapered cells. However, stable interfaces with the inhibition of the primary VF instability can be achieved for the less-viscous one (S2), λ spanning $1.61 \times 10^3 - 1.67 \times 10^5$. The experimental observation of stability diagram (under various α v.s Q) studied in Chapter 3 shows a clear transition between a complete and incomplete sweep.

Using a linear stability analysis with an effective Darcy's law, we obtain a stability criterion corresponding to the perturbation's growth rate of the most unstable mode. The stability criterion derived for the complex fluids depends on the following three types of important parameters summarized below. First, the fluid's rheology and characteristics and the different constants κ, τ_c and n, γ, θ_c. Second, the gap gradient (α). Lastly, the interface velocity, position gap thickness and velocity (r_0, h_0 and U_0, respectively). We examine this theoretical criterion with the experiments done with the two distinct yield-stress fluids. Taking the experimental values of U_0, r_0 and h_0, we calculated the perturbation's growth rate for the most unstable mode. From the different values obtained, we observe a transition between stable and unstable interfaces for $\overline{\sigma}(\bar{k}_{max}) = 4$, which slightly deviated from the theoretically expected transition around 0. This discrepancy may stem from the assumptions we made in the derivation. For instance, the impact of the gravity and the elastic properties of the fluids have been neglected. We also use a static contact angle for moving fluids and make few assumptions related to the gap gradient (α). Notably, we assume a small ratio of gap change and the characteristic length scale over which the depth varies being much larger than the characteristic length scale of the perturbation. Both assumptions especially impact the results for the larger values of α.

Chapter 5

Conclusions, Recommendations, & Future Works

In this work, we investigate the viscous fingering instability in a rectangular and a radial tapered Hele-Shaw cell both experimentally and theoretically. We are the first to demonstrate the possibility of inhibiting the apparition of the interfacial instability with complex yield-stress fluids by adding a converging taper to the confined cell.

From our experiments, we distinguish two distinct regimes of displacements—a stable and an unstable one. The former stable one is characterized by a straight or a circular interface for the rectangular and radial geometry, respectively. These stable displacements result in a full sweep of the more-viscous complex yield-stress fluids. On the contrary, the unstable displacements can be recognized by their wavy finger-like interfaces. Experimentally, the stable displacements only occur in tapered cells for low values of injection flow rate, Q. In fact, for each gap gradient (α) and complex fluid, we can define a critical flow rate, Q_c, over which the interface destabilizes and the viscous fingering occurs. This value of Q_c depends on the gap gradient and increases as the converging gradient (α) becomes steeper.

Another important observation from our experimental database is that the fluid's viscosity is crucial to stabilize the interface and the displacement. It is harder to obtain a full sweep if the complex yield-stress fluid is too viscous in the first place. That's why we do not see any stable displacements for the most-viscous fluid in Chapter 3, and that previous studies were not able to observe the same stable interfaces as we did.

Besides experiments, another significant part of our work was theoretical. We perform three different stability analyses which applies solely for Darcy's flow in porous media using an effective Darcy's law and the continuity equation as governing equations. We replace the constant viscosity of Newtonian fluids, μ, by an effective shear-dependent viscosity, μ_{eff}, following the Herschel-Bulkley law. In the theoretical analyses, we start with the above governing equations, make the same assumptions, e.g., small relative gradient and perturbation as well as the Bingham approximation, for both radial and rectangular geometries. We obtain two following types of stability criteria for the different cell geometries.

Firstly, from our theoretical derivation, we obtain the expression of the dimensionless perturbation's growth rate ($\bar{\sigma}$) whereby we can calculate the dimensionless wavenumber ($\bar{k}_{max}$) and wavelength (λ_{max}) of the maximum growth mode. For the rectangular geometry, by comparing λ_{max} to the cell width, we obtain an important dimensionless term, $C^* = -3\left(\frac{2\pi h_0}{W}\right)^2 + 2\alpha\cos\theta_c + \frac{12U_0}{\gamma}\left(\mu_2|_{x=0} - \mu_1|_{x=0}\right)$, which is used as the stability criterion for a visible fingering pattern.

Secondly, knowing the wavenumber-dependent growth rate, we substitute $\bar{k}_{max}$ into $\overline{\sigma}$ to obtain the growth rate of the most unstable mode. If the latter is less than zero, the interface should always be stable whatever the wavenumber of the perturbation. We use $\overline{\sigma}(\bar{k}_{max})$ as the stability criterion for the analyses in the radial geometry. In this particular geometry, we also investigate the impact of one key assumption concerning the Bingham number and perform another linear stability analysis without simplification of the Bingham number. We obtain a brand new expression for the dimensionless growth rate of the most unstable mode ($\overline{\sigma}(\bar{k}_{max})$) and observe some improvement of the prediction.

To conclude, we can see a clear separation between the stable and the unstable displacements for the experiments using the theoretical stability criteria. We obtain good agreement between our theoretical analyses and experimental results for both geometries. Our theoretical criteria can be used with pretty good accuracy to estimate whether an interface destabilizes and deforms into a wavy-finger-like shape. However, slight discrepancy exists, mainly due to all the assumptions we made throughout the theoretical derivations to ensure the equations are analytically solvable.

Concerning future work, although we are the first to observe stable displacements for yield-stress fluids, the experimental database of experiments is still limited. To expand the existing parameter space, one can perform more experiments with different gap gradients, different injection flow rates, and various yield-stress fluids. These additional experimental results are also beneficial to test out our theoretical stability criteria truly. For the present, good agreement is found for two or three yield-stress fluids and with a small number of gap gradients. More data is needed to affirm these criteria are accurate entirely.

Finally, it will be interesting to develop a theoretical solution without various assumptions concerning the sizes of the relative perturbation and the relative taper gradient, the impact of gravity, the elastic properties of the fluid, and the use of a static contact angle. However, this analytical work is rather challenging and may not be feasible to obtain analytical results without any assumptions because of complex partial derivative equations that we obtain from the effective Darcy's law and the continuity equation.

Appendix A

Viscosity Measurements and Variations of Poly(Acrylic) Acid Solutions

This appendix reports the measurements and observations about the viscosity changes for the (same) solution (S2) used in our rectangular and radial experiments. This solution is an aqueous solution of Poly(Acrylic acid) (PAA) with a concentration of polymer equal to $c_p = 0.10\%$ wt. The only difference between this solution (S2) and all the others used for our experiments is that we did not used Sodium Hydroxide to neutralize the (S2) acid solution. This solution is a mixture of water and (PAA) polymer only, and somehow the freshly-made solution reveals high viscosity than that used after one or more times of the viscous fingering experiments.

As with all the other solutions, the rheological measurements have been performed with (S2) using an Anton Paar MCR302 rheometer with a concentric cylinder. For each fluid, we performed measurements on freshly-made solutions and after each experiment to see the impact of time and usage rate on the rheological characteristic of the solution.

For the other fluids, we observe their viscosity values stayed nearly unchanged. However, this was not the case for the fluid (S2) shown in Fig. A.1. The figure shows that the fresh

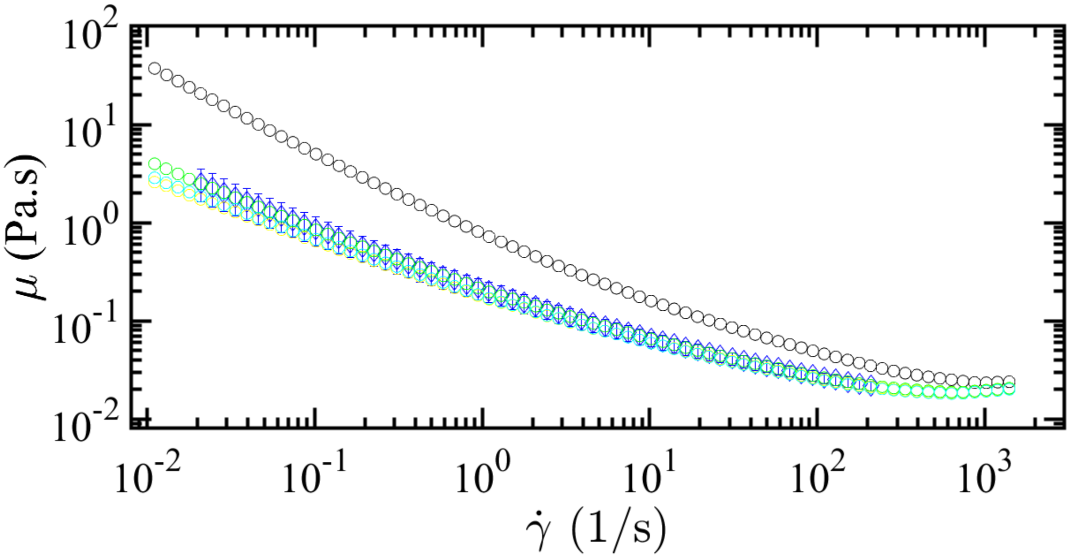

Figure A.1. Viscosity versus shear rate for the solution (S2) after different number of experiments. The symbols (○,○,○ and ○) correspond to the viscosity measurements of the solution after 0, 1, 5 or 9 experiments, respectively. The symbol (◇) corresponds to the mean rheological evolution we fitted with the Herschel-Bulkley model.

solution is more viscous than the same after performing experiments, even after just one. Hopefully, we can notice that the decrease in viscosity is direct from one value to another. After this drastic decrease, we can see small changes in the viscosity evolution between different sets of measurements. Still, the viscosity values stay inside the error margin of our Herschel-Bulkley fitting in Ch. 3.

This solution has been the only one to show such variation with time, and it seems this issue has never been encountered before. From previously published papers, it is possible to imagine two reasons why this variation happens. First, some authors have already noticed that the viscosity of the Poly(acrylic) acid solution is very sensitive to the ionic strength and the neutralization degree [99, 100, 101]. In these articles, they noticed that the variation of viscosity due to a variation of neutralization degree is more important for low values of neutralization degree. When the degree of neutralization is above 0.5, the viscosity stops increasing and reaches nearly a plateau.

It means that if the nitrogen has the capacity to reduce the neutralization degree of the solution when the solution is not neutralized, the viscosity can drastically change; when the solution is neutralized, the viscosity decrease due to the nitrogen being negligible. However, a point is difficult to justify with this hypothesis. We did not notice any major pH changes in the solution before and after the experiments.

The second hypothesis concerns the difference in the microscopic arrangement of the Poly(acrylic acid) polymer between a non-neutralized and a neutralized solution. Indeed, the polymeric chains and the hydrogen bonds are different between the two solutions [102, 103]. Todica et al. found that water clusters exist at the vicinity of the polymeric chains, and we do not necessarily find them for the neutralized solution [103]. Now, knowing that nitrogen dissolves in water, it is possible to assume that the nitrogen is dissolving in this water cluster, reducing the viscosity of the all solution. The viscosity reaches a plateau afterward because the water clusters are saturated with nitrogen. Those clusters do not seem to exist for neutralized solution justifying why the viscosity of the other used solutions remained invariable with time and use.

Finally, we only present the above assumptions and reasoning in this Appendix. Finding the correct reasons for this viscosity change needs a deeper study. We kept using the (S2) solution in subsequent experiments since its viscosity didn't show any significant changes after the first experiment and we were able to find a model of Herschel-Bulkley viscosity law that fits our experimental measurements.

References

[1] K. Ishizaki, S. Komarneni, and M. Nanko. Porous Materials: Process technology and applications. Springer science & business media, 2013.

[2] M. K. Das, P. P Mukherjee, and K. Muralidhar. Modeling transport phenomena in porous media with applications. Springer, 2018.

[3] F. A. L. Dullien. Porous media: fluid transport and pore structure. Academic Press, 1979.

[4] S. Hill. Channeling in packed columns. Chemical Engineering Science, 1:247–253, 1952.

[5] P. G. Saffman and G. Taylor. The penetration of a fluid into a porous medium or hele-shaw cell containing a more viscous liquid. Proceedings of the Royal Society of London. Series A. Mathematical and Physical Sciences, 245:312–329, 1958.

[6] P. Tabeling, G. Zocchi, and A. Libchaber. An experimental study of the saffman-taylor instability. Journal of Fluid Mechanics, 177:67–82, 1987.

[7] E. Pitts and J. Greiller. The flow of thin liquid films between rollers. Journal of Fluid Mechanics, 11:33–50, 1961.

[8] J. Greener, T. Sullivan, B. Turner, and S. Middleman. Ribbing instability of a two-roll coater: Newtonian fluids. Chemical Engineering Communications, 5:73–83, 1980.

[9] M. D. Savage. Mathematical model for the onset of ribbing. AICHE Journal, 30:999–1002, 1984.

[10] M. Rabaud, S. Michalland, and Y. Couder. Dynamical regimes of directional viscous fingering: Spatiotemporal chaos and wave propagation. Physical Review Letters,

64:184, 1990.

[11] E. J. Fernandez, T. T. Norton, W. C. Jung, and J. G. Tsavalas. A column design for reducing viscous fingering in size exclusion chromatography. Biotechnology Progress, 12:480–487, 1996.

[12] A. M. Grillet, A. G. Lee, and E. S. G. Shaqfeh. Observations of ribbing instabilities in elastic fluid flows with gravity stabilization. Journal of Fluid Mechanics, 399:49–83, 1999.

[13] A. G. Lee, E. S. G. Shaqfeh, and B. Khomami. Viscoelastic effects on interfacial dynamics in air-liquid displacement under gravity stabilization. Journal of Fluid Mechanics, 531:59–83, 2005.

[14] K. E. Holloway, H. Tabuteau, and J. R. De Bruyn. Spreading and fingering in a yield-stress fluid during spin coating. Rheologica Acta, 49:245–254, 2010.

[15] A. Lange, M. Schroter, M. A. Scherer, A. Engel, and I. Rehberg. Fingering instability in a water-sand mixture. The European Physical Journal B, 4:475–484, 1998.

[16] R. Maes, G. Rousseaux, B. Scheid, M. Mishra, P. Colinet, and A. De Wit. Experimental study of dispersion and miscible viscous fingering of initially circular samples in hele-shaw cells. Physics of Fluids, 22:123104, 2010.

[17] S. Thomas. Enhanced oil recovery - an overview. Oil and Gas Science and Technology, 63:9–19, 2008.

[18] J. Wang and M. Dong. Optimum effective viscosity of polymer solution for improving heavy oil recovery. Journal of Petroleum Science and Engineering, 67:155–158, 2009.

[19] E. A. Chukwudeme and A. A. Hamouda. Enhanced oil recovery (EOR) by miscible CO_2 and water flooding of asphaltenic and non-asphaltenic oils. Energies, 2:714–737, 2009.

[20] S. C. Cao, B. Bate, J. W. Hu, and J. Jung. Engineering behavior and characteristics of water-soluble polymers: Implication on soil remediation and enhanced oil recovery. Sustainability (Switzerland), 8:205, 2016.

[21] X. Xu, A. Saeedi, and K. Liu. An experimental study of combined foam/surfactant

polymer (SP) flooding for carbone dioxide-enhanced oil recovery (CO_2-EOR). Journal of Petroleum Science and Engineering, 149:603–611, 2017.

[22] Y. Zeng, K. Ma, R. Farajzadeh, M. Puerto, S. L. Biswal, and G. J. Hirasaki. Effect of surfactant partitioning between gaseous phase and aqueous phase on CO_2 foam transport for enhanced oil recovery. Transport in Porous Media, 114:777–793, 2016.

[23] C. Esene, S. Zendehboudi, A. Aborig, and H. Shiri. A modeling strategy to investigate carbonated water injection for EOR and CO_2 sequestration. Fuel, 252:710–721, 2019.

[24] J. Daneshfar, R. G. Hughes, and F. Civan. Feasibility investigation and modeling analysis of CO_2 sequestration in arbuckle formation utilizing salt water disposal wells. Journal of Energy Resources Technology, Transactions of the ASME, 131:0233011–02330110, 2009.

[25] A. R. White and T. Ward. CO_2 sequestration in a radial hele-shaw cell via an interfacial chemical reaction. Chaos, 22:037114, 2012.

[26] E. H. Kimbrel, A. L. Herring, R. T. Armstrong, I. Lunati, B. K. Bay, and D. Wildenschild. Experimental characterization of nonwetting phase trapping and implications for geologic CO_2 sequestration. International Journal of Greenhouse Gas Control, 42:1–15, 2015.

[27] T. Ganat. Pumping system of heavy oil production. In R. M. Gounder, editor, Processing of Heavy Crude Oils - Challenges and Opportunities. InTechOpen, 2019.

[28] A. B. Thompson, A. Juel, and A. L. Hazel. Multiple finger propagation modes in hele-shaw channels of variable depth. Journal of Fluid Mechanics, 746:123–164, 2014.

[29] C. Chevalier, M. Ben Amar, D. Bonn, and A. Lindner. Inertial effects on saffman-taylor viscous fingering. Journal of Fluid Mechanics, 552:83–97, 2006.

[30] M. Ben Amar and E. Corvera Poiré. Pushing a non-newtonian fluid in a hele-shaw cell: From fingers to needles. Physics of Fluids, 11:1757–1767, 1999.

[31] F. M. Rocha and J. A. Miranda. Manipulation of the saffman-taylor instability: A curvature-dependent surface tension approach. Physical Review E - Statistical, Nonlinear, and Soft Matter Physics, 87:013017, 2013.

[32] P. Daripa and X. Ding. A numerical study of instability control for the design of an optimal policy of enhanced oil recovery by tertiary displacement processes. Transport in Porous Media, 93:675–703, 2012.

[33] P. Daripa. Studies on stability in three-layer hele-shaw flows. Physics of Fluids, 20:112101, 2008.

[34] A. He, J. Lowengrub, and A. Belmonte. Modeling an elastic fingering instability in a reactive hele-shaw flow. SIAM Journal on Applied Mathematics, 72:842–856, 2012.

[35] M. Ahmadlouydarab, J. Azaiez, and Z. Chen. Immiscible flow displacements with phase change in radial injection. International Journal of Multiphase Flow, 72:73–82, 2015.

[36] E. Alvarez Lacalle, J. Ortín, and J. Casademunt. Low viscosity contrast fingering in a rotating hele-shaw cell. Physics of Fluids, 16:908–924, 2004.

[37] E. Álvarez Lacalle, J. Ortín, and J. Casademunt. Relevance of dynamic wetting in viscous fingering patterns. Physical Review E - Statistical, Nonlinear, and Soft Matter Physics, 74:025302(R), 2006.

[38] E. O. Dias and J. A. Miranda. Control of centrifugally driven fingering in a tapered hele-shaw cell. Physical Review E - Statistical, Nonlinear, and Soft Matter Physics, 87:053014, 2013.

[39] J. D. Chen. Growth of radial viscous fingers in a hele-shaw cell. Journal of Fluid Mechanics, 201:223–242, 1989.

[40] P. G. Saffman. Viscous fingering in hele-shaw cells. Journal of Fluid Mechanics, 173:73–94, 1986.

[41] G. M. Homsy. Viscous fingering in porous media. Annual Review of Fluid Mechanics, 19:271–302, 1987.

[42] M. G. Moore, A. Juel, J. M. Burgess, W. D. McCormick, and H. L. Swinney. Fluctuations in viscous fingering. Physical Review E - Statistical Physics, Plasmas, Fluids, and Related Interdisciplinary Topics, 65:030601(R), 2002.

[43] J. D. Chen. Radial viscous fingering patterns in hele-shaw cells. Experiments in Fluids,

5:363–371, 1987.

[44] L. Paterson. Radial fingering in a hele shaw cell. Journal of Fluid Mechanics, 113:513–529, 1981.

[45] J. A. Miranda and M. Widom. Radial fingering in a hele-shaw cell: a weakly nonlinear analysis. Physica D, 120:315–328, 1998.

[46] S. S. Park and D. J. Durian. Viscous and elastic fingering instabilities in foam. Physical Review Letters, 72:3347, 1994.

[47] M. Kawaguchi, S. Yamazaki, K. Yonekura, and T. Kato. Viscous fingering instabilities in an oil in water emulsion. Physics of Fluids, 16:1908, 2004.

[48] D. Bonn, H. Kellay, and J. Meunier. Viscous fingering and related instabilities in complex fluids. Philosophical Magazine B: Physics of Condensed Matter; Statistical Mechanics, Electronic, Optical and Magnetic Properties, 78:131–142, 1998.

[49] A. Lindner, D. Bonn, and J. Meunier. Viscous fingering in a shear-thinning fluid. Physics of Fluids, 12:256–261, 2000.

[50] A. Lindner, D. Bonn, and J. Meunier. Viscous fingering in complex fluids. Journal of Physics Condensed Matter, 12:A477–A482, 2000.

[51] L. Kondic, M. J. Shelley, and P. Palffy-Muhoray. Non-newtonian hele-shaw flow and the saffman-taylor instability. Physical Review Letters, 80:1433, 1998.

[52] P. Fast, L. Kondic, M. J. Shelley, and P. Palffy-Muhoray. Pattern formation in non-newtonian hele-shaw flow. Physics of Fluids, 13:1191–1212, 2001.

[53] Y. H. Lee, J. Azaiez, and I. D. Gates. Interfacial instabilities of immiscible non-newtonian radial displacements in porous media. Physics of Fluids, 31:043103, 2019.

[54] D. Bonn, H. Kellay, M. Brunlich, M. Ben Amar, and J. Meunier. Viscous fingering in complex fluids. Physica A, 220:60–73, 1995.

[55] S. Ahmadikhamsi, F. Golfier, C. Oltean, E. Lefèvre, and S. A. Bahrani. Impact of surfactant addition on non-newtonian fluid behavior during viscous fingering in hele-shaw cell. Physics of Fluids, 32:012103, 2020.

[56] H. Van Damme, C. Laroche, L. Gatineau, and P. Levitz. Viscoelastic effects in fingering

between miscible fluids. Journal de Physique, 48:1121–1133, 1987.

[57] E. Lemaire, P. Levitz, G. Daccord, and H. Van Damme. From viscous fingering to viscoelastic fracturing in colloidal fluids. Physical Review Letters, 67:2009, 1991.

[58] H. Van Damme, C. Laroche, and L. Gatineau. Radial fingering in viscoelastic media, an experimental study. Revue de Physique Appliquée, 22:241–252, 1987.

[59] F. Xu, J. Kim, and S. Lee. Particle-induced viscous fingering. Journal of Non-Newtonian Fluid Mechanics, 238:92–99, 2016.

[60] R. Luo, Y. Chen, and S. Lee. Particle-induced viscous fingering: Review and outlook. Physical Review Fluids, 3:110502, 2018.

[61] W. H. Herschel and R. Bulkley. Konsistenzmessungen von gummi-benzollösungen. Kolloid-Zeitschrift, 39:291, 1926.

[62] O. A. Fadoul and P. Coussot. Saffman-taylor instability in yield stress fluids: Theory-experiment comparison. Fluids, 4:53, 2019.

[63] T. Divoux, A. Shukla, B. Marsit, Y. Kaloga, and I. Bischofberger. Criterion for fingering instabilities in colloidal gels. Physical Review Letters, 124:248006, 2020.

[64] A. Lindner, P. Coussot, and D. Bonn. Viscous fingering in a yield stress fluid. Physical Review Letters, 85:314, 2000.

[65] N. Maleki-Jirsaraei, A. Lindner, S. Rouhani, and D. Bonn. Saffman–taylor instability in yield stress fluids. Journal of Physics: Condensed Matter, 17:1219–1228, 2005.

[66] B. Ebrahimi, P. Mostaghimi, H. Gholamian, and K. Sadeghy. Viscous fingering in yield stress fluids: a numerical study. Journal of Engineering Mathematics, 97:161–176, 2016.

[67] A. Eslami and S. M. Taghavi. Viscous fingering regimes in elasto-visco-plastic fluids. Journal of Non-Newtonian Fluid Mechanics, 243:79–94, 2017.

[68] A. Eslami and S. M. Taghavi. Viscous fingering of yield stress fluids: The effects of wettability. Journal of Non-Newtonian Fluid Mechanics, 264:25–47, 2019.

[69] A. Eslami and S. M. Taghavi. Viscoplastic fingering in rectangular channels. Physical Review E, 102:023105, 2020.

[70] P. Coussot. Saffman-taylor instability in yield-stress fluids. Journal of Fluid Mechanics, 380:363–376, 1999.

[71] R. Ledesma-Aguilar, A. Hernández-Machado, and I. Pagonabarraga. Three-dimensional aspects of fluid flows in channels. i. meniscus and thin film regimes. Physics of Fluids, 19:102112, 2007.

[72] V. Sharma, S. Nand, S. Pramanik, C. Y. Chen, and M. Mishra. Control of radial miscible viscous fingering. Journal of Fluid Mechanics, 884:A16, 2019.

[73] X. Fu, L. Cueto-Felgueroso, and R. Juanes. Viscous fingering with partially miscible fluids. Physical Review Fluids, 2:104001, 2017.

[74] L. Paterson. Fingering with miscible fluids in a hele shaw cell. Physics of Fluids, 28:26–30, 1985.

[75] P. A. Sesini, D. A. F. De Souza, and A. L. G. A. Coutinho. Finite element simulation of viscous fingering in miscible displacements at high mobility-ratios. Journal of the Brazilian Society of Mechanical Sciences and Engineering, 32:292–299, 2010.

[76] S. S. Cardoso and A. W. Woods. The formation of drops through viscous instability. Journal of Fluid Mechanics, 289:351, 1995.

[77] E. O. Dias, E. Alvarez Lacalle, M. S. Carvalho, and J. A. Miranda. Minimization of viscous fluid fingering: A variational scheme for optimal flow rates. Physical Review Letters, 109:144502, 2012.

[78] T. T. Al-Housseiny and H. A. Stone. Controlling viscous fingering in tapered hele-shaw cells. Physics of Fluids, 25:092102, 2013.

[79] J. V. Fontana, E. O. Dias, and J. A. Miranda. Controlling and minimizing fingering instabilities in non-newtonian fluids. Physical Review E - Statistical, Nonlinear, and Soft Matter Physics, 89:013016, 2014.

[80] M. Ben Amar and D. Bonn. Fingering instabilities in adhesive failure. Physica D: Nonlinear Phenomena, 209:1–16, 2005.

[81] H. S. Rabbani, D. Or, Y. Liu, C-Y. Lai, N. B. Lu, S. S. Datta, H. A. Stone, and N. Shokri. Suppressing viscous fingering in structured porous media. PNAS, 115:4833–

4838, 2018.

[82] F. K. Eriksen, R. Toussaint, K. J. Måløy, and E. G. Flekkøy. Invasion patterns during two-phase flow in deformable porous media. Frontiers in Physics, 3:81, 2015.

[83] P. Daripa and G. Paşa. On capillary slowdown of viscous fingering in immiscible displacement in porous media. Transport in Porous Media, 75:1–16, 2008.

[84] N. Sabet, H. Hassanzadeh, and J. Abedi. Control of viscous fingering by nanoparticles. Physical Review E, 96:063114, 2017.

[85] T. T. Al-Housseiny, P. A. Tsai, and H. A. Stone. Control of interfacial instabilities using flow geometry. Nature Physics, 8:747–750, 2012.

[86] G. Bongrand and P. A. Tsai. Manipulation of viscous fingering in a radially tapered cell geometry. Physical Review E, 97:061101, 2018.

[87] P. H. A. Anjos, E. O. Dias, and J. A. Miranda. Fingering instability transition in radially tapered hele-shaw cells: Insights at the onset of nonlinear effects. Physical Review Fluids, 3:124004, 2018.

[88] S. J. Jackson, H. Power, D. Giddings, and D. Stevens. The stability of immiscible viscous fingering in hele-shaw cells with spatially varying permeability. Computer Methods in Applied Mechanics and Engineering, 320:606–632, 2017.

[89] A. Eslami, R. Basak, and S. M. Taghavi. Multiphase viscoplastic flows in a nonuniform hele-shaw cell: A fluidic device to control interfacial patterns. Industrial and Engineering Chemistry Research, 59:4119–4133, 2020.

[90] T. T. Al-Housseiny, I. C. Christov, and H. A. Stone. Two-phase fluid displacement and interfacial instabilities under elastic membranes. Physical Review Letters, 111:034502, 2013.

[91] D. Pihler-Puzović, P. Illien, M. Heil, and A. Juel. Suppression of complex finger-like patterns at the interface between air and a viscous fluid by elastic membranes. Physical Review Letters, 108:074502, 2012.

[92] D. Pihler-Puzović, R. Périllat, M. Russell, A. Juel, and M. Heil. Modelling the suppression of viscous fingering in elastic-walled hele-shaw cells. Journal of Fluid Mechanics,

731:162–183, 2013.

[93] D. Pihler-Puzović, A. Juel, and M. Heil. The interaction between viscous fingering and wrinkling in elastic-walled hele-shaw cells. Physics of Fluids, 26:022102, 2014.

[94] A. Taheri, J. D. Ytrehus, B. Lund, and M. Torsæter. Use of concentric hele-shaw cell for the study of displacement flow and interface tracking in primary cementing. Energies, 14:51, 2020.

[95] Y. Wang, R. A. Pethrick, N. E. Hudson, and C. J. Schaschke. Rheology of poly(acrylic acid): A model study. Industrial and Engineering Chemistry Research, 51:16196–16208, 2012.

[96] S. Khanlari and M. A. Dubé. Effect of Ph on poly(acrylic acid) solution polymerization. Journal of Macromolecular Science, Part A: Pure and Applied Chemistry, 52:587–595, 2015.

[97] M. Mirzadeh and M. Z. Bazant. Electrokinetic control of viscous fingering. Physical Review Letters, 119:174501, 2017.

[98] D. E. Barton, M. Abramovitz, and I. A. Stegun. Handbook of mathematical functions with formulas, graphs and mathematical tables. Journal of the Royal Statistical Society. Series A (General), 128, 1965.

[99] G. Staikos and G. Bokias. The intrinsic viscosity of poly(acrylic acid) and partially neutralized poly(acrylic acid) by isoionic dilution. Polymer international, 31:385–389, 1993.

[100] B. Kim, H. Park, S. H. Lee, and W. M. Sigmund. Poly(acrylic acid) nanofibers by electrospinning. Materials Letters, 59:829–832, 2005.

[101] E. Di Giuseppe, F. Corbi, F. Funiciello, A. Massmeyer, T. N. Santimano, M. Rosenau, and A. Davaille. Characterization of carbopol® hydrogel rheology for experimental tectonics and geodynamics. Tectonophysics, 642:29–45, 2015.

[102] M. T. Garay, C. Alava, and M. Rodriguez. Study of polymer–polymer complexes and blends of poly(n-isopropylacrylamide) with poly(carboxylic acid). 2. poly(acrylic acid) and poly(methacrylic acid) partially neutralized. Polymer, 41:5799–5807, 2000.

[103] M. Todica, R. Stefan, C. V. Pop, and L. Olar. Ir and raman investigation of some poly(acrylic) acid gels in aqueous and neutralized state. Acta Physica Polonica A, 128:128, 2015.